

# SWARM-PROBE ENABLING ATEG REACTOR

# SPEAR

NASA Innovative and Advanced Concepts Phase I Final Report

**Award Number:** 80NSSC19K0962

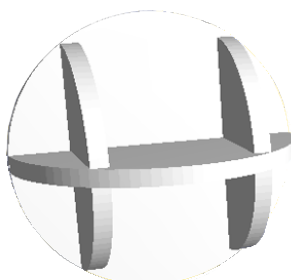
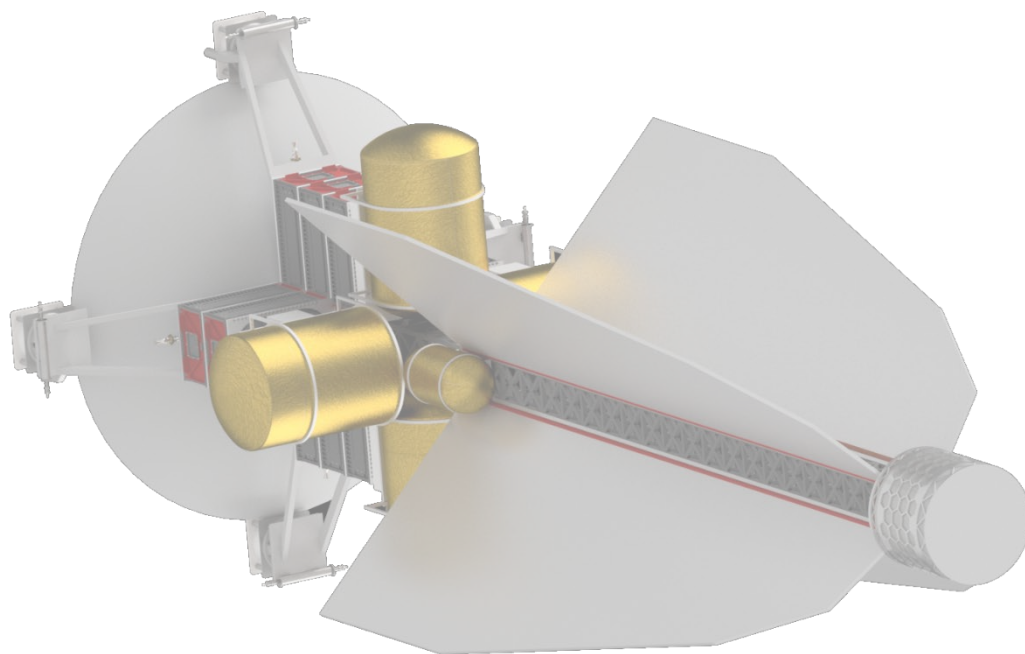
**Principal Investigator:** Dr. Troy Howe- Howe Industries LLC

**Howe Industries Team:** Dr. Steven Howe, Jack Miller, Kyle Weiss, Nathan Blaylock

**Partners:**

Atomos Space

The Hypershield Partnership



## Executive Summary:

Deep space exploration is a challenging engineering task with numerous scientific benefits. The wealth of resources and scientific knowledge that lays beyond Earth orbit is boundless but remains unreachable except for a select few government agencies around the world. The astonishing costs involved with deep space programs dissuades commercial entities from producing their own deep space exploration vehicles. However, as the rapid expansion of commercial involvement in Earth orbit increases it is only a matter of time before commercial efforts begin focusing on deep space for development and exploration.

Several key issues arise from the desire for deep space exploration, primarily the need for efficient, long term power production. Traditional fuels don't have the required energy density to power a spacecraft for years, and photovoltaic power generation drops off drastically as the distance from the sun increases. To combat this lack of resources, it is possible to utilize a nuclear power source in the form of radioisotopes or fission to create a heat source for a power conversion system to produce electrical power. However, traditional thermoelectric generators used with radioisotopes are relatively inefficient and large fission systems have heavy dynamic power systems to produce power.

Howe Industries proposes an innovative advanced thermoelectric generator (ATEG) power conversion system to provide solid state power generation at high efficiency. This system will be integrated into the Swarm Probe-Enabling ATEG Reactor (SPEAR) probe that will enable commercial exploration and development of deep space starting with the exploration of Europa. The SPEAR probe is powered by a 15 kWt nano-reactor, and with the included ATEG power conversion system can produce 3kW of electrical power. This enables the nuclear electric propulsion (NEP) system to propel the SPEAR spacecraft from Earth orbit to Europa under its own power. With a low mass this system, the SPEAR probe minimizes traditionally prohibitive launch costs and can deliver a 70 kg payload of CubeSats to Europa to search for signs of organic life.

Howe Industries investigated the SPEAR probe in this NIAC Phase I study to determine the potential for the successful exploration of Europa. As part of this NIAC study, Howe Industries thoroughly investigated the ATEG power conversion system. Computer models and simulations were created to determine what the behavior of the ATEG system and the effects various dopants had on the total conversion efficiency. A physical experiment was also conducted using a radiation field from a TRIGA fission reactor to validate the mechanisms that make the ATEGs so efficient. The results showed promising potential for astonishing increases in ATEG efficiencies over traditional TEGs, increasing from the usual 5-7% efficiency to over 25%.

In this Phase I study Howe Industries also investigated the nano-reactor, radiation shielding, radiation environments, overall design of SPEAR and its CubeSats, as well as the mission operations with the CubeSat swarm at Europa. Two partners, Atomos Space, and The Hypershield Partnership also investigated different aspects of the SPEAR probe. Atomos Space investigated SPEAR's trajectory, determined the optimal thruster selection, and assisted in the mass budget for this mission. The Hypershield Partnership performed thermal analysis of the SPEAR system and its ability to reject heat and maintain stable operating temperatures for the ATEG power conversion system. These studies have all shown that the SPEAR probe and its ATEG power conversion system remain a viable method for low cost commercial exploration and development of deep space. Recent developments and evidence for Europa plumes have grown within the last year, making this mission highly applicable to current events. Not only would SPEAR set out to prove high efficiency solid state power conversion is possible, it would have a high probability of finding extraterrestrial life on Europa.

The applications for SPEAR and the ATEG power conversion system are boundless from both a deep space and terrestrial perspective. The power conversion system could make the breakthroughs needed for solid state power conversion a reality. Phase II efforts would set out to further develop the ATEG power conversion system with efforts to create a functional ATEG unit to empirically show conversion efficiency. Further refinements and investigations into SPEAR's design would validate its potential for a successful deep space exploration vehicle and to accelerate the development of deep space for humanity.



## Table of Contents

1	Introduction .....	5
2	Mission Concept and Architecture.....	6
2.1	Earth Orbit and Spiral Transfer .....	6
2.2	Interplanetary Cruise Phase.....	7
2.3	Europa/Jovian System Operations.....	8
3	Spacecraft Design Overview .....	9
3.1	Electrical Power System .....	10
3.2	Communications .....	12
3.3	Propulsion .....	13
3.4	Thermal Control .....	13
3.5	Attitude Determination and Control System .....	13
3.6	Command and Data Handling .....	14
3.7	Payload.....	14
3.8	Mass Model.....	14
4	NIAC Phase I Overview.....	16
4.1	ATEG Power Conversion System.....	16
4.2	Nano-reactor, Shielding, and Neutronics.....	16
4.3	CubeSat Swarm .....	17
4.4	Trajectory, Power Distribution, and Mass Budget.....	17
4.5	Thermal Management .....	17
4.6	Mission Costs .....	17
5	Advanced Thermoelectric Generator Design, Modeling, and Validation .....	17
5.1	Thermoelectric Generator Principles.....	18
5.2	Advanced Thermoelectric Generators.....	19
5.2.1	Radioisotope Source .....	19
5.2.2	Neutron Interaction .....	20
5.3	ATEG Modeling .....	20
5.4	Experimental Results .....	29
5.5	Potential ATEG Materials.....	31
5.6	ATEG Conversion System Conclusions .....	33
6	Reactor and Radiation Shield Design .....	34
6.1	Reactor Design .....	34



6.1.1	Geometry Selection .....	34
6.1.2	Reactor Materials.....	36
6.1.3	Advantages of LEU .....	37
6.1.4	Advantages of LiH .....	37
6.1.5	ATEG Location .....	37
6.1.6	Neutron Flux from Reactor .....	38
6.2	Shield Design.....	38
6.2.1	Propellant Tanks.....	39
6.2.2	Shield Mass .....	39
6.3	Planetary and Deep Space Radiation Environments.....	40
6.3.1	Earth Radiation Environment.....	40
6.3.2	Interplanetary Radiation Environment .....	41
6.3.3	Europa Radiation Environment.....	42
7	Thruster Selection .....	42
7.1	Specific Impulse Selection.....	43
7.2	Thruster Selection .....	44
8	SPEAR Mission Performance .....	45
8.1	SPEAR Trajectory Design .....	45
8.2	Kilopower Trajectory Design .....	46
8.3	Comparison .....	47
8.4	Mission and Systems Engineering Recommendations .....	48
9	Thermal Systems design and performance analysis .....	49
9.1	Preliminary Design Study .....	49
9.2	Radiator Performance Study.....	53
9.3	Trajectory-Based Thermal Analysis of the Full Vehicle .....	57
9.4	Considerations for Phase II Thermal Analysis .....	60
10	CubeSat Swarm .....	61
10.1	Europa Environment .....	61
10.1.1	Evidence of Plume Activity.....	62
10.1.2	Plume Mechanics and Particle Behavior .....	63
10.1.3	Habitability of Europa .....	63
10.2	Wireless Power Transmission .....	64
10.2.1	Transmitter Size .....	65



10.2.2	Beam Divergence .....	66
10.2.3	Distance.....	66
10.2.4	Frequency.....	67
10.3	CubeSat Swarm Operations .....	68
10.4	Charging Considerations .....	68
10.4.1	Antenna Orientation .....	69
10.4.2	Estimated Absorbed Power and Charging Regime .....	70
10.4.3	Improvements to Charging System.....	70
10.5	CubeSat Components.....	71
10.6	CubeSat Science Objectives .....	74
10.7	Sample Collection .....	75
11	Cost Comparison and Estimation.....	76
11.1	Launch Costs .....	77
11.2	Operational Costs.....	78
11.3	Reactor and Exotic Material Costs .....	80
11.4	Development Costs .....	81
12	Conclusions and future work .....	82
13	References .....	83



## 1 INTRODUCTION

Deep space exploration has been the cornerstone of engineering challenges and scientific discoveries for many decades. Within the entire history of space exploration only government organizations have sent probes beyond Earth to explore deep space. While a rapidly developing space economy around Earth spurred by the NewSpace movement is developing, access to deep space remains inaccessible to private industry. The astronomical costs and advanced technologies required for such a mission have deterred all but government agencies. With untold knowledge and resource wealth beyond Earth, deep space entices private industry, scientists, wonderers and dreamers alike, all without the resources to explore it.

One of the most significant challenges in deep space exploration is power generation. As the distance away from the sun increases the solar irradiance decreases limiting the feasibility of solar panels for power generation. Juno, utilizing three massive solar panels, produces only 500 Watts of power at Jupiter [1]. Nuclear powered exploration systems have been used with the aid of radioisotope thermoelectric generators (RTGs), which harvest energy from the heat produced by the decaying nuclear material. These sources can only be used by government organizations and are in short supply, with only a handful of missions available before plutonium reserves run dry. Reaching deep space is a costly challenge requiring large launch vehicles to transport the spacecraft from Earth to their destination. With the incomprehensible scientific wealth and resources available, there remains no current solution for private industry to explore this knowledge and resources.

The Swarm Probe Enabling ATEG Reactor (SPEAR) system will venture to make deep space exploration open to private industries. Several novel designs, including a nano-sized nuclear reactor and advanced thermoelectric generators (ATEGs), combine to produce one of the highest performing deep space platforms in existence. The ATEGs used to harvest power from the nano-reactor offer solid state energy production efficiencies well above current technologies. This advancement, which can be applied to a multitude of space technologies, is what drives SPEAR's potential for success. With a conservative 3 kW of electrical power, SPEAR outperforms any previous deep space power system including RTGs and solar panels (beyond Earth orbit) and contends with future nuclear systems in development. SPEAR can explore vast stretches of the solar system at fractions of the cost of traditional missions. Its compact form factor and low mass allows it to be launched on inexpensive launch vehicles, and its nuclear electric propulsion system can propel it to the far reaches of the solar system. SPEAR has been designed to include a swarm of 10 CubeSats in a 6U form factor which can be deployed at its final destination or throughout its mission. The gradual miniaturization of spacecraft into CubeSats has shown that an immense amount of high impact science can be placed in a small package. The CubeSat design is familiar to universities, private industry, and government organizations looking to test technologies and perform high impact scientific studies. Instead of being limited to Earth orbit SPEAR can transport CubeSats millions of kilometers away allowing many new participants to explore deep space at a fraction of the cost of traditional missions. SPEAR has the capability to bring new scientific research from deep space back to Earth, pushing humanity's exploration frontier further than ever before.

One particularly exciting application for the SPEAR probe is the exploration of Jupiter's moon Europa. NASA has put a mission to explore Europa and investigate its habitability as the second highest-priority mission for the decade after the Mars 2020 mission [2]. Its expected mission costs at the time of the survey was estimated at \$4.7 billion. This mission is expected to launch sometime in the 2020's with an unknown launch date and launch vehicle [3]. While this mission contains many science instruments, its costs and uncertainty in launch date make its future uncertain. SPEAR could transport a swarm of CubeSats to Europa for a fraction of the cost to accomplish more focused science goals. Each CubeSat will explore the Europa environment with high resolution cameras, detectors, and communications devices. With evidence of plumes erupting from Europa's surface, the primary goal of the CubeSats will be to fly through these plumes and analyze the material for evidence of extraterrestrial life. This swarm has a higher probability of intercepting plumes, maximizing the potential to discover organic molecules. The high-resolution maps generated by onboard cameras will be paramount for future missions that intend to land on the surface of Europa. At Europa, the SPEAR probe will have more power available than any other deep space probe allowing for large quantities of data to be transmitted to Earth for analysis. SPEAR has the capabilities to unravel the mysteries that Europa contains and answer some of the greatest scientific questions ever known.



## 2 MISSION CONCEPT AND ARCHITECTURE

The SPEAR spacecraft is an interplanetary nuclear electric propulsion (NEP) probe designed to study the Europa environment in search of life. This ultra-lightweight probe is meant to significantly reduce mission costs for interplanetary space missions and open deep space exploration to private industries by using a majority of commercial off the shelf (COTS) components as well as a low enriched uranium (LEU) reactor. With a total mass of 1517 kg SPEAR can be launched at a relatively cheap price compared to most interplanetary missions. With a comparatively small form factor, it may be able to ride share with another primary payload or launch on board a small dedicated rocket. SPEAR's current design utilizes limited moving parts to reduce failure modes when being deployed in space and has been designed to fit inside the Minotaur IV launch vehicle. Modifications including extendable booms and radiators can be used to further decrease the size of SPEAR to fit within even smaller launch vehicles or be compact enough for a ride share mission.

### 2.1 Earth Orbit and Spiral Transfer

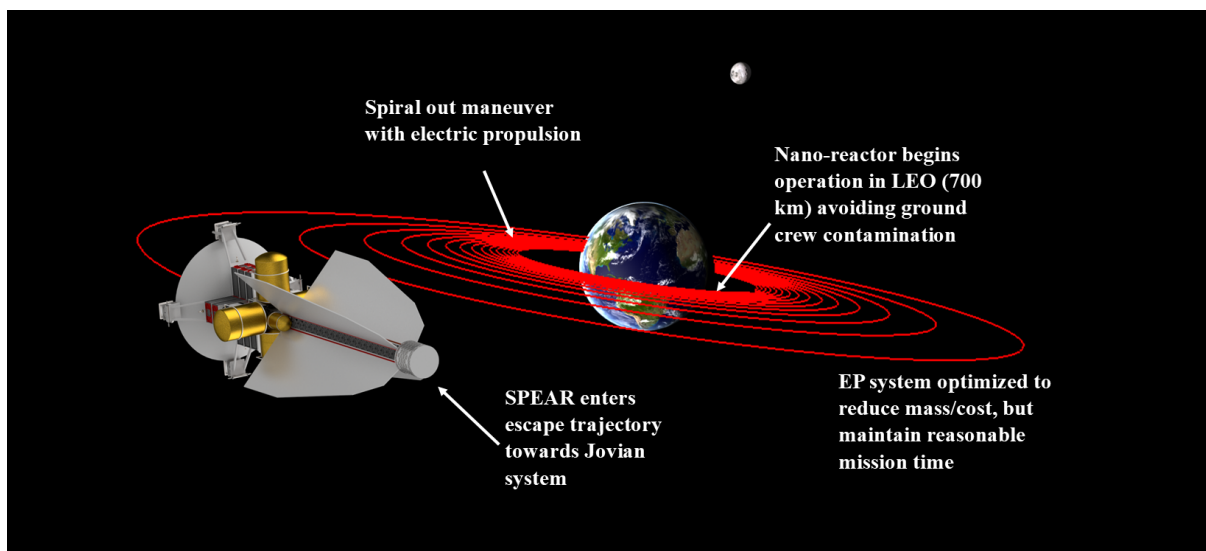


**Figure 1: After being launched and initiating the reactor, SPEAR will perform a spiral transfer maneuver to escape Earth. The NEP system has been optimized to reduce mass, which consequently reduces launch costs, and maintain a reasonably short mission timeframe. SPEAR will use this time to report any important scientific and spacecraft information back to ground crews before entering a transit mode for the interplanetary phase of the mission.**

After launching into orbit around Earth at 700 km, SPEAR will engage the reactor control rods to begin the fission process. The reactor will not produce radiation until this process begins, reducing radiation contamination concerns on Earth. Once activated, the SPEAR will produce 15 kW of thermal power and is estimated to produce 3 kW of electrical power from the ATEG system. SPEAR will then utilize its NEP system to conduct a spiral transfer maneuver to escape Earth. A graphic of this phase of the mission is visible in Figure 1.

Orbiting around Earth and conducting the spiral transfer maneuver presents the maximum thermal load SPEAR will see due to the Earth's albedo, infrared signature, and proximity to the sun. To reduce the thermal load on the spacecraft, SPEAR will be slowly rotated around its long axis to ensure even heating of the spacecraft. During the initial phases with such close proximity to Earth, ground controllers are able to use this time to study the performance of the reactor and collect any important science data transmitted by SPEAR before interplanetary transit begins.

## 2.2 Interplanetary Cruise Phase

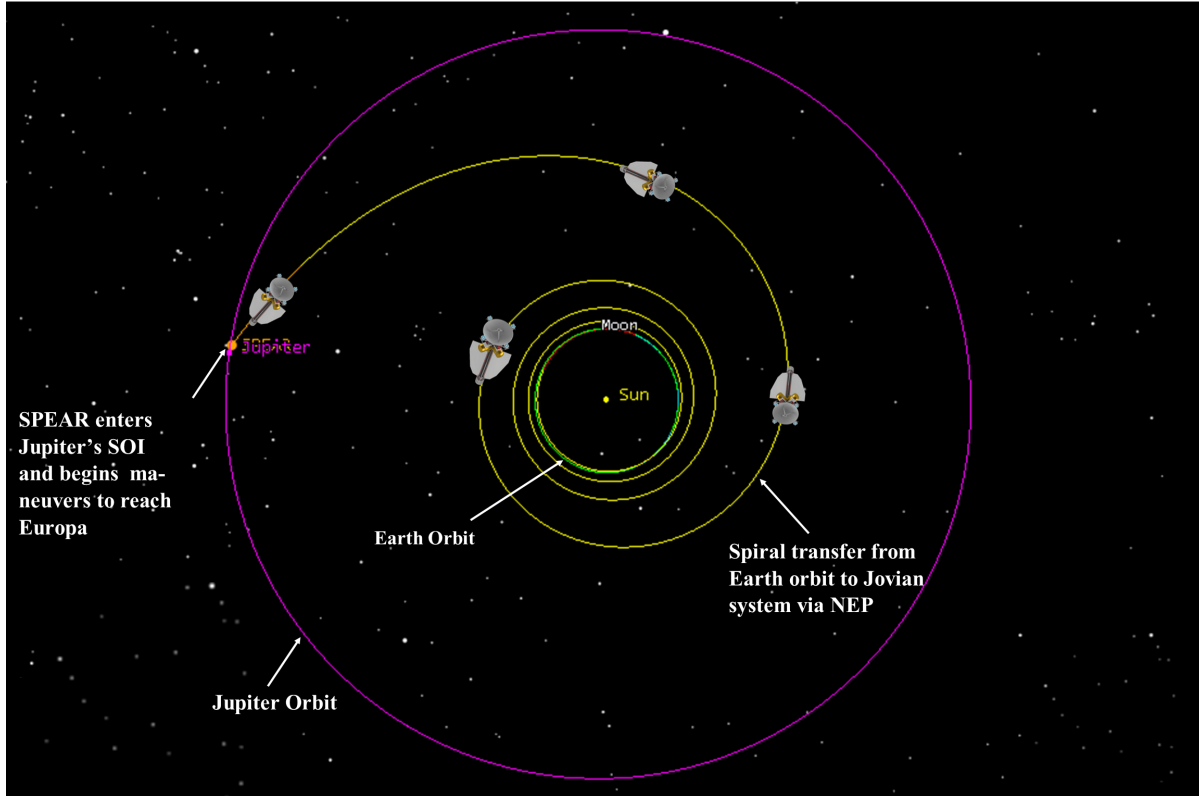


**Figure 2:** After escaping from Earth's gravity, SPEAR will continue on an interplanetary spiral trajectory to the Jovian system. Non-essential systems will enter a hibernation mode and the reactor will maintain its operational capacity of 15 kWt to power the electric thrusters. Once SPEAR is within Jupiter's sphere of influence it will begin its spiral transfer to Europa.

After leaving Earth's influence, SPEAR will continue on its interplanetary cruise phase to Jupiter. Cost models include staff to monitor navigation to make minor course corrections on its journey to the Jovian system, but subsequent efforts will be made to introduce an artificial intelligence-based guidance system. This will limit the need for a full staff to be present during the somewhat long transit times, and human intervention will only be necessary in the rare event that something unexpected happens to the craft while flying through the vacuum of space. This spiral transfer to the Jovian system is visible in Figure 2.

During this time the reactor will continue to operate at full power for the NEP system while its other systems enter a hibernation mode. Vital components of the spacecraft are protected from radiation coming from the reactor via a radiation shadow shield near the propellant tanks at the rear section of the craft. This shadow shield is designed to protect the most sensitive components of the spacecraft including electronics and the CubeSat payloads. To minimize mass, the shield does not protect some structural components and is positioned far away from the reactor with substantial Xe propellant in the tanks also blocking some of radiation. By not fully encapsulating the reactor with shielding, hundreds of kilograms of dead mass can be saved, and the radiation harmlessly dispersed into space. SPEAR will still be subjected to galactic cosmic rays (GCRs) and any solar particle events (SPE) that may occur, but the included shield and radiation hardened electronics will assist with longevity during transit.



### 2.3 Europa/Jovian System Operations

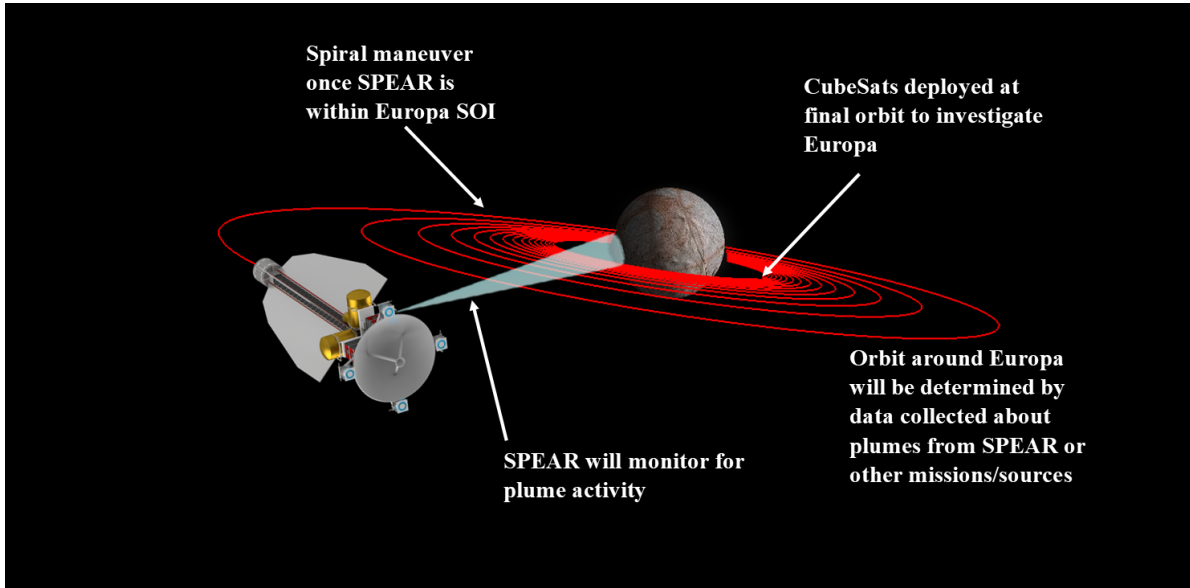


**Figure 3:** Similar to the Earth spiral transfer maneuver, SPEAR will utilize a similar maneuver, but descend to a lower altitude above Europa. This time will be used to study Europa and search for evidence of plumes and their behavior to determine the best orbit to deploy the CubeSat swarm. After spiraling down to the desired orbit, SPEAR will deploy its CubeSat swarm to capture plume ejecta in search for extraterrestrial life.

Upon arrival at Europa, SPEAR will begin studying the Europa environment. SPEAR will contain only a few scientific instruments on the main craft, as most of the payload mass has been allocated to the CubeSats. Nonetheless, SPEAR will monitor the surface of Europa for several Europa days (approximately 3.5 Earth Days) to investigate changes to the surface and gather preliminary data. Plumes have been confirmed on Europa on only a few separate occasions, one via the Hubble Telescope, another from the Keck Observatory, and the last being the Galileo mission which is thought to have flown through a plume based on anomalous data while passing Europa [4] [5] [6]. The spiral transfer and observation phase is visible in Figure 3. After achieving the proper orbit, SPEAR will begin deployment procedures visible in Figure 4. Each CubeSat can apply a small amount of delta-v to change its orbital inclination and cover the maximum amount of area about the main orbit of the SPEAR craft. CubeSats will be launched two at a time from opposite sides of the SPEAR probe to minimize attitude changes imparted on SPEAR. Each CubeSat will be equipped with several science instruments to monitor the Europa environment and include a mechanism to capture and analyze plume particles. The purpose of these 10 CubeSats is to maximize the probability of intercepting a plume particle. With all the CubeSats deployed, a wide swathe of the moon

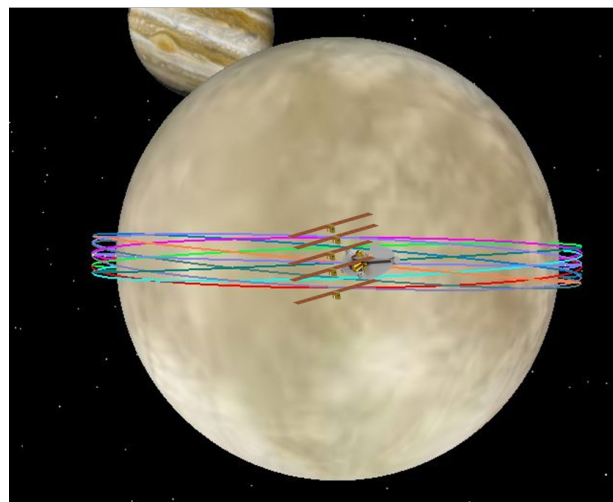


**Figure 4:** SPEAR will deploy its CubeSats in the orbit deemed most favorable for plume/particle interceptions. The large area covered and number of CubeSats allows for high throughput of material for the detection of life.

is covered due to the CubeSats weaving up and down relative to the main craft. The equipment and CubeSat performance will be covered in more detail in a later section. After deployment of all the CubeSats SPEAR transitions into a “mother-ship” mode for transmitting, receiving, and processing data. Sections below detail the RF and laser options for beaming power to the CubeSats to keep them operating for the duration of the mission. The SPEAR craft processes the information gathered from the CubeSats and will intermittently transmit data back to Earth with its high gain antenna. Each CubeSat is expected to operate for roughly 30 days before reaching its maximum dose of ionizing radiation. After the 30-day CubeSat operation is complete and all scientific data has been transmitted to Earth, SPEAR’s health and systems will be assessed to determine any additional missions that can be completed before succumbing to radiation. So long as systems remain functional, the swarm can gather visual data on the surface, scan for life, or monitor the local area.

### 3 SPACECRAFT DESIGN OVERVIEW

SPEAR has been designed for extreme simplicity to reduce the number of fatal errors the system may experience on its voyage to Europa. There are no large deployable mechanisms in the current design version, which reduces the potential for failure within orbit significantly. The reactor is safe in nature and only produces radiation via activation of control rods to begin the nuclear fission process. This design reflects a simplistic payload of CubeSats which will be deployed at Europa and is visible in Figure 5. SPEAR could be easily modified to deliver a similarly sized payload to other locations within the solar system. Again, a system of CubeSats is preferred because of its high technology readiness level (TRL) and industry familiarity with the CubeSat form factor.

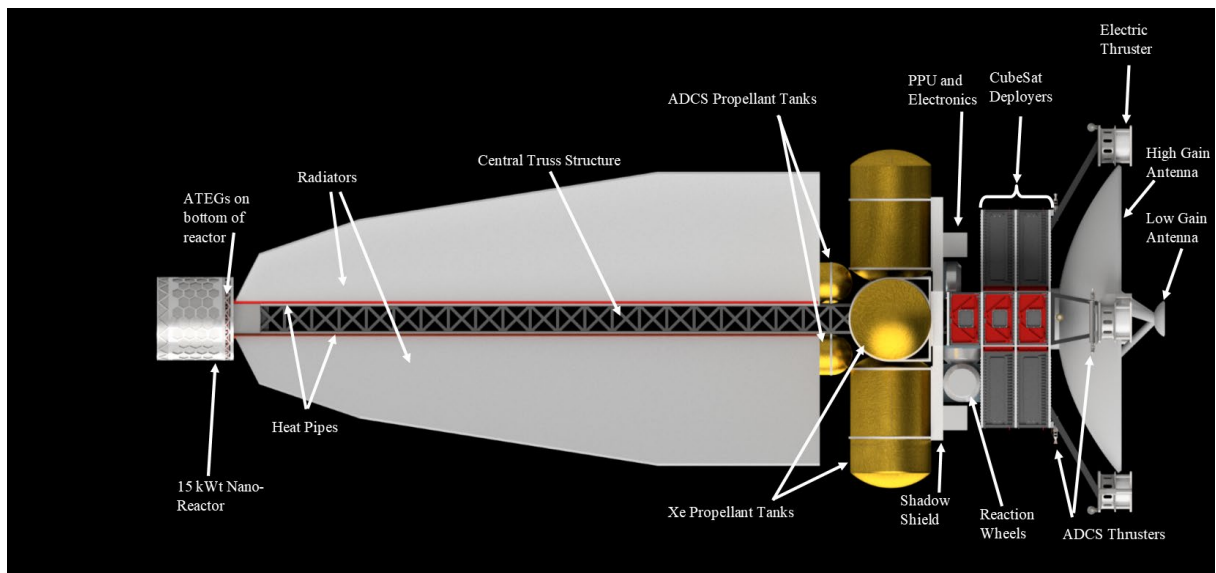


**Figure 5: Complete SPEAR spacecraft with CubeSat swarm payload.** The advanced thermoelectric generators enable massive efficiency increases over traditional thermoelectric generators reaching efficiencies matching or exceeding current sterling or dynamic power systems. A lightweight and compact form factor enable SPEAR to be launched on small/medium launch vehicles allowing for much lower launch costs. SPEAR has the potential to revolutionize the accessibility to deep space for both government use and private industries in the near future.

### 3.1 Electrical Power System

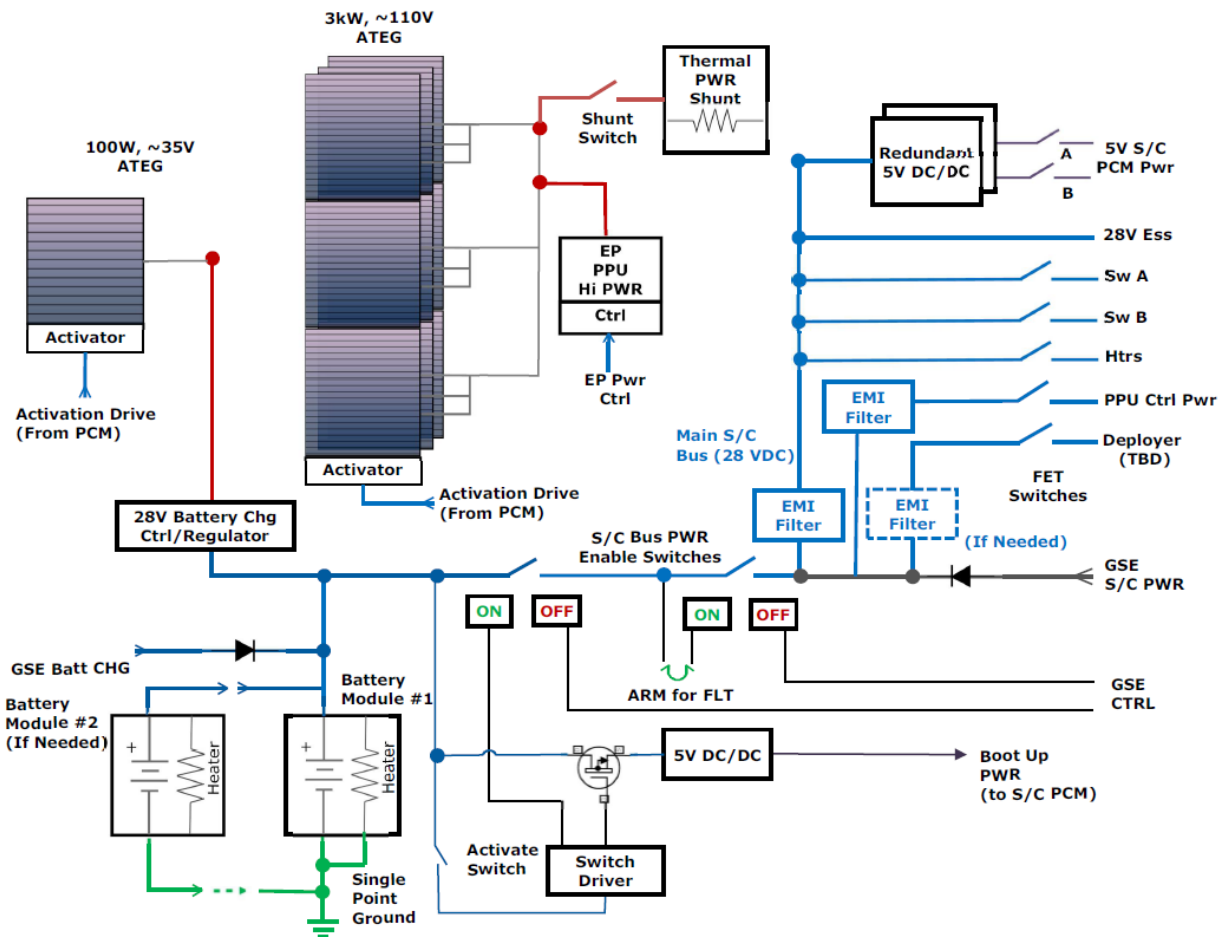


**Figure 6: Tentative power management and distribution of spear. Batteries allow for reactor start up and contain enough power for 24 hours of emergency operation for ground crews.**

A 15 kWt reactor sits atop the SPEAR probe, which when combined with the ATEG's can deliver 3 kW of electrical power. This power will primarily be applied to the NEP system during its mission to Europa. The design for the nano-reactor involves lightweight moderator materials and low enriched uranium (LEU) to minimize launch costs and allow for private ownership of the nano-reactor. A small array of batteries will be used to operate SPEAR while its nano-reactor is not operating. This should only occur during initial operations around Earth and any situations where the reactor needs to be powered down. The ATEGs and nano-reactor design will be discussed in later sections with greater detail. The electrical subsystem is diagramed in detail in Figure 6. The SPEAR Electrical Power System (EPS) utilizes the available energy from an ATEG capable of being configured to supply two individual and unique loads. The EPS has two buses; a  $3\text{kW}_e$  source of relatively-high DC voltage to serve as the energy source for the NASA developed NEXT-C electric propulsion (EP) system; and a separate  $\sim 100\text{W}_e$  source of power at a voltage suitable as input to a battery charge controller and regulator supplying power to the  $28\text{V}_{\text{DC}}$  SPEAR spacecraft bus. In Figure 6, depicting the functional architecture of the system, two ATEG units are shown; while the system could be implemented with two independent ATEG sources, it is also possible (and desirable from mass, volume and thermal management perspectives) to provide both high power and low power taps from a single ATEG unit. A summary of the acronyms used can be found in Table 1 and the  $100\text{W}_e$  and  $3\text{kW}_e$  ATEG units can be found in Table 2.

**Table 1: Acronyms for SPEAR EPS functional architecture diagram**

Acronym	Definition
ATEG	Advanced Thermoelectric Generator
Batt	Battery
CHG	Charge
Ctrl	Control
EMI	Electromagnetic Interference
EP	Electric Propulsion
Ess	Essential (Bus)
FET	Field Effect Transistor
FLT	Flight
GSE	Ground Support Equipment
Htrs	Heaters
kW	Kilowatt
PCM	Power (Subsystem) Control Module
PPU	Power Processing Unit (for EP)
PWR	Power
S/C	Spacecraft
Sw	Switched (Power Bus)
TBD	To Be Determined
W	Watt

**Table 2: 100 We and 3kW<sub>e</sub> ATEG units summarized below not accounting for thermal shielding and other heat conversion hardware, raw thermoelectric material only.**

	100W <sub>e</sub>	3kW <sub>e</sub>
Current (A)	2.856	27.094
Voltage (V)	35.017	110.722
Efficiency (%)	~30%	~35.5%
Number of ATEG couples (#)	859	2,715
ATEG mass (kg)	0.235	1.696
Configuration	All in series	All in series

The EPS is designed to start up upon SPEAR deployment from the launch vehicle. An Activate Switch will close upon deployment, which would switch on main spacecraft bus power and energize a field effect transistor (FET) switch to also connect 28V main bus power to a “startup” 5V<sub>DC</sub> converter. The 5V output of that startup converter will supply system boot up power to the Power Controller Module (PCM), a microprocessor (for simplicity not explicitly shown in the figure) that then would execute the software instructions necessary to turn on the rest of the power system and to configure additional switched 28V buses to supply power to the rest of the spacecraft in a planned, controlled manner. Some of those switched buses may need to be electromagnetic interference (EMI) filtered to ensure that electromagnetic noise originating from a component on one bus would not propagate to devices on other spacecraft buses.

Upon successful startup and self-checkout of the rest of the systems on the spacecraft, all initially performed with power supplied by Lithium-Ion battery modules, the ATEG will be activated. The batteries have been sized to operate for a total of 48 hours, with a storage capacity of 108Ah.

The activation will be via a motor driver signal from the PCM. Once active, the ATEG will source power to maintain the 28V main bus indefinitely, to charge the battery (to be available as a future contingency power source),



as well as to source high power for the EP power programming unit (PPU), and thus the Hall Effect Thruster. Once activated the ATEG will operate continuously. During those times when the EP is not consuming power the 3kW<sub>e</sub> ATEG will need to have its power dissipated via a shunt resistor to prevent the ATEG from overheating. Connections to that shunt, as well as control of the EP PPU, will also be managed by the PCM.

Prior to launch, control of the spacecraft and charge management of the battery will be possible via Ground Support Equipment (GSE). The GSE will have the ability to set main bus switches in a “safe for launch” OFF state. Additional protection from inadvertent startup is provided by an “Arm for Flight” cable jumper that prevents any power from the battery being applied to the spacecraft 28V bus until the jumper is installed. Operationally, installation of that jumper would take place as one of the last activities during close-out operations just prior to launch. The GSE will also have the ability to source 28V spacecraft power via an independent connection which would only be used to check out spacecraft components prior to launch. The PCM is inhibited from initiating its post-deployment activation sequence by A-B lockout switches on the 5V power that are intended to be used to operate the PCM only post-deployment.

At Europa, SPEAR will have an unparalleled quantity of power for numerous applications including science operations, powering of CubeSats, and communications with Earth. Each CubeSat will be powered via radio frequency (RF) charging from the SPEAR Probe. This will minimize the complexity of the CubeSats and their systems to ensure mission success. The RF charging is attractive to charge the CubeSats due to the fact that a high power RF system is already installed and used for communications. Additionally, changing the reactor power levels can be complicated due to fission product buildup and the presence of neutron poisons in the reactor, so it is recommended that the power production stay as constant as possible during the entire mission. As it will already be generating 3kW of continuous electric power and has an RF system on board, using this for charging seems a viable method for keeping masses low.

A rather unique feature of the ATEG system is to provide the desired voltage and current to different systems without changing the production profile of the power system. Various voltages and currents can be achieved by simply changing which TEG feet are in series or parallel when the units are installed. Utilizing this unique feature, the power processing can be more efficient as the need to convert between high voltage, high current, and other sources can be reduced significantly. In the diagram above, a 100W subsystem power source is wired separately from the main ATEG array and operates at 35V. The main array has more units connected in series, which brings the total power up to 3kW and 110V.

### 3.2 Communications

A prominent feature of SPEAR is its high gain antenna situated on the bottom of the spacecraft. This antenna will be used to communicate with Earth throughout its mission. Instead of powering down the reactor at Europa to minimize thermal requirements, SPEAR will utilize the power from the reactor to beam power to the CubeSats and send science data back to Earth. The 1.5 meter diameter dish is comparatively smaller than other spacecraft such as Juno or Cassini with 2.5 meter and 4 meter diameter dishes respectively [7] [8]. The high gain antenna size is restricted by the fairing size of the launch vehicle, so a 1.5 meter dish was chosen to offer high performance with minimal form factor. Assuming SPEAR broadcasts at similar frequencies to Juno on the fifth and sixth channel of the deep space network the respective gains from SPEAR should be 33 dB and 32.5 dB. When Jupiter is at its farthest location from Earth, the received power should be -136.41 dBm and at its closest location the received power should be -133.02 dBm. These values appear to be between that of the Juno probe and Cassini with received powers of -129 dBm [7] and -137.87 dBm [8]. The large amount of power available for communications makes it possible to reduce the size of the antenna dish, allowing SPEAR to fit within smaller payload fairings compared to other deep space missions.

SPEAR will not only need to communicate with Earth, but also relay information to and from the 10 deployed CubeSats. This will leverage the technologies currently available for Earth based communication satellites. S-band receivers, transmitters, and patch antennas will be utilized to communicate with SPEAR. Most communications should occur between SPEAR and individual CubeSats, but the s-band communications architecture allows for high data rate communication between satellites. This could prove useful if SPEAR needs to send information to CubeSats that are not reachable for direct communication. Analysis of the secondary mode of remote charging from the SPEAR probe will be discussed in a later section with greater detail.



### 3.3 Propulsion

Interplanetary NEP systems have no flight heritage, but many systems have been proposed for missions to the outer solar system. Most of these systems involve dynamic power generation systems for their high conversion efficiency. The Jupiter Icy Moons Orbiter (JIMO) was a 100 kW NEP spacecraft slated to explore three of Jupiter's moons including Europa with a Brayton power conversion system [9]. This massive spacecraft was eventually cancelled, and the concept never fully tested. The SPEAR probe leverages similar concepts from the JIMO mission, including the use of a high specific impulse ion thruster. SPEAR will utilize the NASA Evolutionary Xenon Thruster (NEXT), or a system like it, for its primary propulsion. A NEXT thruster is capable of 4,190s of specific impulse with projected total throughput of over 730 kg of propellant [10]. These parameters make the NEXT thruster more than ideal for the 10 year mission lifetime.

It should be noted that the artist rendering includes four thrusters instead of a single NEXT thruster. The NEXT thruster is considered a place holder until the final design for SPEAR is determined. This may include using different thrusters of lower individual power levels or rearranging components for the final design.

### 3.4 Thermal Control

Positioned on the long axis of the SPEAR probe are four large radiators. These radiators are used to dissipate the 12 kW of waste heat from the reactor. Heat pipes are used to transfer heat from the back of the ATEGs out to these radiators. The use of four radiators results in a less effective design due to the radiators shining on each other, but due to the truncated space of the launcher fairing it was necessary to achieve the required surface area. The possibility remains to deploy radiators or extend a telescoping boom for the main shaft, but this would introduce moving parts and potential modes of failure. For this design, the extra radiator mass was acceptable but other missions may be willing or able to use a more optimized system.

A detailed analysis of the radiator system was conducted to determine the maximum heat rejection while maintaining a low mass system. With a complex trajectory, SPEAR's radiators need to reject heat as it orbits Earth, on its journey to the Jovian system, and while it is at Europa. A carbon-based material with heat pipes containing water as the working fluid were chosen. Analysis was performed on the trajectory SPEAR would take to the Jovian system to determine the optimal size of the radiators to maintain a steady 350K cold side for the ATEGs.

### 3.5 Attitude Determination and Control System

As SPEAR travels through space it will utilize its electric propulsion system to perform various attitude control maneuvers as well as a suite of attitude control thrusters. Four reaction control wheels will be used to control SPEAR's attitude in orbit as well. These systems were chosen as they primarily rely on power generated by the spacecraft instead of additional propellant systems to minimize mass and complexity, and the SPEAR craft has a surplus of electrical power. With the excess power available at Europa the reaction wheels will be used to the fullest extent when attitude changes are required by the SPEAR Probe. The reaction wheels are better suited for use around Europa as this is when the system will be at its lightest. Around Earth orbit, the spacecraft will rely more on its thrusters to provide gradual attitude changes in addition to the reaction control wheels. Several sun sensors, star trackers, and magnetometers will be used to determine the attitude of the spacecraft. The star trackers will be especially useful while navigating to Europa and other deep space locations. Several of these components are already commercially available and rated to moderate radiation levels, which will minimize the amount of shielding required in the Europa environment.

Reaction wheels and attitude control thrusters will be used around Earth and at the Jovian system to desaturate reaction wheels as well as perform attitude correction maneuvers. In deep space, a majority of the attitude control will be accomplished through the use of the primary electric propulsion system. This system will make gradual changes to the spacecraft's attitude for any corrections in its trajectory.

The monopropellant control system consists of 22 kg of monopropellant and 12 thrusters to provide agile maneuvering of the spacecraft and in deep space. This will be used for ADCS corrections or maneuvers that are too quick for the reaction wheels and passive system to support.





### 3.6 Command and Data Handling

SPEAR will use the previously demonstrated and highly reliable RAD750 computer to process information and handle data. This computer has fantastic heritage with numerous deep space missions. Included in the numerous probes that use the RAD750 computer is Juno, which is currently orbiting Jupiter [11]. The RAD750 is capable of withstanding up to 1 Mrad total ionizing dose (TID), which is ideal for surviving the radiation from the reactor and the radiation environment from Europa [12]. While the RAD750 comes in 3U and 6U form factors, it was not considered for the CubeSat computers because of its mass and power consumption.

### 3.7 Payload

The primary payload aboard SPEAR is the array of 10 CubeSats that will be delivered to Europa and form a swarm around the moon. Contrary to a satellite constellation in which all pieces remain in a constant position relative to each other, the CubeSats will be deployed at different times to create a dynamic weaving pattern for maximum surface coverage. Thus, the cluster of satellites will more resemble a swarm of insects than a constellation of stars. Each CubeSat has a mass of 7 kg for a total payload mass of 70 kg. More specifically, each CubeSat will contain a multispectral camera, Raman spectrometer, lab-on-a-chip for chirality detection and imaging via a microscope. The latter two will be used to detect the composition of Europa's plumes and detect for any extraterrestrial life. CubeSat scientific payload and other systems will be described in more detail in another section.

The secondary payload for Europa mission will consist of several observational instruments to observe Europa's surface. With the primary payload looking for signs of life, SPEAR will assume a primarily observational role of Europa. Reuse of several systems from other deep space probes is considered advantageous to reduce development costs. The JunoCam produced by Malin Space Science Systems will be used onboard the SPEAR probe to image the moon's surface [13]. This technology has already proven itself onboard the Juno spacecraft and is capable of withstanding the extreme Jovian environment [13]. Infrared cameras will also be included on the SPEAR probe monitor the temperature levels of Europa's vast ice sheet. SPEAR will also closely monitor the perturbations experienced by the CubeSats during its mission and relay any useful science data about anomalies around Jupiter. The SPEAR probe will also contain two sets of the same life detection instruments as the CubeSats contain for mission redundancy. After the primary CubeSat mission is over, mission extensions will be investigated based on the health of the spacecraft and propellant remaining.

### 3.8 Mass Model

A detailed mass model of the SPEAR system was created to estimate the initial wet mass of the system. SPEAR's original mass estimate was 1100kg, but after in-depth analysis during this Phase I study the total mass increased to just over 1,500 kg. A major factor in this was due to the size of the radiator system and the fact that 4 radiators were required to fit in the launch fairing. A cold side temperature of 350K was originally chosen to provide a comparison to the MMRTG systems available now. However, increasing this temperature would decrease the radiator area but decrease ATEG efficiencies. Additionally, expandable booms or a larger fairing would allow for more efficient radiator operation and reduced total mass. A more refined radiator design will be conducted in phase II to determine any potential mass savings. **Error! Reference source not found.** shows the mass budget for the SPEAR probe on its journey to Europa.



**Table 3: Launch mass of the SPEAR probe from the Phase I study. Various methods can be used to decrease this mass and will be discussed in various sections. \* notates estimation by Howe Industries, Atomos Space, and/or The Hypershield Partnership.**

Section	Quantity	Mass/ Unit (kg)	Mass (kg)	
<b>Power and propulsion</b>				587.3
<b>Reactor system</b>				134.9
Core	1	58.4*	58.4	
Fuel	1	76.3*	76.3	
Control rods and actuators	1	0.2*	0.2	
Shield				32.0
Main power conversion				11.9
Heat exchanger (hot)	1	7.5*	7.5	
ATEGs	1	4.4*	4.4	
<b>Thermal control system</b>				200
Radiators	4	50.0*	200.0	
<b>Primary propulsion system and Electrical Bus</b>				59.5
Thruster cluster	1	13.5 [14]	13.5	
PPU	1	40.0 [14]	40.0	
Mount	1	6.0 [14]	6.0	
<b>Secondary propulsion system</b>				35.1
Thruster Clusters	1	17.5 [15]	17.5	
Reaction wheels	4	4.4 [16]	17.6	
<b>Auxiliary power system</b>				22
Batteries, Drivers	1	12.0*	12.0	
Cables	1	10.0*	10.0	
<b>Structures</b>				24.8
Main truss	1	20.8*	20.8	
Tank and payload dispenser support	4	0.8*	3.1	
Secondary Structures	1	0.9*	0.9	
<b>Avionics</b>				25.7
Star trackers	2	0.35 [17]	0.7	
High-gain antenna	1	15.0*	15.0	
Structures and shield	1	10.0*	10.0	
<b>Tankage</b>				41.4
Mission propellant tanks	4	6.4*	26.4	
Feed lines and valves	1	10.0*	10.0	
Insulation	1	5.0*	5.0	
<b>Main mission section</b>				103.09
<b>Payload and provisions</b>				103.09
Board computer	2	0.15 [12]	0.29	
Telecommunication system	1	16.8*	16.8	
Payload dispenser	10	1.6 [18] [19]	16	
Cubesats	10	7.0*	70.0	
<b>Fluids</b>				826.3
<b>Mission propellant mass</b>				804.3
<b>Reaction control propellant</b>				22.0
<b>Launch mass</b>				1516.6 9





Another significant contributor to the overall mass is the amount of Xe propellant onboard the system. With improvements to the trajectory, the total mass of the system can be significantly decreased. As the ATEG system is further investigated and the possible efficiency for this system more refined there could be vast improvements upon the mass. A 20% ATEG efficiency was used as conservative estimate, and improvements to this decrease the amount of heat that needs to be rejected and increases the power available to the propulsion system, which would translate to a higher specific impulse. This higher specific impulse would correspond to a drop in the total propellant required for the mission. Refinements to these systems will occur in a Phase II study.

## 4 NIAC PHASE I OVERVIEW

Several key areas of study were identified to validate SPEAR as the next generation deep space exploration probe. These studies were identified as the most important aspects of the SPEAR probe and have the highest impact on its future success as well as applications towards other space missions. Howe Industries in conjunction with Atomos Space and The Hypershield Partnership investigated the following aspects of the SPEAR probe and Europa mission:

1. ATEG modeling and validation
2. Reactor and radiation shield design for various environments
3. CubeSat swarm at Europa and associated science goals
4. Mission trajectory and power distribution throughout various phases
5. Thermal systems modeling during various phases of the mission during reactor operations
6. Estimated cost of the development, launch, and operations of SPEAR mission

Studies into these aspects of the SPEAR probe and Europa mission have shown how successful this system will be for deep space exploration. The high science impact and low-cost Europa mission promises to reveal the ultimate questions about life in our solar system. This is all made possible by the ATEG technologies developed by Howe Industries, which has already shown the potential for advanced power generation that will revolutionize solid state energy harvesting.

### 4.1 ATEG Power Conversion System

Design, modeling, and materials testing of the ATEG conversion system was conducted by Howe Industries. This study investigated the potential to increase the efficiencies of current ATEG technologies to levels previously unknown. This technology is one of the primary drivers that makes the SPEAR probe possible. Models of ATEGs have shown the potential for power conversion efficiencies greater than 20% at the given temperatures. Materials testing validated some of the behaviors that make the ATEG technologies possible for future space exploration missions and terrestrial based power systems.

This truly novel system has shown the potential for applications in space exploration as well as terrestrial applications. Predictions show efficiencies rivaling or exceeding the performance of current nuclear power systems for space exploration. Numerous materials were identified for future studies to further validate models and create a working ATEG prototype. This investigation was led by Howe Industries and its research team.

### 4.2 Nano-reactor, Shielding, and Neutronics

Another important study was conducted into the design of a small nano-reactor capable of producing 15 kW of thermal power. This reactor, specifically designed to be lightweight and utilize low enriched uranium, provides the power necessary for SPEAR's system. The use of novel materials and LEU allows this reactor to be privately owned and operated for a multitude of other applications as well.

Investigations into shield design were also conducted to minimize shield mass but offer maximum protection for the payload going to Europa. The design of SPEAR's shield as well as propellant tanks and radiators offers a significant amount of protection for the valuable CubeSat payload. A shadow shield concept was used to protect localized areas on the spacecraft.

Several ionizing radiation environments were investigated to determine the total ionizing dose and level of shielding required to keep the scientific payload operational. This included the radiation environment around Earth,



galactic cosmic rays (GCR), solar particle events (SPE), the Europa environment, as well as the neutrons and gammas of the nuclear reactor. The Europa environment poses a significant challenge because of its extreme radiation fields producing upwards of 30 krad/day of total ionizing dose behind 2.54mm of aluminum [20]. In such an extreme environment it is expected that the CubeSats will only be able to survive for 30 days before succumbing to the radiation. Howe Industries led the investigation into the nano-reactor, shield design, and neutronics associated with this SPEAR mission.

#### **4.3 CubeSat Swarm**

The primary science mission of SPEAR was investigated to determine the validity and advantages of using a CubeSat swarm to observe Europa over a single spacecraft. Components were found to minimize cost and maximize the extraterrestrial life detection abilities of Each CubeSat. Novel lab-on-a-chip technologies will allow the CubeSats to detect the chirality of samples with high throughput capabilities.

Based on current data about Europa's plumes different mission scenarios were considered and studied to determine the most efficient method to study Europa's plumes and their contents. It is believed that by using a CubeSat swarm the life-detecting capabilities of this mission are greatly increased compared to planned missions to Europa. This investigation was led by Howe Industries and has revealed the high scientific impact potential of SPEAR's CubeSat swarm.

#### **4.4 Trajectory, Power Distribution, and Mass Budget**

Atomos Space has led the investigation into the different electric thrusters and mission trajectories for the Earth to Europa portion of the mission. Howe Industries worked with Atomos Space to develop a mass budget for the SPEAR probe based on heritage components and speculation on future components. They also developed the power management and distribution system that SPEAR will utilize throughout its journey to Europa.

#### **4.5 Thermal Management**

The Hypershield Partnership investigated the thermal management aspects of the SPEAR probe. With a large thermal load to dissipate, understanding the thermal environment of the SPEAR probe is of utmost importance. SPEAR will experience various forms of heating and thermal stress throughout its journey to Europa because of the various environments it will pass through. Investigations into the radiator and its heat piping were also undertaken to determine if SPEAR can radiate enough thermal energy to prevent critical failure of the reactor.

#### **4.6 Mission Costs**

Howe Industries investigated total costs that would be associated with the SPEAR mission. SPEAR can launch on significantly cheaper launch vehicles due to its low mass and compact form factor. The use of commercial off the shelf components and CubeSat technologies enables this mission to have a low cost but high science impact. The nano-reactor would be the first of its kind that can be privately owned by companies or individuals due to the use of low enriched uranium. The ATEGs have the potential to revolutionize power generation for spacecraft as well as terrestrial power applications.

### **5 ADVANCED THERMOELECTRIC GENERATOR DESIGN, MODELING, AND VALIDATION**

Driving the success of the SPEAR probe is the advanced thermoelectric generator (ATEG) concept theorized by Howe Industries. This system has the potential to increase current thermoelectric generator (TEG) efficiencies by two to three times. With this revolutionary technology SPEAR can produce more power than any previous deep space probe without the need for large solar panels or costly RTG power sources. This investigation will show the validity of this system and its potential to revolutionize TEG technologies to levels once thought unfeasible.



## 5.1 Thermoelectric Generator Principles

Thermoelectric technologies have been researched for many decades with new materials created to increase performance, but large advancements have yet to be realized. Thermoelectric materials are characterized by their figure of merit, which is defined in the following equation provided by [21].

$$zT = \frac{S^2 T}{\frac{\kappa}{\sigma}} \quad (1)$$

In this case  $\sigma$  is the materials electrical conductivity,  $S$ , is the materials Seebeck Coefficient,  $T$ , is the temperature, and  $\kappa$  is the materials thermal conductivity. A higher figure of merit results in a higher performing thermoelectric material. While the equation above is applicable to a single material, a thermoelectric generator typically consists of p-type and n-type semiconductors. A new figure of merit for the thermoelectric generator can be determined from the following equation provided by [21].

$$Z\bar{T} = \frac{(S_p - S_n)^2 \bar{T}}{\left( \left( \frac{\kappa_p}{\sigma_p} \right)^{\frac{1}{2}} + \left( \frac{\kappa_n}{\sigma_n} \right)^{\frac{1}{2}} \right)^2} \quad (2)$$

In this case  $\bar{T}$  is the average temperature between the hot and cold side,  $S_p, S_n, \kappa_p, \kappa_n, \sigma_p, \sigma_n$  represent the Seebeck coefficient, thermal conductivity, and electrical conductivity of the p-type and n-type materials. It is obvious from these equations that increasing the electrical conductivity, average temperature, and Seebeck coefficient, as well as decreasing the thermal conductivity, are all viable ways to increase the figure of merit. This figure of merit directly translates to the efficiency of the thermoelectric generator described in the following equation also provided by [21].

$$\eta = \frac{\Delta T}{T_h} \frac{\sqrt{1 + Z\bar{T}} - 1}{\sqrt{1 + Z\bar{T}} + \frac{T_c}{T_h}} \quad (3)$$

Where  $\eta$  is the overall conversion efficiency,  $T_h$  is the hot side temperature, and  $T_c$  is the cold side temperature of the TEG. The first portion of this equation is the Carnot Efficiency, which is the theoretical maximum that can be achieved. As  $Z\bar{T}$  approaches infinity, the conversion efficiency approaches the Carnot limit.

**Error! Reference source not found.** shows how larger figures of merit are beneficial to producing power. Current figures of merit for existing TEGs struggle to reach levels that can compete with traditional power generation systems. NASA's multi-mission radioisotope thermoelectric generator (MMRTG) and their enhanced MMRTG (eMMRTG) only have efficiency levels between 5.5%-7.4% at the beginning of their life [22]. A dynamic cycle may achieve efficiencies above to 20-25% [22] but requires working fluids and moving machinery. Increasing the temperature gradient would also increase efficiency, but this option is limited in its ability to change the efficiency due to limitations of materials and heat rejection systems.



**Figure 7: An example of efficiency levels for TEG units at different ZT values. Increasing the temperature difference of thermoelectric generators only increases the efficiency so far, where large gains in efficiency are more readily apparent by increasing the figure of merit. Plot courtesy of [23].**

## 5.2 Advanced Thermoelectric Generators

Howe Industries has examined the possibility of increasing the figure of merit of thermoelectric generators to outpace the performance of current deep space and terrestrial power generation systems. This is accomplished through the phenomena known as radiation induced conductivity (RIC) [24] [25]. In this process, ionizing radiation causes atoms in the target material to ionize and free electrons, which increases the electrical conductivity of the material. These electrons eventually return to their host nucleus, returning the electrical conductivity of the material to its original state. Radiation can be continuously applied to re-ionize the atom and maintain a constant state of elevated electrical conductivity.

The ATEG unit function by irradiating the feet of a thermoelectric generator and modifying the material properties of the feet. A source of ionization must be present for the ATEGs to function, which can be accomplished through two different methods; a radioisotope source or neutron interactions. Both methods result in ATEG units having the potential to reach comparable efficiency and power production as a traditional dynamic power cycle, but with no moving parts.

### 5.2.1 Radioisotope Source

A common source of ionizing radiation is from radioisotopes, which continuously emit ionizing radiation. Often this is in the form of an alpha particle, which has two protons and two neutrons, and is positively charged. Common radioisotopes include, plutonium-238, americium-241, and polonium-210. The energy of the alpha particle depends on the source and will typically exceed 5 MeV. Depending on the ionization energy of the foot material, these alpha particles can ionize hundreds of thousands of atoms, and each radioisotope particle can produce billions of alpha particles per second depending on its mass. With a properly designed radioisotope dopant, a continuous supply of ionized atoms and free electrons will be available within the ATEG to maintain the elevated electrical conductivity for the lifetime of the radioisotope.

Embedding these alpha particle sources inside of the ATEG is a simple matter of using hot pressing or spark plasma sintering (SPS) to introduce the particles. The hot press process involves heating and compressing powders until they are densified into a solid object, while the SPS also introduces an electric current. Depending on the material, either of these methods can be used. Radioisotope particles would simply be mixed into the powder and pressed down into a usable ATEG foot. Further investigations into the specific quantity of radioisotope needed to accomplish increased electrical conductivity will be discussed in a later section.

This type of radiation source would provide a stand-alone ATEG that would operate with higher efficiencies in accordance with its half-life. Alpha particles require little in the way of shielding, making it suitable for most applications that require solid state power production from a heat source. ATEGs could be paired with traditional heat-to-electric systems to increase their power density and expand their mission capabilities with virtually no penalty. Other advantages and disadvantages of these sources will be discussed in another section.

### 5.2.2 Neutron Interaction

The second method investigated to produce ionizing radiation is through a neutron interaction with the nucleus of an atom. When a neutron is captured by an atom, that atom undergoes transmutation and if the resultant nuclide is unstable, it will decay. In this specific case, we examined the use of boron-10 as a means to produce alpha particles through neutron absorption.  $^{10}\text{B}$  has the advantage of a very large neutron capture cross section for thermal neutrons, as well as being an abundant element in many thermoelectric materials and semi-conductor dopants. Natural boron consists mostly of  $^{11}\text{B}$  (~80%) with roughly 20% of the atoms being  $^{10}\text{B}$  [26]. When a  $^{10}\text{B}$  atom captures a neutron, it releases a 2.5 MeV alpha particle and quickly decays into lithium-7 [27]. This alpha particle behaves similar to the particles from the radioisotope sources and penetrates into the ATEG foot, thus ionizing the material and freeing electrons to increase the electrical conductivity.

$^{10}\text{B}$  has many advantages over radioisotopes. It is not inherently radioactive, it is safer to handle, and it is not regulated by the Nuclear Regulatory Commission (NRC). This allows for testing and validation of the ATEG without the need to obtain radioisotopes. In fact, Howe Industries was able to successfully test boron loaded materials in the Kansas State TRIGA reactor to investigate the RIC of a potential thermoelectric material. Results showed a drastic increase in conductivity as predicted and are discussed in more depth in a later section.

A significant disadvantage of  $^{10}\text{B}$  is that it must be paired with a neutron source for the ATEG to function properly. In the case of SPEAR, this neutron source would be the reactor powering the spacecraft. Another drawback is that the energy of the alpha particle released is roughly half that of the radioisotope alpha particle, which results in a lower penetration depth into the ATEG materials. The tradeoffs between radioisotope ATEGs and  $^{10}\text{B}$  ATEGs will be discussed in a later section.

### 5.3 ATEG Modeling

Investigation into the ATEG was performed mostly through the use of an in-house model created exclusively to predict the performance of the ATEG with a large variety of inputs. The basic operating principals behind TEGs was described in the previous sections. As stated, the most effective method to increase the efficiency of these TEGs is to change the electrical conductivity of the sample. Modification of the Seebeck coefficient and thermal conductivity due to radiation exposure has shown positive results as well [28] [29]. However, these factors would not pose as significant changes to the ATEGs efficiency as altering the materials electrical conductivity. Previous studies have shown several orders of magnitude differences in electrical conductivity, while changes in thermal conductivity and Seebeck coefficient are limited to only a few factors difference.

A key component of the model was to predict the amount of RIC dopant (radioisotope, or neutron interaction) that needed to be added to the thermoelectric material to increase its electrical conductivity to adequate levels. The volume percentage (vol%) and particle size of the RIC dopant directly impacts the electrical conductivity of the sample. Figure 8 shows an illustration of the ATEG couple with the embedded RIC dopant particles. Alpha particles are emitted and penetrate into the matrix which causes localized regions of increased conductivity shown in red. These regions of localized conductivity can overlap, increasing the amount of ionizations these areas. This further increases the electrical conductivity in that area as well. Multiple areas of overlapping RIC influenced areas connect forming a highly conductive pathway through the TEG foot. Addition of RIC dopant particles will affect the thermal conductivity, Seebeck coefficient, and electrical conductivity. A primary concern with more thermally conductivity particles, was to avoid forming a pathway through the ATEG foot of high thermally conductive particles, which would reduce the ATEGs efficiency. However, because of the volume of material under RIC influence is greater than the particle vol% this will be unlikely to occur. Areas under the influence of the ionizing radiation are also expected to experience decreases in thermal conductivity and increases in Seebeck coefficient. However, these changes were overshadowed by the more dominating change in electrical conductivity.

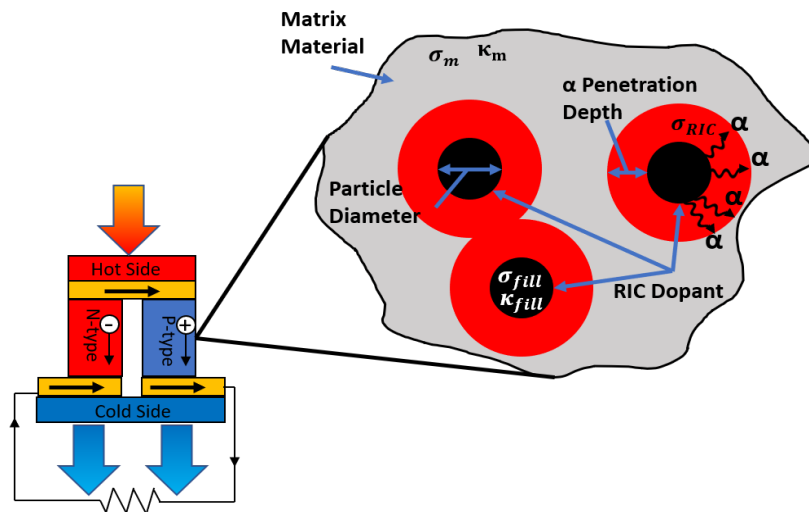


**Figure 8: ATEG thermocouple with embedded RIC dopant particles.** The RIC particles have their own thermal conductivity and electrical conductivity separate from the matrix. The matrix also has its own thermal and electrical conductivity separate from the RIC particles. The area in red is the RIC influenced area which will see localized increases in electrical conductivity greater than the surrounding matrix. This figure also illustrates how RIC influence areas can overlap forming a pathway through the material with greater electrical conductivity.

**Table 4: Alpha particle penetration depth in various thermoelectric generator materials.** Penetration depth is directly related to volume of material effected by the radiation induced conductivity. The average alpha particle energy is taken from each source and all penetration depths are represented in microns.

Material	NiO (6.67 g/cc)	SiGe (3.01 g/cc)	Bi <sub>2</sub> Te <sub>3</sub> (7.7 g/cc)	PbTe (8.16 g/cc)
<sup>238</sup> Pu (5.6 MeV)	12.4	26.2	20.3	19.7
<sup>241</sup> Am (5.5 MeV)	12	25.5	19.7	19.2
<sup>10</sup> B (2.5 MeV)	4.46	8.96	7.18	7.06

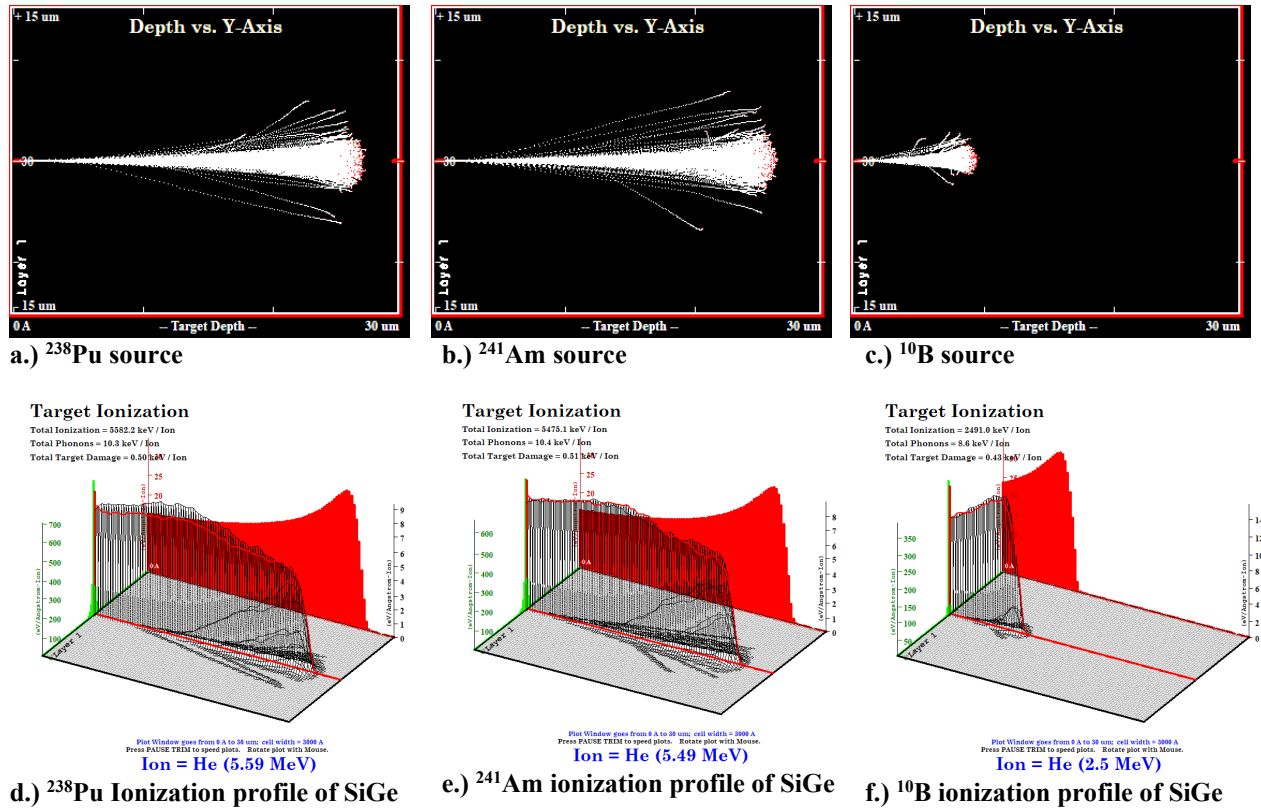


**Figure 9:** Images a-c show the penetration depth of different alpha particle sources within a SiGe TEG foot. Plots d-f show the ionization profile of each alpha particle source. It is clear that the higher energy alpha particles penetrate much further into the material, resulting in larger areas under RIC influence.

The radiation sources described in the previous section all have different alpha particle energy levels, and therefore penetrate to different depths within the thermoelectric material. This behavior is visible in Table 4 for some common thermoelectric materials. Boron, with the smallest alpha particle energy, has roughly 1/3 the penetration depth of the two radioisotope sources studied, which would require it to have a higher RIC dopant vol% to reach the same change in electrical conductivity. Figure 9 shows how the energy of the alpha particle effects the penetration depth and the number of ionizations within a SiGe matrix. A larger penetration depth can also aid in reducing the amount of radioisotope used per ATEG. Figure 5 shows the difference between a  $^{241}\text{Am}$  source and a  $^{10}\text{B}(\text{n},\alpha)$  source and its corresponding change in the volume influenced by RIC. Clearly, to reach the same RIC influence vol% a larger amount of  $^{10}\text{B}$  must be used, as the goal is to completely encompass the material under RIC influence.



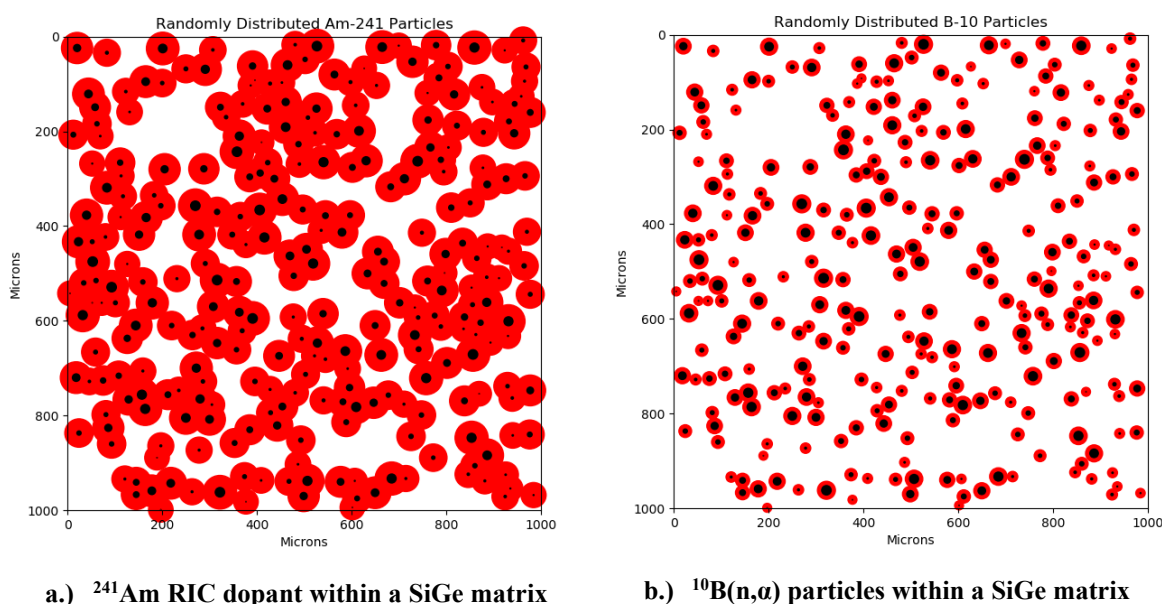


**Figure 10:** These plots show the same particle distribution, but with different RIC penetration depths due to 5.49 MeV alpha particles and 2.5 MeV particles. In order to cover the same vol% as the  $^{241}\text{Am}$  larger vol% of the  $^{10}\text{B}(n,\alpha)$  will be required.

Decreasing the RIC dopant particle sizes also has a significant effect on the electrical conductivity of the samples. If small particle sizes are used a larger volume of the ATEG foot will be under RIC influence for the same vol%. Larger particles will result in smaller vol% under RIC influence as the particles will not be as dispersed within the matrix. In samples that contain  $(n,\alpha)$  particles this holds true as well, however, particle such as  $^{10}\text{B}$  will already be atomistically distributed within the material because it is one of the elements that make up the compounds. This should yield much higher vol% under RIC influence as compared to materials made through sintering with RIC particles.

It is clear from Figure 10 that there may be areas within the matrix that have overlapping areas of RIC influence. These areas will see increases in electrical conductivity compared to other areas depending on the RIC influence areas that are overlapping. This also means that for each vol% infill and particle size distribution there will be a statistical distribution of RIC coverage that can be expected. This provides valuable information in understanding how much radioisotope of  $(n,\alpha)$  must be added to the ATEG foot to achieve the required change in electrical conductivity. These statistical distributions also aid in determining the performance of potential ATEG materials without the need to run countless simulations based on their material properties. Figure 11 shows these statistical distributions for varying particle sizes at 4 vol% infill within a PbTe ATEG foot. It is clear from this plot how the particle size effects the RIC vol% infill fraction. Smaller particle sizes help to distribute the RIC influenced areas throughout

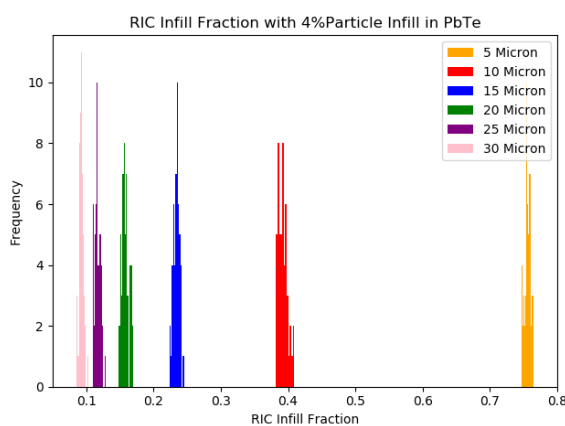


**Figure 11:** Statistical distribution of RIC influence volume coverage within a PbTe matrix. Smaller particle sizes result in larger RIC vol% for the same infill vol%. Atomistically distributed particles should result in complete RIC vol% coverage.



the material. It is clear that as the particle size decreases the RIC infill percent reaches its maximum value. With atomistic distribution, virtually the entire sample should be under RIC influence. This should be the case for the various borides and boron compounds that have been identified as potential ATEG materials discussed in a later section.

The same simulation was performed on various thermoelectric materials to study their behavior with various vol% infills, alpha sources, and particle sizes, which is visible in Figure 12. The shows how the actual ATEG foot material can affect the RIC coverage compared to others. This may be a factor in the decision to choose specific materials over one another to SPS with the alpha particle sources. It is clear from this plot that  $^{238}\text{Pu}$  and  $^{241}\text{Am}$  effect the material in a similar fashion, with the difference being the specific activity of each radioisotope. Note that this simulation was conducted at 4% infill, higher infill percentages should see much larger RIC vol% infill fractions, particularly with  $^{10}\text{B}(\text{n},\alpha)$ .

Determining the impact on the efficiency of the thermoelectric generator uses the RIC vol% infills determined from these simulations. When these particles are introduced to the ATEG matrix they affect the electrical conductivity, Seebeck coefficient, and thermal conductivity. As discussed earlier the electrical conductivity is affected the most by radiation, while the thermal conductivity and Seebeck coefficient increase but maintain the same magnitude. The particles introduced have their own electrical conductivity and thermal conductivity which can influence the new composite properties in potentially negative ways.  $^{10}\text{B}$  for example has a thermal conductivity of 27 W/mK, which is an order of magnitude higher than the ATEG materials shown in Figure 12. Thus, the addition of boron particles increases the overall thermal conductivity of the material which can negatively affect the performance of the ATEG.  $^{238}\text{Pu}$  and  $^{241}\text{Am}$  do not suffer as much from this issue as their thermal conductivities, while greater than most thermoelectric materials, are still the same order magnitude as the ATEG feet. The effects of adding the filler material were taken into consideration in this model to determine any negative effects.

The degree of conductivity changes is under investigation as significant information over a range of materials is not available. However, an experiment at Oak Ridge National Laboratory (ONRL) observed and increase of 400x in the electrical conductivity of alumina when exposed to ionizing radiation at

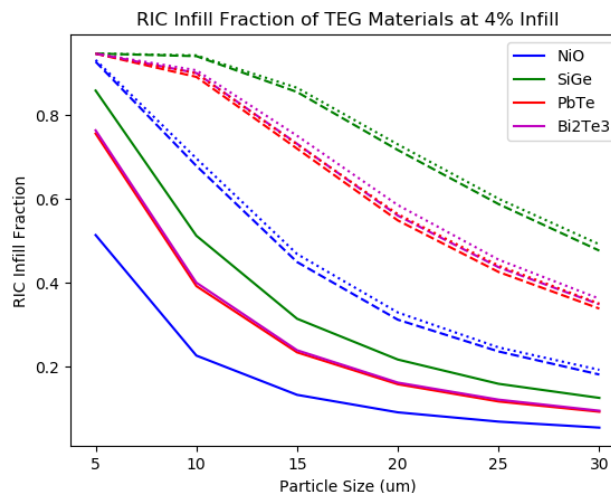


**Figure 12: Particle size, alpha source type, and ATEG foot type all effect the RIC vol% infill fraction. Solid lines represent  $^{10}\text{B}(\text{n},\alpha)$  particles, the dashed lines represent  $^{241}\text{Am}$  particles, and the dotted lines represent  $^{238}\text{Pu}$  particles.**

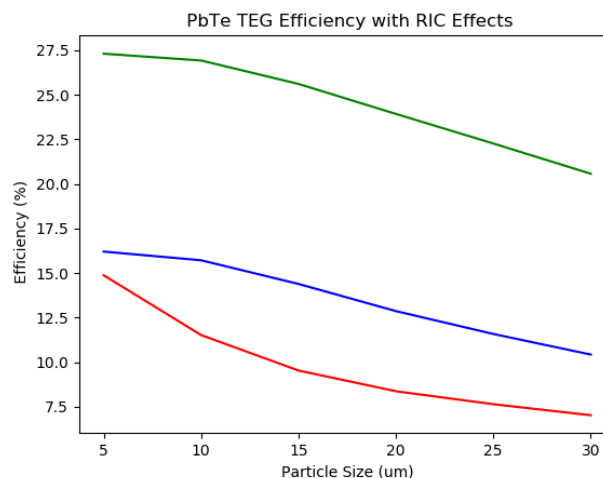


**Figure 13: Predicted PbTe enhanced efficiency due to alpha sources within its material matrix. Green represents  $^{238}\text{Pu}$ , blue represents  $^{241}\text{Am}$ , and red represents  $^{10}\text{B}$  particles. Plutonium has a higher activity level than the other sources therefore resulting in a greater change in conductivity in its influenced area.**

temperatures within our operating range [25]. Another experiment on ceramic materials observed over 10,000 times increase in electrical conductivity in a UV grade sapphire sample [24] inside a reactor core. Results from Howe Industries experiment with boron nitride will be discussed in a later section in more depth but showed a 50x increase in electrical conductivity when subjected to a neutron flux in a TRIGA reactor. Without a significant amount of testing conducted on various materials the exact influence of ionizing radiation on the conductivity of a sample is difficult to predict. A conductivity multiplier factor was applied to the material's electrical conductivity to simulate the expected change in properties until an exact solution can be experimentally determined.

The efficiency and figure of merit of the ATEG is determined from equations 2 and 3 with modifications to the thermal and electrical conductivities due to the particles' effects. These results are visible in Figure 13 for a lead telluride sample with the three alpha sources studied. Efficiencies were calculated for a standard temperature at 600 K for the hot side and 350 K for the cold side. As observed earlier smaller particles have a greater effect at increasing the electrical conductivity and therefore the efficiency. The activity of  $^{238}\text{Pu}$  is roughly five times greater than that of  $^{241}\text{Am}$  for an equivalent mass. This means that the material around the  $^{238}\text{Pu}$  should see a higher dose which is directly linked to the conductivity multiplier.  $^{10}\text{B}$ 's activity is dependent on the neutron source flux, in this case the assumed radioactivity matched that of  $^{241}\text{Am}$ . Figure 13 shows this relationship with  $^{238}\text{Pu}$  having a greater efficiency due to its higher electrical conductivity. In this case, a conductivity multiplier of 10 was used to simulate the effects of RIC. It is clear from this plot that plutonium has a greater effect on increasing the efficiency because of its increased reactivity while the other two alpha sources show lower activity levels. Because of the lower RIC vol% infill  $^{10}\text{B}(n,\alpha)$  did not match that of  $^{241}\text{Am}$  which had a higher vol% coverage. Figure 14 shows the associated figures of merit for the ATEG couple. It can be seen that significantly larger figures of merits can be reached than previously possible through conventional TEG technologies, even though the conductivity multiplier used to simulate this ATEG was significantly lower than that of previous studies on other materials. It is unknown how some of these materials will react to ionizing radiation from the alpha particles. However, it has been observed that changes in conductivity on the level observed by ORNL are not necessary to raise the efficiency of the thermoelectric material above 20-25%. This is visible in Figure 15 where the conductivity multiplier has been plotted against the change in figure of merit and the efficiency of a PbTe-PbTe ATEG. One can clearly see that changes of 25-50 times the normal conductivity can yield drastic changes in efficiency and figure of merit. At changes in conductivity seen in with Oak Ridge National Laboratory the efficiency would increase to 40.8%, which is roughly 98% that of the Carnot efficiency.

This multiplication factor would coincide with a large dose of radiation. Radioisotope particles will have a continued dose rate that slowly decays over time in conjunction with their half-life. Meaning that they will never

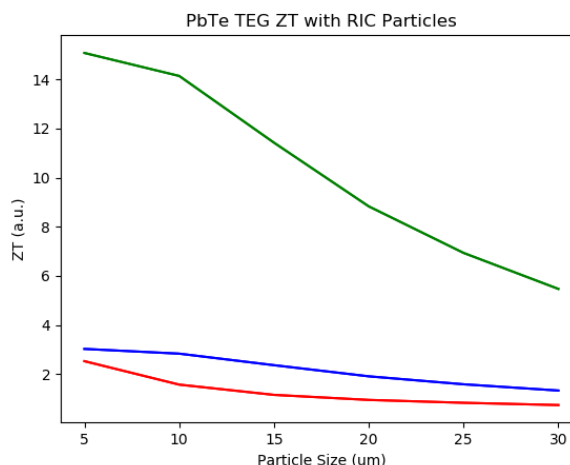


**Figure 14: Figures of merit associated with the ATEG created from PbTe materials with the alpha source particles. Reaching higher levels of efficiency requires larger figures of merit.**

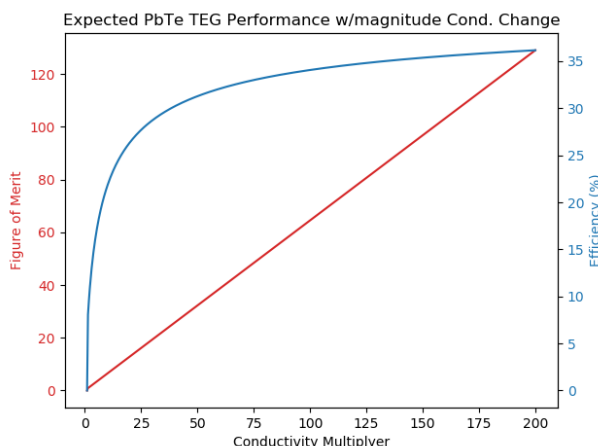


**Figure 15: Large increases in efficiency and figure of merit occur at relatively small changes in conductivity.**

exceed the expected efficiency based on their conductivity multiplier and their RIC coverage area. With a  $(n,\alpha)$  particle such as  $^{10}\text{B}$ , the dose rate can be increased and decreased depending on the desired efficiency. This is because the alpha particle dose is dependent on the neutron flux, which can be adjusted inside of the reactor. Simply increasing and decreasing the neutron flux will change the electrical conductivity of the ATEG which would not be possible with a constant radiation source such as the radioisotopes.

Utilizing the simulations and models derived above Howe Industries has developed a comprehensive ATEG tool to determine performance characteristics and physical properties of the ATEGs. This tool has shown that these ATEGs have the capability of reaching extremely high efficiencies. Models have exceeded the expectation of reaching efficiency values of 20% with all three alpha sources. Figure 16 shows one such ATEG with a PbTe as the p-type and n-type foot with a  $^{10}\text{B}(n,\alpha)$  source with a conductivity multiplication factor of 50 and a 7% volume infill. At the temperature gradient we expect for our mission we should be able to reach an expected efficiency of 30% for this ATEG. Variation in the figure of merit plot is due to the thermoelectric property dependence on temperature in PbTe. These results are the cornerstone of this mission and future deep space exploration missions that require high power density sources with no moving parts. The power derived from the ATEG can be determined from the following equations provided by [30]:

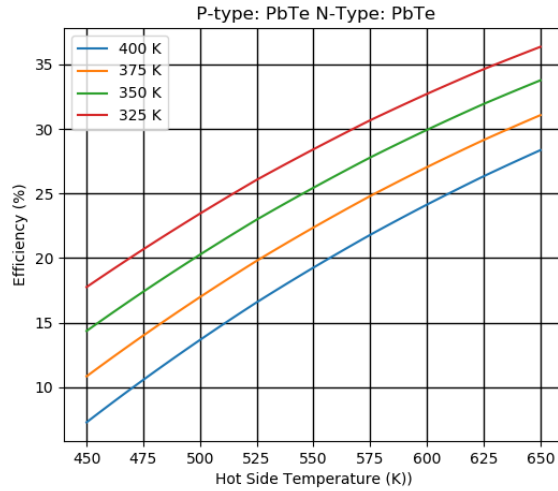
$$\alpha = \alpha_p - \alpha_n \quad (4)$$

Where  $p$  and  $n$  denotes the p-type and n-type material and  $\alpha$  represents the Seebeck coefficient. The total resistance of the thermoelectric couple must also be determined from the following equation:

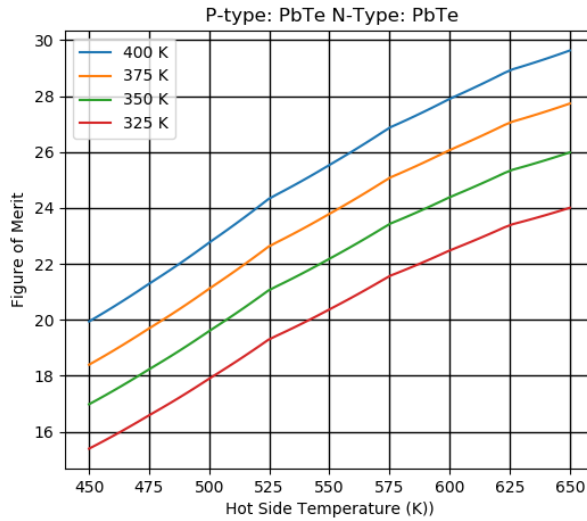
$$R = \frac{\rho_p L_p}{A_p} + \frac{\rho_n L_n}{A_n} \quad (5)$$

Where  $\rho$  is the materials electrical resistance (note conductance is the reciprocal of this),  $L$  is the length of thermoelectric material, and  $A$  is the cross sectional area of the thermoelectric foot. The thermal conductivity of couple can also be determined from the following equation:

$$\kappa = \frac{\kappa_p A_p}{L_p} + \frac{\kappa_n A_n}{L_n} \quad (6)$$



a.) Efficiency of PbTe ATEG with ~30% efficiency with mission temperature gradient.



b.) Figure of merit of PbTe ATEG exceeding any currently available ZT value.

**Figure 16: This figure depicts the performance of a PbTe ATEG under various temperature gradients. Variation in plot is due to temperature dependent material properties of PbTe.**

Where  $\kappa$  is the thermal conductivity of the specific material. Voltage produced by the ATEG is a function of the Seebeck coefficient, ATEG resistance, load resistance and the number of couples in the ATEG. Current is dependent on the same parameters as the voltage. The following equation describes these relationships also provided by [30]:

$$V = \frac{n\alpha(T_h - T_c)}{\frac{R_L}{R} + 1} \left( \frac{R_L}{R} \right) \quad (7)$$

$$I = \frac{\alpha(T_h - T_c)}{R_L + R} \quad (8)$$

In this case  $R_L$  denotes the load resistance; maximum power is reached when the load resistance matches the ATEG internal resistance resulting in the following equations for current, voltage and power:

$$V = \frac{n\alpha(T_h - T_c)}{2} \quad (9)$$

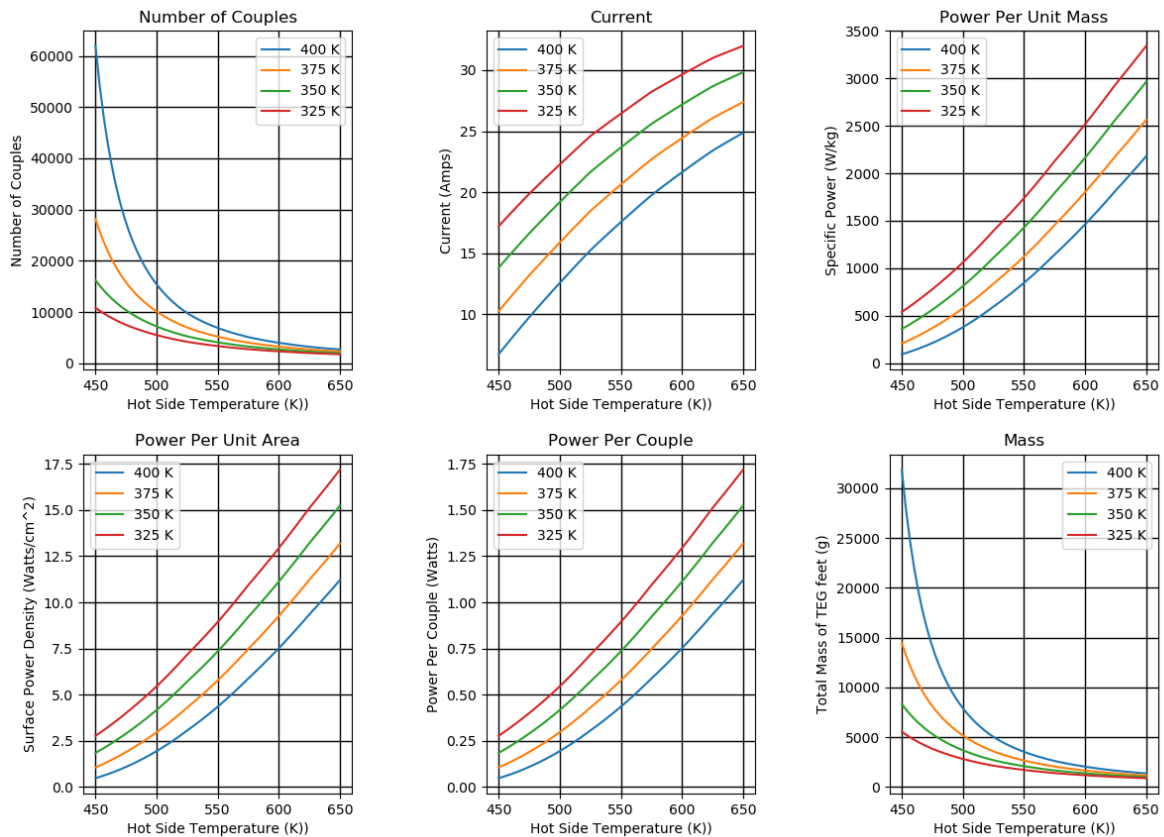


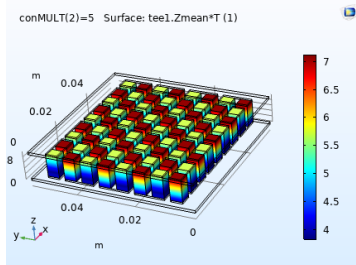
**Figure 17: Performance characteristics of an ATEG system that produces 3kW of electrical power. Note that masses are of the ATEG only and do not represent overall power production system. ATEG feet used at n-type and p-type PbTe with 7 vol% infill and a 40 times conductivity multiplier.**

$$I = \frac{\alpha(T_h - T_c)}{2R} \quad (10)$$

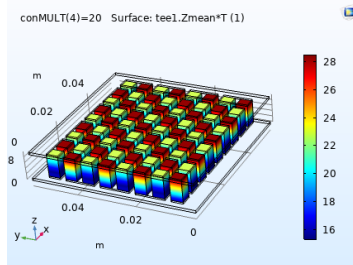
$$P = \frac{n\alpha^2(T_h - T_c)^2}{4R} \quad (11)$$

In equation 11 one can clearly see that to increase power the resistance of the system must be lowered while Seebeck coefficient and temperature gradient must be increased. These equations can be used to determine several key parameters of the ATEG power system. Figure 17 shows several plots derived from these equations and properties of the thermoelectric generator. In these figures the mass of the ATEG is determined through the physical properties of the ATEG feet materials and current ATEG technologies (primarily for the insulators, conductive connectors and solder). This results in a high specific power as only the weight of the ATEGs are taken into consideration with this calculation. The ATEG conversion system mass is miniscule compared to the reactor mass and collect a large amount of power for a given surface area. Calculations for the figure above only take into account ATEG couples connected in series. A more realistic system would see ATEGs connected in a system of series and parallel connections to introduce some redundancy within the system in case of failures in the ATEG coupler connections. This would increase system mass slightly, but this does not appear to be a major system driver. In some of the ATEG materials the addition of the RIC filler actually decreases the mass of the system slightly, specifically with  $^{10}\text{B}$  which is much lighter than most of its ATEG matrices.

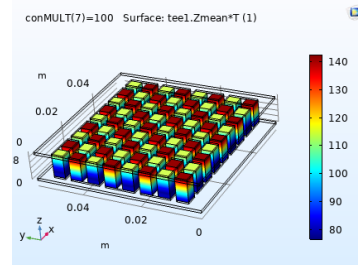
These systems were also validated in COMSOL to show how an increase in conductivity will affect an assembled ATEG. The material conductivity values were changed in a similar manner to show the RIC particles would affect the thermoelectric generator. Figure 18 shows how the figure of merit and the efficiency changed as the degree of conductivity change was increased. It should be noted that the original figure of merit range was between 0.8 and 1.4 for this ATEG combination of bismuth telluride p-type and n-type while the efficiency varied between 8-11%.



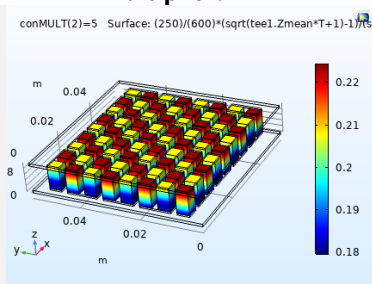
a.) Figure of Merit for 5 times conductivity multiplier.



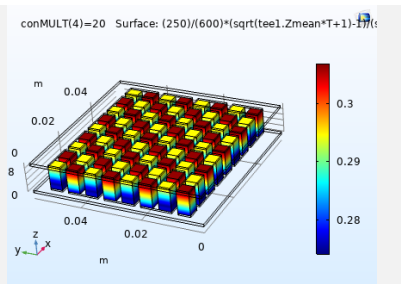
b.) Figure of Merit for 20 times conductivity multiplier.



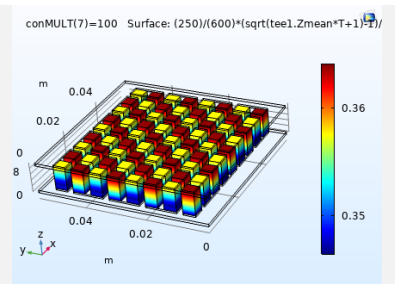
c.) Figure of Merit for 100 times conductivity multiplier.



d.) Efficiency for a 5 times conductivity multiplier



e.) Efficiency for a 20 times multiplication factor.



f.) Efficiency for a 100 times multiplication factor.

**Figure 18: COMSOL Simulations of a  $\text{Bi}_2\text{Te}_3$  p-type and n-type ATEG with applied conductivity changes ranging from 5 to 100. Large increases in figure of merit and the efficiency can be seen. Original figures of merit and efficiency were between 0.8-1.4 and 8-11%.**



Even with a conductivity increase of only 5x, the figure of merit and efficiency increased to between 4-7 and 18-22%. Larger increases in efficiency and figure of merit are seen with modest increases well below literature values.

## 5.4 Experimental Results

Howe Industries conducted experiments to validate radiation induced conductivity in potential thermoelectric materials. While the most heavily documented RIC cases have involved aluminum oxide and other insulators, none of them contained  $^{10}\text{B}$  for an alpha source. Boron nitride (BN) was chosen as the material to be tested for its potential to demonstrate the key concept of the (n, $\alpha$ ) source, and that it is considered a wide band gap insulator. Within the BN, 20% of the boron content would comprise  $^{10}\text{B}$  which should have a uniform distribution throughout the compound. A TRIGA Mark II Nuclear Research Reactor at Kansas State University (KSU) was used as a neutron source to generate the alpha particles. Leads were attached to the BN sample to take in-situ conductivity measurements while the reactor was being operated. Contained within a polyethylene container the BN sample was subjected to the neutron flux at various power levels to determine its resistive response.

An insulation resistance meter was utilized to determine the resistance of the material. The initial resistance of the sample was just over 4 G $\Omega$  and slowly rose to above 5 G $\Omega$  before the RIC effects were visible. This effect is visible in Figure 19 with power intervals marked between dashed lines. Insulators typically exhibit an increase in resistivity as they are measured from capacitive effects which was observed during this experiment and previous experiments observed without a neutron flux. An initial decrease in resistance is observed as the reactor is stepped up to 40 Watts. As the reactor power increases to 160 Watts a more noticeable drop in resistance is visible. This trend continues as the power/neutron flux increases. Larger jumps in resistance appear to be more prevalent at lower increases in power.

Boron Nitride was tested up to  $\frac{1}{2}$  MW to determine its resistance response at this power/flux level. Figure 20 shows the entire test which was conducted over the course of one hour. After the reactor reached a level of 20 kW and was held for a short period of time, a control rod was removed as the reactor was ramped up to

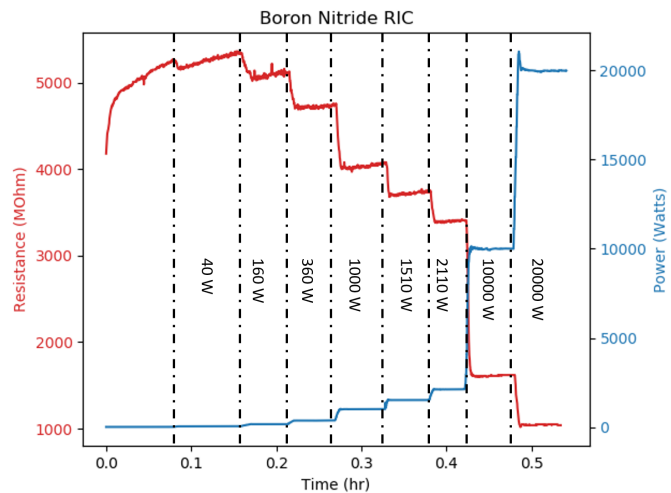


**Figure 19: Boron Nitride resistance effects due to neutron flux from nuclear reactor. Clear dependence on neutron flux is shown as resistance decreases with increases in power. Shown here is the power between 0W to 20 kW of thermal power.**

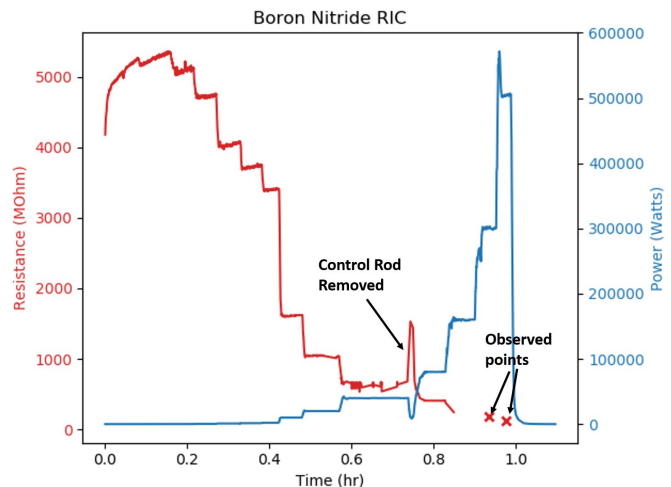


**Figure 20: Boron Nitride complete test up to  $\frac{1}{2}$  Mega-Watt power level observing  $\sim 50$  times conductivity multiplier. Previous data shows that a 50 times conductivity multiplier is more than suitable to significantly change the performance of an ATEG.**

40 kW. This caused a decrease in reactor power which also resulted in an increase in conductivity. This again shows an extremely responsive relationship to the reactors power level/ neutron flux. Power levels were increased again to 80 kW, 160 kW, 300 kW and finally 540 kW. During this time the resistance meter stopped recording but continued to display resistance. Personnel, except the reactor supervisor, were stationed inside of the control room and away from the meter and were unable to manually restart it. However, the reactor supervisor relayed data points at 300 kW and 540 kW, which were 183 MOhm and 140 MOhm respectively. These points have been marked on figure 15 to show their respective position at that power level. It is clear from these plots that the increase in conductivity is not linear with the increase in power. At smaller activity levels within the reactor there were larger gains in conductivity observed. This bodes well showing that large changes in conductivity are likely especially at power/flux levels that the SPEAR reactor will produce. While BN is not typically used as a thermoelectric material there have been several studies that show its potential.

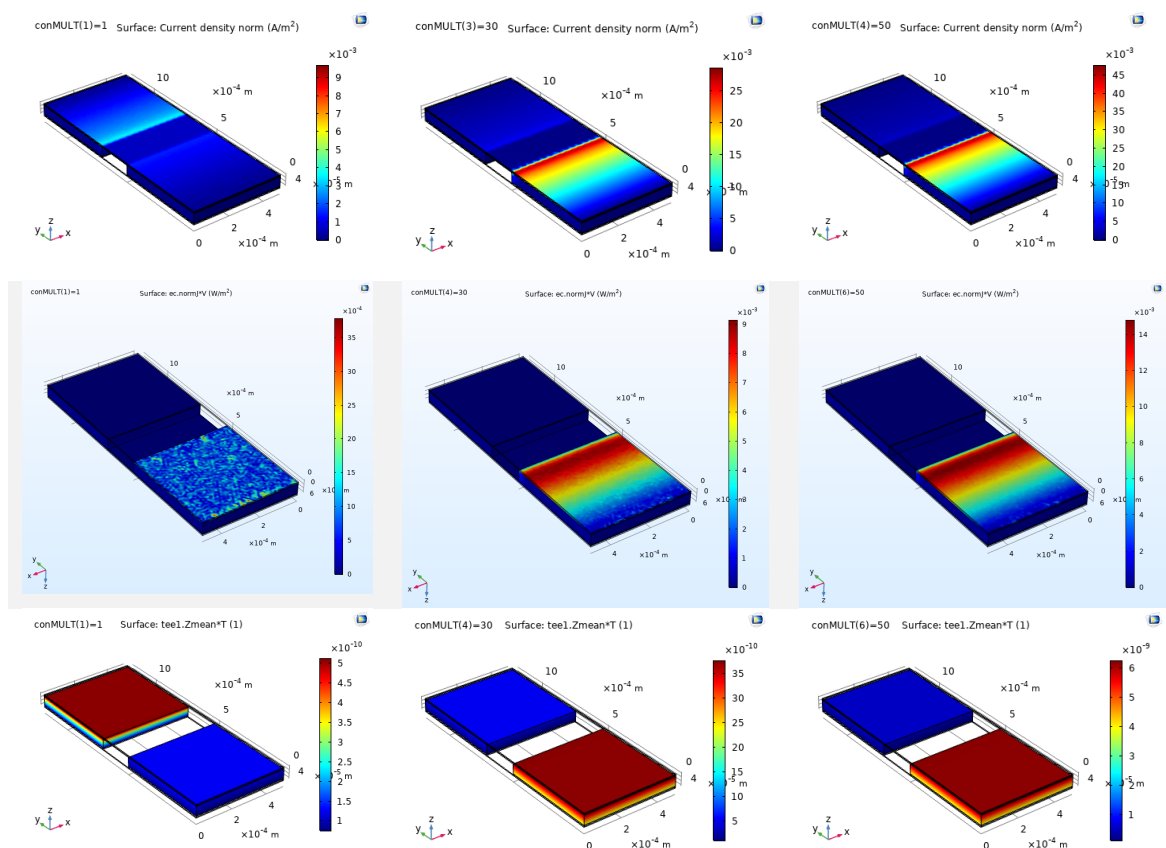


**Figure 21: COMSOL modeling results for a BN thermoelectric junction for conductivity multipliers of 1, 30, and 50x. Current density, power levels, and ZT values all improve drastically with the increased conductivity values measured at the KSU reactor.**

Although the 400-10,000x increase in electrical conductivity was not observed by the BN in this experiment, there was at least a ~50x increase in electrical conductivity observed. Referencing Figure 15, this slight increase in conductivity could be enough to reach efficiency values greater than 20% depending on other material properties.

With a highly resistive material the efficiency of the thermoelectric generator is very small. However, there should be a slight but noticeable change in voltage/power/current from the ATEG couple. While Seebeck coefficients for most thermoelectric and semiconductors are known, Seebeck coefficients for insulators are less studied, therefore Seebeck coefficients for BN were estimated from literature values. COMSOL was used to simulate an ATEG couple that could produce power on the micro-Watt scale based on known and estimated thermoelectric properties of BN. The results of this brief study are visible in Figure 21. Voltage is not shown, as this is dependent on the Seebeck

coefficient and maintained a consistent 0.4V drop. All simulations were conducted with a 600K hot side and a 350 K cold side. From this model, it can be seen that there are noticeable changes to current, power levels, and ZT values with increases in conductivity. BN, pending further investigation into Seebeck coefficient, is considered the p-type foot, while the n-type foot was modeled as SiGe. This system could be easily created and tested within the KSU reactor to determine the performance of the thermoelectric generator. This would prove the validity of the ATEG system and could be accomplished in a phase II study.

## 5.5 Potential ATEG Materials

Many of the thermoelectric materials described in the sections above must be created via SPS if they are to be created with the radioisotope or the  $(n,\alpha)$  if not already embedded within the material. While the radioisotope embedded ATEGs can operate without a reactor the availability of radioisotopes for phase II studies is unknown. Creating materials with  $^{10}\text{B}(n,\alpha)$  sources is much more practical from a phase II study point of view. However, several thermoelectric materials with  $^{10}\text{B}(n,\alpha)$  have already been studied and can be obtained for future experiments. In addition to this a few thermoelectric materials containing BN in the form of quantum dots, thin films, and nano-ribbons/tubes have been studied [31] [32]. This is advantageous as our BN experiment has already shown the potential to take bulk BN material and increase its electrical conductivity significantly.

Zhou et al. has shown that a ZT of 2.5 is possible with graphene/h-BN (hexagonal BN) superlattice monolayers [33]. If the changes in conductivity observed from the KSU experiment hold true for BN to this superlattice, a ZT potential of greater than 100 is theoretically possible which corresponds to an efficiency of 35% with SPEAR's temperature gradient. This would far exceed any thermoelectric technologies currently available. In another study conducted by Algharagholy et al. involving graphene-boron nitride hetero-structures of various widths a ZT value of 0.9 was theoretically possible [34]. Again, if the same change in conductivity is observed as the BN experiment, this would result in a ZT value of >40 corresponding to a 32% efficiency. It would appear that despite BN's poor bulk thermoelectric properties, their use inside the technologies above can increase ZT values to usable levels, and potential RIC behavior cross over to these materials can accelerate these values beyond what was previously thought possible. The current record ZT value of 7.4 was measured in hybrid  $\text{MoS}_2/\text{MoSe}_2$  nanoribbons at 800K by Ouyang et al [35]. Howe Industries ATEG technologies and projections with BN alone would significantly pass this record.

Other materials containing boron have been extensively studied for their potential use in thermoelectric generators. Many of them are on the cusp of high ZT values, most being held back by lower than average electrical

Figure available in  
source cited

Figure available in  
source cited

**Figure 22: Results of previous work involving boron based thermoelectric materials. These materials are predicted to behave exemplary when augmented with RIC. Plots courtesy of [36].**



conductivities for thermoelectric materials. One such material,  $\text{AlMgB}_{14}$  has been shown to have high Seebeck coefficients and moderate electrical conductivities based on its mixture ratios. Miura et al. has shown that  $\text{AlMgB}_{14}$  can reach Seebeck coefficients in upwards of 250-450  $\mu\text{V/K}$  which is competitive with most thermoelectric materials [36]. An even more interesting aspect of this is that through slight changes in material composition during the SPS process Miura et al. was able to create an  $\text{AlMgB}_{14}$  sample with a -500  $\mu\text{V/K}$  seebeck coefficient. Meaning that an ATEG could be created with virtually the same material, limiting issues with thermal expansion coefficients and other stresses that the ATEG might endure with varying ATEG feet. The varying Seebeck Coefficient and electrical conductivity from their work is visible in Figure 22. It is clear from this figure that the Seebeck coefficients are very high for this material, however, the electrical conductivity is much lower compared to traditional thermoelectric materials such as  $\text{PbTe}$  and  $\text{SiGe}$ . While the electrical conductivity restricts the efficiency of this material, it has been shown that slight changes in its composition can have drastic changes in these levels. Combined with RIC enhancing effects this could result in a much higher efficiency and ZT value.  $\text{AlMgB}_{14}$  is also advantageous in that the materials are not considered rare earth borides (REB) making production cheaper and more sustainable on a larger scale.

While  $\text{AlMgB}_{14}$  has a great potential for thermoelectrics at a sustainable and economical price point, there are several other REBs that sit on the cusp of advancing thermoelectric technologies. Materials identified with the greatest potential for ATEG feet include  $\text{ErB}_{66}\text{Si}_2$ ,  $\text{YB}_{66}$ ,  $\text{YB}_{44}\text{Si}_2$ ,  $\text{SmB}_{60}$ ,  $\text{SmB}_{62}$ ,  $\text{TbB}_{44}\text{Si}_2$ , and  $\text{ErB}_{66}$ . The thermoelectric properties of these materials can be found in Table 5. While these materials are not currently considered high performing TEGs, with modification to their electrical properties via RIC they can reach high ZT values making them promising candidates for ATEGs.

**Table 5: Material properties for various rare earth borides that can potentially be used as advanced thermoelectric generators. These materials are mostly held back due to their higher electrical resistivity compared to traditional TEG materials. It is predicted that they will behave more like an insulator than traditional TEG materials so changes in conductivity should be more noticeable. Small changes in conductivity are enough to achieve noticeably large increases in efficiency.**

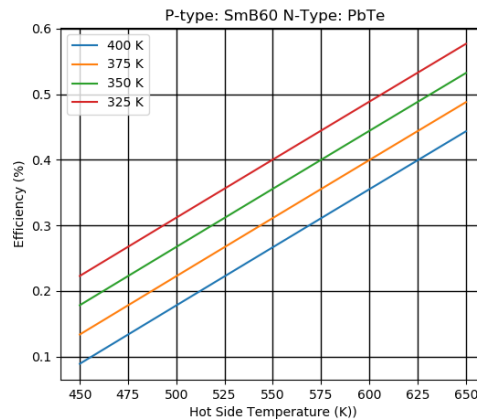
Material	Seebeck Coefficient	Thermal Conductivity	Electrical Resistance
$\text{ErB}_{44}\text{Si}_2$	50-220 [37]	1.6-2.7 [37]	0.0087-135 [38]
$\text{YB}_{66}$	205-752 [39]	2.49-3.74 [39]	0.0035-157 [39]
$\text{YB}_{44}\text{Si}_2$	80-200 [38]	~2.7 [38]	9e-4-0.02 [38]
$\text{SmB}_{60}$	197-567 [39]	2.53-3.17 [39]	1.33e-4-0.332 [39]
$\text{SmB}_{62}$	207-557 [39]	2.06-2.76 [39]	1.54e-4-0.625 [39]
$\text{TbB}_{44}\text{Si}_2$	70-140 [38]	~2.7 [38]	9e-4-0.0045 [38]
$\text{ErB}_{66}$	200-700 [38]	~2.7 [38]	0.0085-207 [38]

These materials, if shown that they cannot reach the required conductivity levels to increase the ZT to the required levels for SPEAR, can still demonstrate the RICs ability to increase ZT substantially with the change in conductivity observed by the BN. If the conductivity change matches closer to the alumina samples, the conductivity should reach into efficiencies greater than 20%. Figure 23 shows a simulation conducted with  $\text{SmB}_{60}$  with various levels of conductivity applied. It is clear that the efficiency without RIC effects applied is lower than current TEG technologies. With the same change in conductivity applied to the ATEG as was observed in the KSU experiment the efficiency increases to levels matching current technology capabilities. This makes it a very promising candidate for phase II experiments within a nuclear reactor with a single couple or a complete ATEG. At RIC conductivity changes seen with previous alumina data large increases efficiency are feasible reaching far beyond current technology standards.  $\text{SmB}_{60}$ , as well as other REB, excel at high temperatures, which as a result of larger temperature gradients would increase the expected conductivity even further. The higher electrical resistance of these materials brings them closer to being insulators than the traditional thermoelectric materials. This fact may lead them to behave in a similar fashion to the alumina and BN where RIC was observed in these insulators.

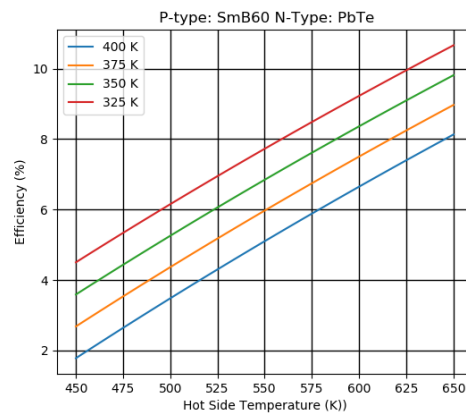
The technology behind ATEGs shows great promise in expanding upon the efficiency of current TEG technologies. This enables the SPEAR mission to maintain its very low mass and propel itself with NEP to Europa. Improving the amount of power extracted via solid-state energy methods has untold scientific benefits for deep space missions. Howe Industries has modeled and shown the potential for ATEG technologies to become a game changing reality for future space exploration. Further material tests need to be conducted to further validate and create a working ATEG for these missions.

## 5.6 ATEG Conversion System Conclusions

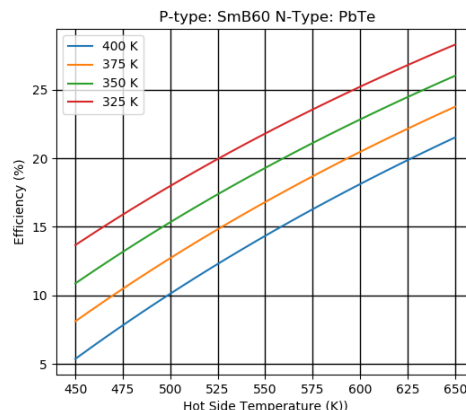
The effects of radiation induced conductivity were shown experimentally in a neutron field at KSU, and the electrical conductivity of the boron nitride did indeed change by up to 50x. BN thin film thermoelectrics currently exist and if they benefit from this change as modeled, they may become viable ATEGs. Other boron based TEGs are likely to be greatly enhanced as well, as their electrical conductivity is often their weakness and the RIC will improve this. Phase II efforts will involve further exploration potential ATEG materials, as well as empirical demonstrations of boron and boron based TEGs in a neutron field to show results. A suite of suitable materials could be tested at the KSU reactor in a similar fashion as the BN. With this material sweep, Howe Industries could further validate its ATEG models and begin the construction of a ATEG prototype. In the second year of a Phase II proposal Howe Industries, believes it would be able to create a working ATEG prototype and test its potential within the KSU reactor or other facilities with suitable neutron fields. If successful this would prove an astonishing breakthrough in thermoelectric materials and spaced-based power production.



- a.) SmB<sub>60</sub> paired with a n-type PbTe with no RIC effects applied. This results in a relatively low efficiency because of the relatively high resistance of SmB<sub>60</sub>.



- b.) RIC multiplier equivalent to the BN at KSU applied showing a large increase in efficiency that would be noticeable in an experiment.



- c.) RIC multiplier equivalent to 400 times applied to the material. Efficiencies far exceed traditional TEGs

Figure 23: Computational modeling results for a rare earth boron based ATEGs at different levels of RIC.

## 6 REACTOR AND RADIATION SHIELD DESIGN

SPEAR faces very unique radiation environments from its own power source as well as the different environments it will encounter. The reactor has been designed in such a way to maintain criticality at moderate temperatures. These temperatures are comparable to RTGs and contribute to its successful design as a lightweight reactor that can produce a significant amount of power due to the ATEG power conversion system.

SPEAR utilizes its geometry and radiation shield to protect the valuable payload from the reactor during operation. This was modeled to determine the expected dose rate for the CubeSats. SPEAR will also be subject to various radiation environments throughout its journey to Europa. The most prominent being the Van Allen Radiation belts as well as the powerful Jovian radiation fields. These radiation environments were studied to determine how they will affect the spacecraft as well as the CubeSats once they are deployed in Europa orbit.

### 6.1 Reactor Design

The SPEAR nano-reactor produces 15kW of thermal power and utilizing the ATEG power conversion system is estimated to produce 3kW of electrical power with a minimum conversion efficiency of 20%. This is a conservative estimate and our studies have shown the potential for up to 30% efficiency for 4500 kW of electrical power. The unique choice of materials and geometry of the reactor make it uniquely suited to produce this power in a relatively small form factor with low enriched uranium.

The underlying concept behind the reactor design is to decrease the mass by using the high efficiency ATEGs, new materials, and a custom design. With the increased efficiency of the ATEGs, the SPEAR reactor does not require extremely high operating temperatures that often accompany dynamic cycles. The conversion system was designed to be on the same temperature scale as an MMRTG, which also uses TEG conversion, and the hot and cold sides are 600K and 350K, respectively. This allows for lithium hydride to be used as a moderator material instead of zirconium carbide. LiH is a very effective moderator due to its low Z number constituents but is usually not considered for nuclear applications due to the low melting temperature. The SPEAR is also able to use uranium metal instead of a carbide or oxide form, which keeps design simple and reduces unnecessary mass. By taking these steps to shrink the reactor mass down as far as possible, the entire ship, propellant, and payload masses can be reduced to create the small and affordable spacecraft.

#### 6.1.1 Geometry Selection

The scale of reactor components was determined through trials in Monte Carlo Neutral Particle code, version six (MCNP6). The design goal was to create the smallest possible reactor to reach a criticality greater than one. Other considerations include heat pipe spacing, mass efficiency, and manufacturability. Trials in MCNP6 were most successful the closer the overall dimensions were to equal. This is to say the ratio of reactor criticality per unit volume tended to be higher when the base, width, and height were similar. The final iteration of the geometry produced the following results in MCNP6 visible in **Error! Reference source not found.**

**Table 6: MCNP6 Results for final geometry sizing.**

Control Rod State	Steady State Criticality	Standard Deviation	Total Number of Cycles	Number of Initial Cycles Discarded
No Insertion	1.01437	0.00012	500	100
Fully Inserted	0.98793	0.00011	500	100

The reactor was organized cylindrically to promote radial symmetry of the layers of moderator, fissionable material, and heat pipes which is visible in Figure 25 and Figure 24. This would help reduce the presence of heat concentrations throughout the reactor. This also permitted a single control rod to bring the system criticality below one when placed in the very center, the point of maximum neutron flux. A single control rod reduces complexities involved with controlling the reactor and reduces failure modes that a multi-control rod system may see. This is paramount in such a mission with a relatively long operating period. Prior to activation of the reactor in LEO the control rod will be fully inserted to prevent fission from occurring.



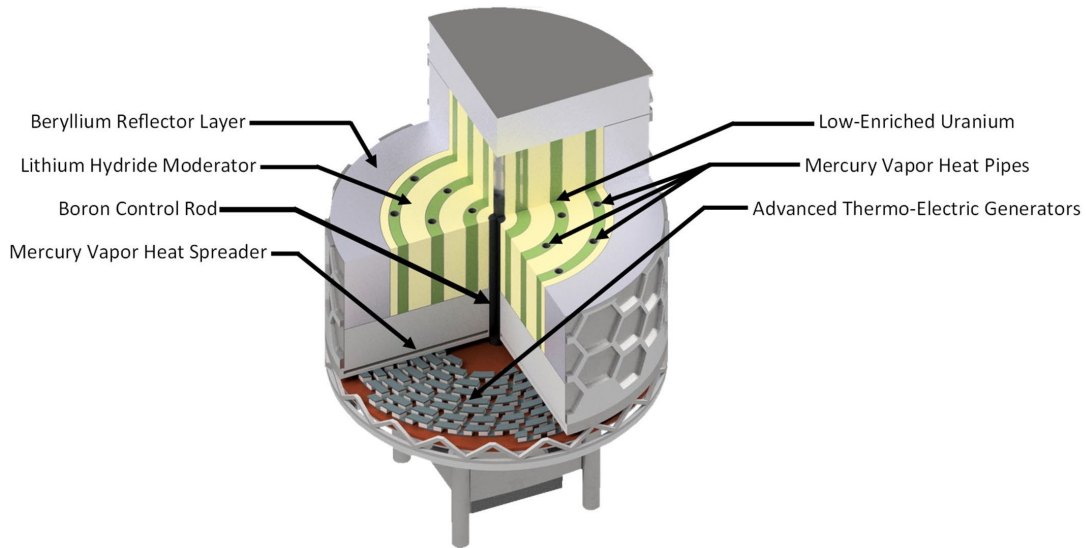


**Figure 25:** Cutaway view of the SPEAR reactor with heat pipes, moderators, reflectors, control rod and low enriched uranium fuel. The hot side of the ATEGs are connected to the mercury heat plate while the cold side are connected to the heat rejection system connected to the radiators along the side of the spacecraft.

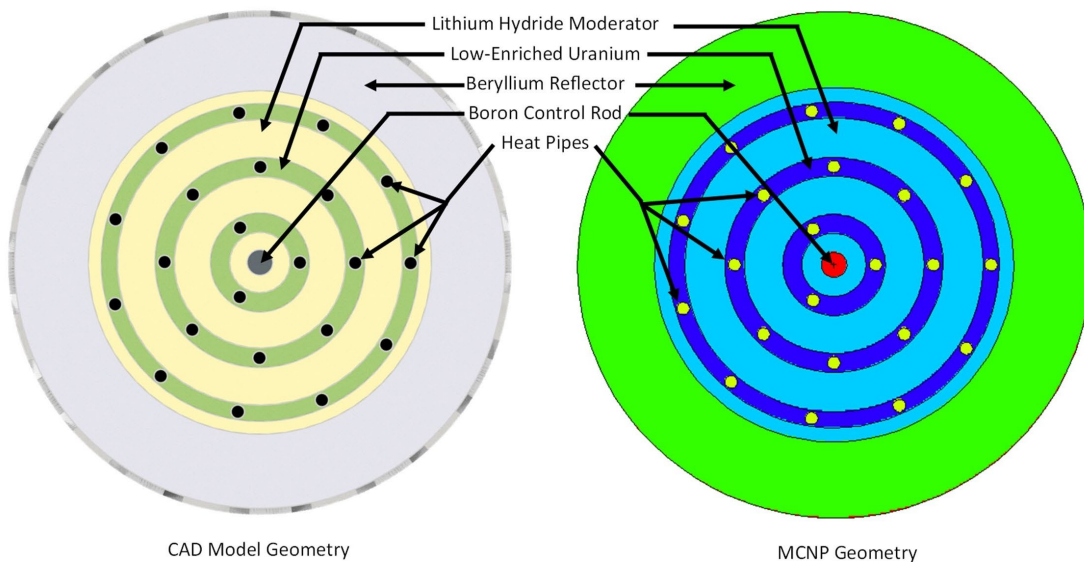


**Figure 24:** Diagram of reactor layout with labelled components as it was entered into MCNP6. The LEU and LiH moderator are organized into concentric rings with equally spaced heat pipes embedded into the LEU. The boron control rod is located at the very center. The entire system is encased in a beryllium reflector layer.

The limiting factor in this design is the maximum temperature reached by the uranium fuel during operation. If the fuel reaches high enough temperatures, it will dissociate the LiH moderator and negatively affect performance. Uranium metal has a rather poor thermal conductivity, and heat pipes were required to be placed close together to

avoid going over the maximum allowable temperature. Doping the fuel rings with a small amount of alloying material may allow for increased thermal conductivity, and thus fewer heat pipes. Geometric optimization of the core could also assist in this aspect, as rings are neutronically functional but potentially not ideal for heat transport. Both of these aspects will be investigated in Phase II.

A mass budget estimate was generated according to the material requirements and sizing of the MCNP model and is visible in Table 7. Assumptions disregard the negligible mass contribution of the internal thin walls for the physical separation of the reactor component materials. The mercury heat pipes contain a mixture of vapor and liquid, but for simplification were approximated to be full density. The heat pipe walls, and internal structure were also approximated to be mercury. As mercury is very dense compared to structural metals, these approximations are both overestimations.

**Table 7: Mass budget estimate broken down by component.**

Component	Quantity	Outer Diameter (cm)	Inner Diameter (cm)	Length (cm)	Volume (cm <sup>3</sup> )	Density (g/cm <sup>3</sup> )	Mass (kg)
Beryllium	1	40	28	20	12817.70	1.85	23.71
Lithium Hydride Ring 1	1	5	1	20	376.99	0.82	0.31
Lithium Hydride Ring 2	1	14	8	20	2073.45	0.82	1.70
Lithium Hydride Ring 3	1	23.25	17	20	3951.53	0.82	3.24
Lithium Hydride Ring 4	1	28	25.75	20	1899.68	0.82	1.56
Uranium Ring 1	1	8	5	20	612.61	19.1	11.70
Uranium Ring 2	1	17	14	20	1460.84	19.1	27.90
Uranium Ring 3	1	25.75	23.25	20	1924.23	19.1	36.75
Mercury Heat Pipes	22	1	0	32	25.13	13.56	7.50
Beryllium Caps	2	40	0	6	7539.82	1.85	27.90
Boron Control Rod	1	2	0	20	62.83	2.37	0.15
						Total Mass (kg)	142.42
						Total LEU Mass (kg)	76.36

### 6.1.2 Reactor Materials

The reactor core will be composed of conventional reactor materials, such as low-enriched uranium, lithium hydride, beryllium, and boron. Everything will be contained using aluminum for its high strength to weight and resistance to neutron damage. The heat pipes will use mercury as the working fluid, matched to the planned operational temperature of the reactor of 600K.





### 6.1.3 Advantages of LEU

Low-Enriched Uranium (LEU) consists of <20% U-235, with the remainder being U-238 [40]. Highly Enriched Uranium (HEU) contains more  $^{235}\text{U}$  which allows for a greater fraction of neutrons to cause fission allowing for a smaller volume/mass of uranium to reach criticality [41]. While this may produce a smaller reactor, the proliferation of HEU is a primary concern for the US government and other national governments making it a significantly more difficult for private companies to work with. “The use of LEU is consistent with US policy for civilian fission systems, reduces security-related costs and schedule impacts (compared to HEU), and greatly increases programmatic flexibility to allow extensive participation by industry and academia” [42]. There are greater security, transportation, and launch requirements with HEU reactors and material which increases program costs by millions of dollars [41].

Although HEU reactors may reduce launch costs because of lowered reactor mass, it is likely that a specialized and larger standby force would be needed for an HEU launch for recovery efforts to prevent HEU from falling into the wrong hands in case of an accident [41]. While the government may have the ability to launch HEU reactors at lower costs, commercial entities will most likely be restricted to only LEU as it will be much cheaper. By some estimates the cost reduction of commercial space companies developing a reactor would be 10% to 50% that of one developed by the government. The uranium within the SPEAR nano-reactor will be enriched to 19.75% to remain classified as LEU avoiding security and regulation issues. Producing only 15 kWt of power also reduces the size of the reactor as most NEP reactors are designed in the MWt power range which would increase launch costs and reactor complexity.

### 6.1.4 Advantages of LiH

When combined with an appropriate moderator and encased in a reflector, LEU is perfectly suitable for energy generation on scale suitable for a spacecraft the size of SPEAR with limited mass penalties. Moderators slow down neutrons emitted by the uranium, promoting additional fission. Reflector material helps keep more of the neutron material travelling through fissionable material. These two in combination allow a reactor built with LEU to reach criticality well below LEU's critical mass.

Lithium Hydride (LiH) was selected as the moderator due to its high hydrogen density. Hydrogen atoms are the most efficient particles for slowing down fast neutrons since both have the same mass [43]. Other materials, such as methane, offer similar performance but are not solid at the system operating temperatures, making them harder to implement and handle. Graphite, typically used as a moderator for its high operating temperature, lacks large amounts of hydrogen. Utilizing LiH increases the amount of hydrogen but reduces the operating temperature from 4000K [44] for graphite down to 961K [45] for LiH. This reduction in operating temperature is compensated for the large increases in efficiency seen with the ATEG conversion system. LiH also has the added benefit of reducing the mass of the core as it is less dense than graphite.

Heat pipes will be located directly inside of the uranium fuel as that is where the heat is generated and will have the highest temperatures. Removing the heat at the source will assist in reducing temperature peaking and limit the effects of the poor thermal conductivity of the moderator.

### 6.1.5 ATEG Location

The ATEGs are located at the base of the reactor assembly. The vertical orientation of the heat pipes allows for a single heat diffuser to accept input from all the heat pipes to the top of the ATEGs. The cold side of the ATEGs will connect to another heat diffuser plate with a working fluid that transfers heat to the radiators to dissipate the heat. This working fluid in conjunction with the radiators will maintain the cold side temperature of the ATEGs at 350K.

As discussed in the previous sections ATEGs utilizing  $(n,\alpha)$  interactions require a thermal neutron source to achieve their expected efficiencies. Therefore, the ATEGs have been placed as close as possible to the reactor to maximize their exposure to the neutrons coming from the reactor. Increasing the efficiencies of these ATEGs would require increasing the flux rate from the reactor as this would increase both the ionizations observed in the ATEGs as well as increase the temperature of the reactor. ATEGs with radioisotope sources would not necessarily require close

proximity to the reactor, but the reduction in heat pipe mass is an important factor in maintaining a lightweight spacecraft.

### 6.1.6 Neutron Flux from Reactor

Analyzing the neutron flux is important both for determining the efficiency of the ATEGs and for shielding design. The neutron and photon flux were determined using MCNP6. Measurements were taken at 25 cm and 350 cm from the center of the reactor. An F2 averaged surface flux tally measured the average neutron flux through a sphere with 25 cm radius, placing it just outside the reactor surface. This value is important as ATEG performance is directly dependent on the neutron flux when using a (n,α) ATEG. Another F2 averaged surface flux tally was taken using two circular surfaces whose area was equal to the planned shielding geometry. The neutron flux values and distance from the reactor are visible in Table 8. As discussed in the section detailing the ATEG system, investigations need to be conducted into the performance of materials that would form (n,α) ATEGs. These systems may require more or less neutron flux which may affect the design of the reactor. These fluxes can be easily simulated in a reactor with the ATEG material to determine how it effects the materials conductivity. From these studies adjustments can be made to optimize the reactor if the (n,α) ATEGs will be utilized.

**Table 8: Neutron Flux values for the reactor and shield. These fluxes were calculated without the xenon propellant tanks.**

Description	Outside Reactor	Front Face of the Shield (w/o propellant tanks)	Rear Face of the Shield (w/o propellant tanks)
Distance from Reactor (cm)	25	350	375
Averaged Neutron Flux ( $\frac{N}{cm^2.s}$ )	4.5097749E+14	3.6329239E+12	7.2323417E+08
Averaged Gamma Flux ( $\frac{P}{cm^2.s}$ )	3.3125579E+18	1.7131607E+16	5.1148057E+14

## 6.2 Shield Design

SPEAR's shadow shield has been designed to protect the vital areas of the spacecraft from the harmful radiation that the reactor produces. The shield takes the shape of a cross to match the orientation of the CubeSat bays. This conforms to how the CubeSats are currently orientated for deployment at Europa. The neutron shield itself is made from tetramethylammonium borohydride (TMAB C<sub>4</sub>H<sub>16</sub>NB). This relatively light weight material is extremely useful as a shielding material in nuclear

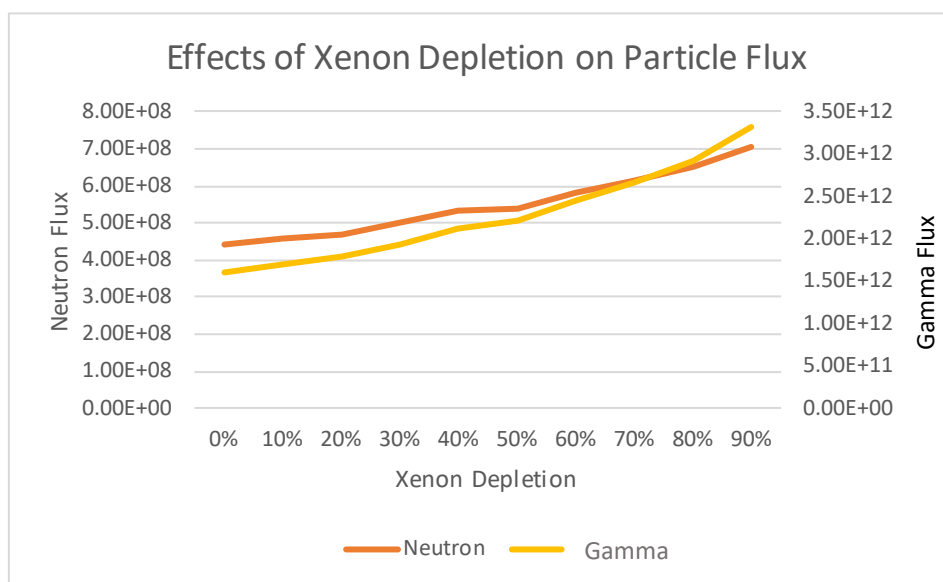


**Figure 26: Neutron and gamma flux effected by the amount of xenon depletion. This flux represents the amount of neutrons that have traveled through the propellant tanks to the front of the shield.**

system. The hydrogen density within TMAB allows it to thermalize neutrons and the boron, with a naturally large neutron capture cross section, absorbs neutrons coming from the reactor. From Table 8 above, it can be seen that the neutron flux is reduced by four orders of magnitude.

### 6.2.1 Propellant Tanks

Aiding in the protection of the CubeSats are the large tanks of xenon placed in front of the shield. These propellant tanks were strategically located to also aid in reducing the dosage the CubeSats see from the reactor. Each propellant tank contains compressed xenon, and with this added mass between the CubeSats and the reactor the total dose observed decreases. Throughout the mission however, the mass of propellant will decrease effecting the effective dose rate to the payload. A study was conducted to better understand how the neutron and gamma flux will change with varying masses of xenon to simulate a journey to Europa. These results are visible in Figure 26. There is some decrease in neutron flux and gamma flux observed. However, it is not of a large magnitude and only decreases the flux by a small factor. However, the addition of the propellant tanks does aid in decreasing the flux behind the shield by another order of magnitude, most likely due to slowing down the neutrons and photons passing through the propellant.

### 6.2.2 Shield Mass

The shields current mass is 32 kg and with this amount of shielding results in a dose of 0.0113 mGy/s directly behind the shield. There are many components between the shield and the CubeSats including power processing units, reaction control wheels, CubeSat Deployers, and shielding for the CubeSats at Europa. A study was conducted to determine the dose of a CubeSat positioned directly behind the shield as a worst-case scenario. The shield thickness was increased to determine how it would affect the dose of the CubeSats. This is represented as a total mass

increase of the shield. These results are shown in Figure 27. Increasing the thickness/mass of the shield allowed for a greater portion of neutrons and gamma rays to be blocked resulting in a slightly smaller dose. It should be noted that the CubeSats are arranged linearly which will result in the CubeSat closest to the reactor having the highest dose. Each subsequent CubeSat will absorb a smaller and smaller dose as the gammas and neutrons are stopped by the electronics, deployers, and individual radiation shields for the Europa environment.

There are several methods that can be used to limit the radiation dose the CubeSats will observe to even lower levels. The first being limiting the amount of time the reactor is operating. The nano-reactor may be able to be shut off during portions of SPEARs missions were the constant thrust is not required. However, this would result in complex restart procedures that are dependent on fission products and poison buildup. Increasing the shield thickness/mass will also aid in the reduction of dosage as was observed in Figure 27. Organizing the payload in another

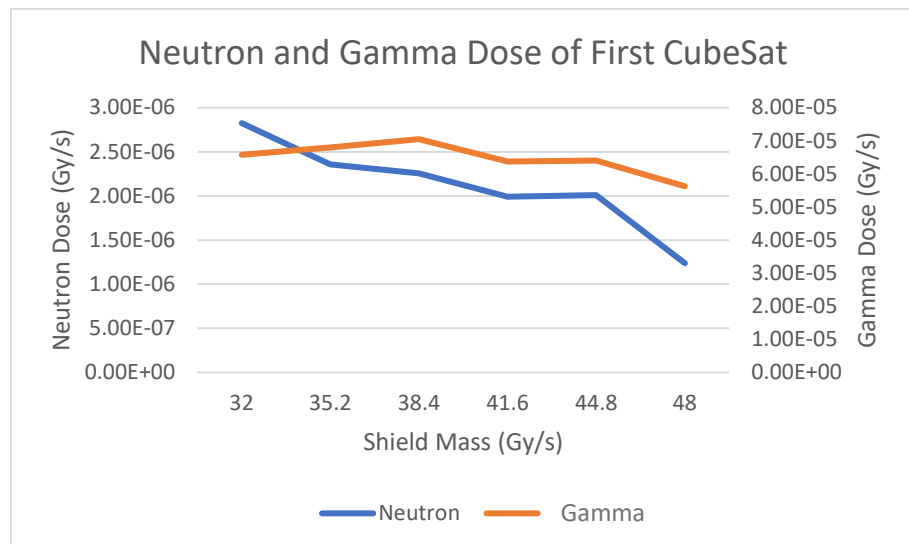


**Figure 27: Neutron and gamma dose rate for a CubeSat positioned directly behind the shield. In reality there would be space between the shield and CubeSats filled with reaction wheels, electronics, deployment mechanisms, and individual shielding for the CubeSats in the Europa environment.**



fashion may also achieve a greater reduction in dosage with the same mass. If all CubeSats can be placed in a linear fashion a larger majority of the shields mass can be placed in front of the CubeSats. Increasing the distance between the reactor and the shield is also an effective method to reduce the total dose absorbed. At ~3m from the reactor the total dose for all four CubeSats directly behind the shield was 0.276 mGy/s; when the distance was increased to 6 meters the total dose was decreased to 0.0889 mGy/s. This magnitude is consistent with the inverse square law that the reactor particle distribution follows. Increasing the distance from the reactor and changing the layout of the CubeSat payload could be an effective method of reducing the total dose. However, this would make for a very long spacecraft, which may not be able to fit in most launch vehicles without folding or deployable booms. The addition of these mechanisms would increase the failure probability of the spacecraft.

### 6.3 Planetary and Deep Space Radiation Environments

Jupiter has one of the most extreme radiation environments in our solar system due to its strong magnetic fields making exploration of Jupiter itself and its moons a serious technical challenge [46]. These radiation belts consist of trapped heavy ions, protons, and electrons which can damage spacecraft systems [46]. While these are the strongest radiation belts that SPEAR and its CubeSats will need to endure, SPEAR must contend with galactic cosmic rays (GCR), solar particle events (SPE), as well as the Van Allen radiation belts around Earth. The reactor discussed in another section also produces ionizing radiation that influences the spacecrafts design and can negatively affect electronics. The total dose due to environmental radiation effects and its potential effects on the spacecraft must be accounted for in addition to radiation generated by the reactor.

#### 6.3.1 Earth Radiation Environment

After launching into Earth's orbit, SPEAR will need to contend with Earth's radiation belts as it spirals out to Jupiter. These fields, like those found at Jupiter, contain trapped heavy ions, protons, and electrons that can all damage spacecraft systems. Minimizing the time spent in these fields is paramount for mission success. As will be noted in the trajectory section of this report, SPEAR is currently reported to spend a significant amount of time within Earth's orbit as it spirals out to an escape trajectory.

While this radiation field is not as large as the Jovian field, it can still significantly affect the payload and electronics. Reducing the time spent in these fields can be accomplished via a kick stage that shortens the time until SPEAR is able to escape Earth. An electric propulsion system with a higher thrust could also decrease the trip time within these fields but would likely reduce Isp. Additionally, the spacecraft can be deployed from the launch vehicle at a higher altitude

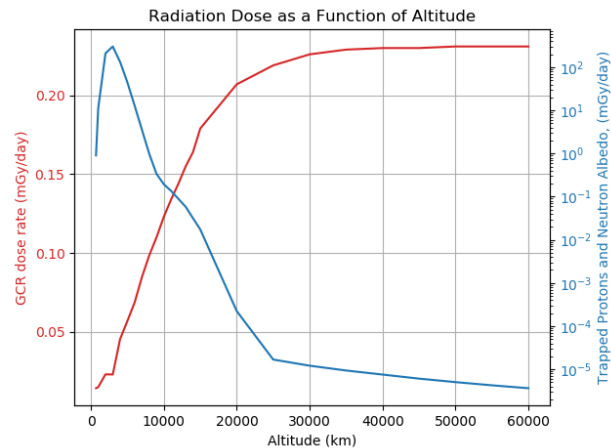


**Figure 28: Radiation dose due to GCR and Trapped protons and neutron albedo in Earth's orbit. Reducing the amount of time spent within these fields will reduce the total dose to the system.**

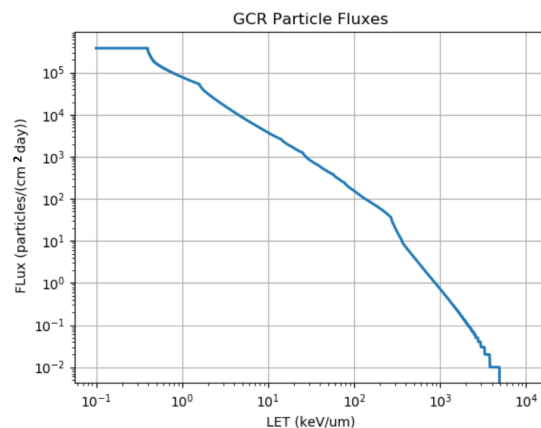


**Figure 29: Expected GCR fluxes for various linear energy transfer values. Particles with lower LET values are typically more common while it becomes increasingly more uncommon for high LET particles to strike the SPEAR spacecraft.**

to reduce the total time in orbit. SPEAR is expected to be within the Van Allen Belt range for ~3.5 years based on its current trajectory and will be subjected to various levels of radiation while it travels through this area. Figure 28 shows how the radiation doses change as a function of altitude. The On-Line Tool for the Assessment of Radiation in Space (OLTARIS) was used for these calculations. At lower altitudes the trapped proton and neutron albedo has a much greater effect on the TID than the GCR. As altitude increases the dominant source of radiation transitions from trapped protons and neutron albedo effects to GCR.

### 6.3.2 Interplanetary Radiation Environment

On its journey to Europa, the spacecraft will be in interplanetary space for a relatively long period of time. This will primarily expose it to GCR and SPE. Spacecraft charging can occur, but of more importance is issues caused by GCR interactions with SPEARs computer causing malfunctions known as single-event phenomena (SEP). SEP can be broken down into three other groups, single-event upset (SEU), single-event latch-up (SEL), and single-event burnout (SEB) [47]. An SEU, also known as a bitflip, causes errors in data that do not necessarily affect the spacecrafts performance. This can however, effect data relating to the spacecraft's health and position as well as scientific data. SEL events occur when a part hangs up, draws excessive current, and no longer operates until it is power cycled [47]. This current draw can both damage the component and drain power to other spacecraft systems. If essential systems are destroyed because of this the SPEAR probe could be permanently crippled. SEB events cause irreversible damage to a component that cannot be repaired. The expected absorbed dose of a SPE was found using the OLTARIS tool and the expected flux of GCR particles can be found in Figure 29 The linear energy transfer (LET) is the energy deposited by an ionizing particle into a material per unit pathlength [48]. Lower energy GCR have higher fluxes than GCR with high LET values.

While a shadow shield can protect the payload from the neutrons coming from the reactor, it cannot protect the payload from GCRs coming from other directions. The GCR dose rate is expected to be 109.1 mGy/year with a total dose of 1507 mGy over the course of the interplanetary trajectory. These high energy particles are difficult to stop, but do not impart a significant radiation dose to the spacecraft compared to other environments. Figure 30 shows the expected absorbed dose during the interplanetary mission phase due to GCR.

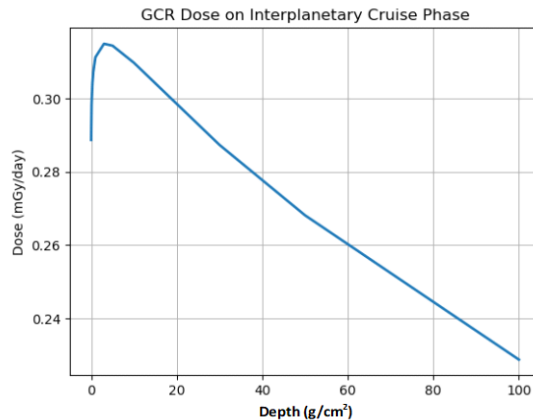


**Figure 30: GCR dose rate for an interplanetary trajectory to Europa as a function of aluminum shielding thickness. GCR particles are highly penetrating and significantly affect the health of the spacecraft.**

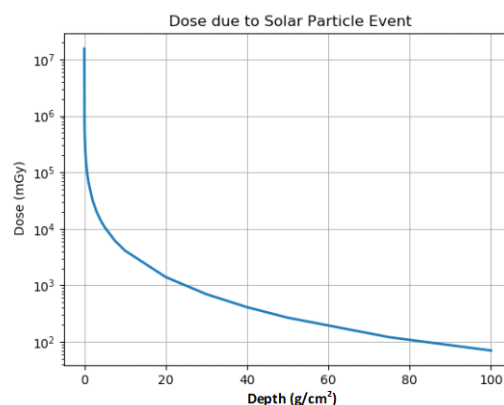


**Figure 31: Solar Particle Event and its associated absorbed dose in aluminum. SPE events are difficult to predict and can significantly damage the spacecraft. This SPE event is based on the 1859 Carrington Event and modeled with OLTARIS.**

Another source of ionizing radiation that SPEAR must contend with are solar particle events (SPE). These events can happen unexpectedly and can be devastating to spacecraft. An expected dose for an SPE event was found based on the historical data from the 1859 Carrington Event which was one of the largest SPE in recent history [49]. One such event could subject the SPEAR spacecraft to extreme levels of radiation. This is evident from Figure 31, which shows the effects of a historical SPE event calculated with OLTARIS.

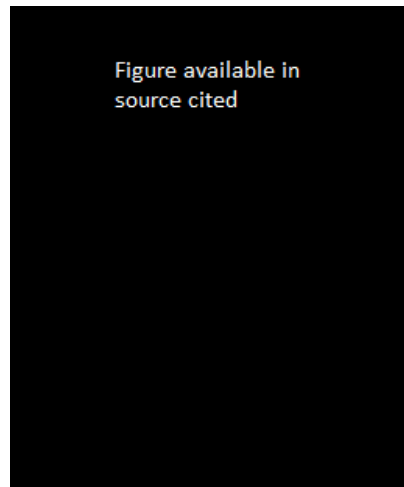
### 6.3.3 Europa Radiation Environment

In this environment, SPEAR will see the largest doses of radiation. As stated earlier the trapped heavy ions, protons, and electrons in this environment contribute to an almost 30 krad/day dose behind 100 mils (2.54mm) of aluminum [20]. Figure 32 shows the expected radiation dose of the Europa environment for the proposed Europa Clipper mission. While most Jovian missions avoid most of the radiation environment by dipping in and out of the radiation fields, SPEAR will need to be within the radiation fields for an extended period of time to deploy CubeSats, as well as power them during their expected 30-day mission. It is clear from figure 1 that Europa sits inside an intense radiation field with a minimal amount of shielding. Increasing the thickness of this shield is one method to reduce the total ionizing dose. However, increasing the thickness of the material will also increase the mass of the spacecraft. This issue becomes especially prevalent with the CubeSats which are extremely mass limited. One such spacecraft that is currently operating in the Jovian system is Juno which included a nearly 200 kg radiation vault to protect its electronics [50]. SPEAR and its CubeSats will be in orbit around

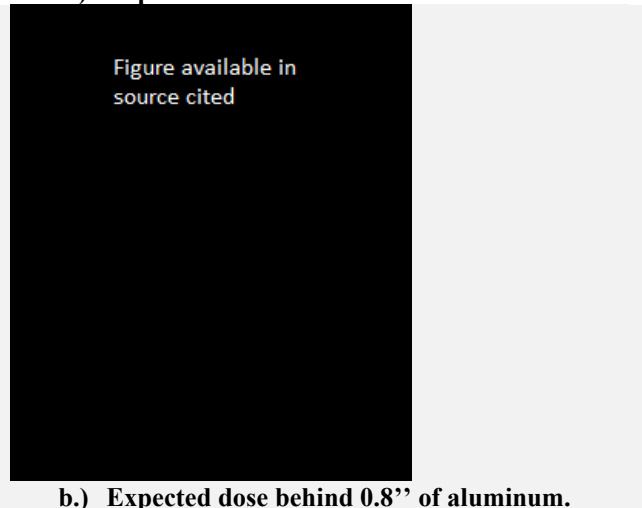
Europa to maximize the possibilities of capturing plume particles. Given that the CubeSats are very small and require open ports to physically capture particles, instruments and electronics will rely on radiation hardened components in lieu of a radiation vault. However, while in orbit SPEAR has the potential to utilize its shadow shield for additional shielding of the on-board electronics by orienting itself to face the radiation field. This could assist in keeping the main craft operating for longer periods of time if necessary.

## 7 THRUSTER SELECTION

SPEAR will require a very robust thruster capable of operating for an extended period of time and at high power levels. Atomos Space led the investigation into the thruster selection, investigating several different thruster and propellant combinations, with an initial trade study to investigate mission flexibility.



a.) Expected dose behind 0.01'' of aluminum.



b.) Expected dose behind 0.8'' of aluminum.

**Figure 32: The expected TID at Europa and the Jovian system is quite large. Reducing the TID can be accomplished by changing the shield material or increasing its thickness. Figures courtesy of [20].**

## 7.1 Specific Impulse Selection

Holistically-focused power and propulsion technology selection is one of the most critical steps in developing a spacecraft architecture. For the SPEAR mission concept, the thruster characteristics, power system characteristics, and trajectory must be holistically optimized.

A thruster optimization was performed, considering key parameters of transit time and launch mass. For the baseline optimization, a vehicle specific mass of 2.6kg/kW<sub>e</sub> was selected for the initial study. The mission segment involving interplanetary transit was considered (that is, Earth-escape to Jupiter capture), with a DV of 17km/s (not including losses). Results are shown in Figure 33 below.

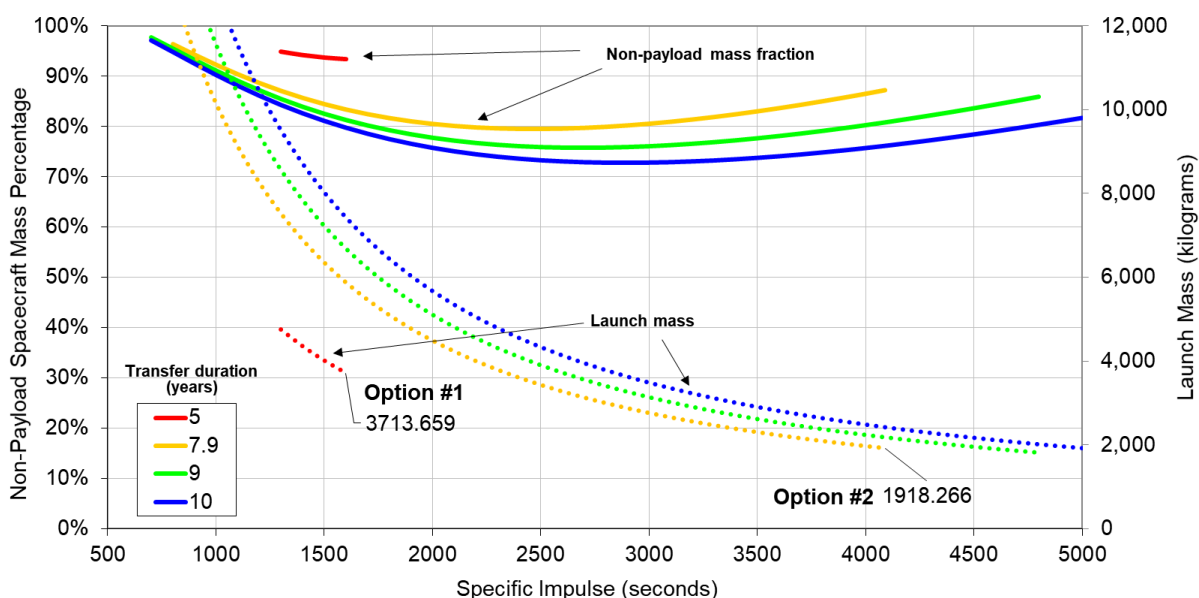


**Figure 33: Power System and propellant mass fractions, and spacecraft launch mass as a function of specific impulse for various interplanetary transit durations.**

Transit durations of 5 to 10 years were considered for this segment. As predicted, payload masses could be maximized over the specific impulse range considered, shown by the local minimum in non-payload specific mass fractions. Two options were considered; fast transit (Option #1, 1,600s, 5 years), and low launch mass (Option #2, 4,090s, 7.9 years). A sensitivity study was performed, to examine the effect of variations to the assumed vehicle dry mass. Outcomes are provided in the Table 9 for the initial trade study.

**Table 9: Thruster sensitivity study outcomes**

Case	Value	Option 1 1,600s	Option 2 4,090s
Baseline	Alpha (W/kg)	2.9	2.9
	Payload mass (kg)	111.9	111.9
	Transfer duration (years)	5.0	7.9
	Propellant mass (kg)	2590.7	795.3
	<b>Launch mass (kg)</b>	<b>3713.7</b>	<b>1918.3</b>
Mass Growth	Alpha (W/kg)	2.0	2.0
	Payload mass (kg)	111.9	111.9
	Transfer duration (years)	7.0	11.0
	Propellant mass (kg)	3587.2	1059.1
	<b>Launch mass (kg)</b>	<b>5199.1</b>	<b>2671.0</b>
Mass Improvement	Alpha (W/kg)	4.0	4.0



	Payload mass (kg)	111.9	111.9
	Transfer duration (years)	4.0	6.3
	Propellant mass (kg)	2109.0	667.8
	<b>Launch mass (kg)</b>	<b>2970.9</b>	<b>1529.8</b>
DV Growth (+25% additional DV)	Alpha (W/kg)	2.9	2.9
	Payload mass (kg)	111.9	111.9
	Transfer duration (years)	7.4	10.5
	Propellant mass (kg)	3778.2	758.7
	<b>Launch mass (kg)</b>	<b>4212.5</b>	<b>2141.6</b>

It was determined that the mission could still be completed with either the 1,600s or 4,090s thruster, even with mission DV or vehicle mass growth. However, Option #1, 1,600s, showed strong deviations and sensitivity to mass growth, with a higher rate of propellant growth. Option #1 was therefore seen as higher risk for launch mass growth, indicating that mass budgets could be violated later in vehicle and mission design.

- Option #2 was found to have strong deviations in mission duration with increasing DV or vehicle mass, however displayed less mass growth.
- Option #2 was selected for further consideration due to the significant launch mass improvement over Option #1.
- However, the trade between Option #1 and Option #2 is fundamentally a trade between launch mass and mission duration. With the objective of enabling affordable deep space missions, launch and operating costs allow direct comparison and trade between these two factors.

## 7.2 Thruster Selection

Propellant selection is another important factor in propulsion system optimization. A summary of considered propellants is detailed below in Table 10.

**Table 10: Propellant options and comparison between two mission options for SPEAR.**

			Option 1 1,600s		Option 2 4,090s		
Propellant	Storage Density (kg/m <sup>3</sup> )	Cost (\$/kg)	TRL*	Propellant cost	TRL*	Propellant cost	Existing Candidate
Xenon	1,351	\$850.00		\$2,202,120		\$676,036	Next-C [51]
Argon	250	\$5.00		\$12,954		\$3,977	BHT-600 [52]
Krypton	788	\$330.00		\$854,941		\$262,461	BHT-600 [52]
Iodine	4,940	\$20.00		\$51,815		\$15,907	BHT-600-I [52]
Ammonia	241	\$0.52		\$1,347		\$414	IRS AF-MPD, SX3 [53]
Lithium	534	\$95.00		\$246,119		\$75,557	LiFA (AF-MPD) [54]
Bismuth	9,780	\$390.00		\$1,010,384		\$310,181	NA
Mercury	13,593	\$17.40		\$45,079		\$13,839	Apollo ACE (1250s) [55]

\*Red TRL 0-5; yellow TRL 6-7; green TRL 9



It was found that the cost of Xenon was very high in comparison to other propellants. However, all other alternatives either had a low storage density (such as Ammonia) or a low technology readiness level (TRL) such as Mercury. Given the high TRL of Xenon systems – including propellant feed systems and engines, Xenon was selected for the propellant.

## 8 SPEAR MISSION PERFORMANCE

After initial trade studies, SPEAR's trajectory and mission design was further developed. Thruster specifications were modeled after SPEAR's expected 3kW<sub>e</sub> output. This mission was also compared to NASA's Kilopower system to determine the advantages of a solid state power conversion system.

### 8.1 SPEAR Trajectory Design

A study was performed to determine a high-fidelity trajectory for the mission given the spacecraft characteristics and thruster performance capabilities. Important factors to address include transit time, propellant mass, and any relevant launch windows. The objective of the trajectory design for this study was to highlight the advantages of the SPEAR power generation and conversion architecture over existing concepts. As such, several simplifying assumptions were made, which are detailed below.

The SPEAR spacecraft powers its main thruster at approximately 3kW<sub>e</sub>. Next-C is a throttleable engine, and its thrust and specific impulse at 3kW<sub>e</sub> was determined using a thruster model constructed from curve fits based on data from [51]. Curve fits are shown in Table 11, below.

**Table 11: NEXT-C Engine Model**

	Formula	Output at 3kW <sub>e</sub>
Specific impulse (s)	$269.32 + 2.4215P - 0.00056905P^2 + 4.2409 \times 10^{-8}P^3$	3,630.49
Mass flow rate (kg/s)	$\text{Throttle} \times (3 \times 10^{-6} - 2 \times 10^{-9}P + 1 \times 10^{-12}P^2 - 9.8 \times 10^{-17}P^3)$	$3.354 \times 10^{-6}$
Mass flow efficiency (%)	0.93	0.93

This model provided a thrust of 111mN and an I<sub>sp</sub> of 3,630s at 3kW<sub>e</sub>. Note that the I<sub>sp</sub> is significantly lower than the 4,090s selected in the thruster design trade, however it was determined that a high-TRL, near-term system should be used to reduce costs. It was assumed that the thruster could be fired for an arbitrarily long time and could therefore be treated as a long-duration, low-thrust propulsion system.

The SPEAR trajectory was modeled starting in low Earth orbit at an altitude of 700km and continuing through Earth escape until arrival within Jupiter's sphere of influence, not including Jupiter orbit capture. An overview of the trajectory is shown in Figure 34.

For the sake of comparison, a lunar flyby was avoided. Future detailed trajectory planning should incorporate use of lunar gravity to aid in Earth escape while simultaneously reducing fuel requirements. This is of particular importance given the low thrust level available from electric propulsion. However, this type of gravity-assist trajectory is extremely sensitive to encounter conditions and was therefore beyond the scope of the effort described here.



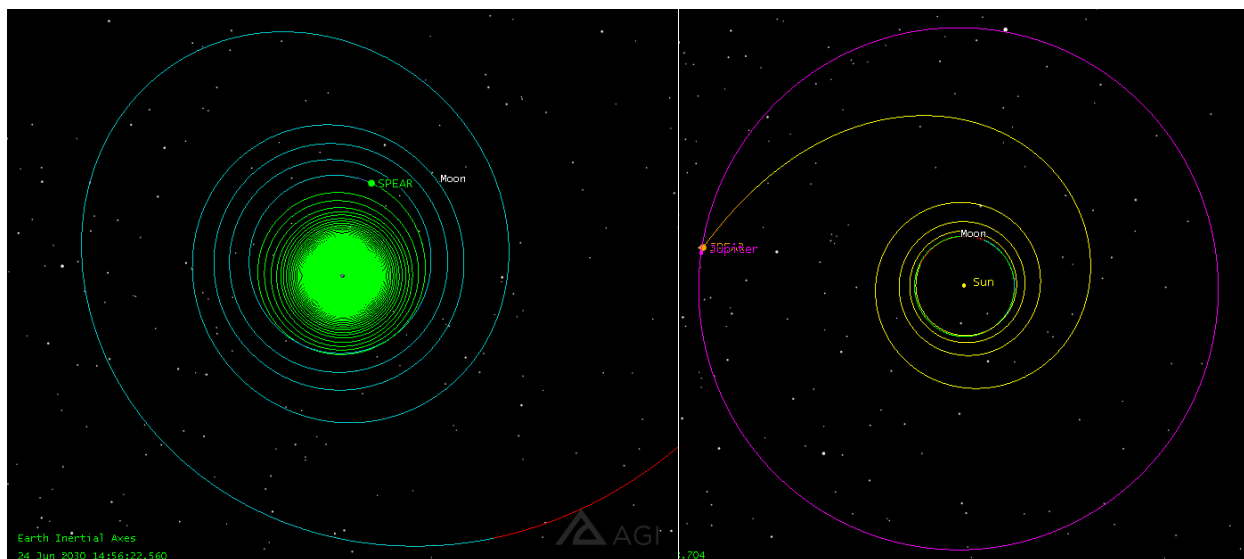


**Figure 34: SPEAR trajectory overview. Earth Escape (left) and Earth-escape to Jupiter (right) are shown.**

With a bus dry mass of 1,133.5 kg and an initial propellant load of 1,500kg, a departure date of 5 March 2026 was chosen for favorable planetary alignment. Under this scenario, Earth escape is achieved on 21 February 2031, after 1,814 days, or nearly 5 years. SPEAR then arrives at Jupiter almost 9 years (3,228 days) later on 24 December 2039. The total transit time is 5,042 days, or nearly 14 years. A summary is provided in Table 12, below.

**Table 12: SPEAR Mission Summary**

Segment	Delta – V (km/s)	Duration (days)	Propellant (kg)
Earth escape	7.371	1,814	525.6
Earth-escape to Jupiter	18.064	3,228	886.4
Jupiter capture to Europa orbit	NA*	NA*	80
Total	<b>25.435</b>	<b>5,042</b>	<b>1,500</b>

\*Not calculated as part of comparative study. Propellant allocation of 80kg assumed for final mission stages.

The total mission duration exceeds 10 years; however, a large fraction of the mission duration is low-thrust Earth escape. Transit duration for the interplanetary portion of the mission is as predicted in the low-fidelity thruster optimization study. Therefore, approaches to reduce this long transit time include: starting from a higher altitude (either from launching to a higher orbit or using a chemical kick stage to achieve Earth escape more quickly); utilizing lunar gravity to boost the orbit; selecting a thruster with greater thrust capability; or increasing power available to the thruster (provided this does not increase the spacecraft mass enough to offset the gain).

## 8.2 Kilopower Trajectory Design

In order to demonstrate the advantages offered by this technology, a comparison trajectory was modeled. Instead of the SPEAR reactor, shield, and ATEG conversion system, the spacecraft dry mass was recalculated to substitute a 3kW<sub>e</sub> Kilopower reactor, with its required shield, and a Stirling conversion system. This increased the spacecraft dry mass per Table 13 below. The masses for the Highly-Enriched Uranium (HEU) Kilopower reactor, shield, and Stirling engine system were taken from [56]. This reference provided a reasonable comparison to the SPEAR vehicle design point, with the Kilopower reactor producing 13.0kW<sub>T</sub>, the conversion operating at 23% efficiency, and the shield

designed to limit payload dosage at 10m to  $10^{11}\text{n/cm}^2$  and 25krad (although the duration of exposure period was unspecified). Figure 35 details the trajectory with the Kilopower reactor.

**Table 13: Kilopower dry mass comparison**

	<b>SPEAR</b>	<b>Kilopower - Stirling</b>
Reactor mass (kg)	134.0	175.0
Shield mass (kg)	32.0	364.0
Conversion system mass (kg)	11.0	449.0

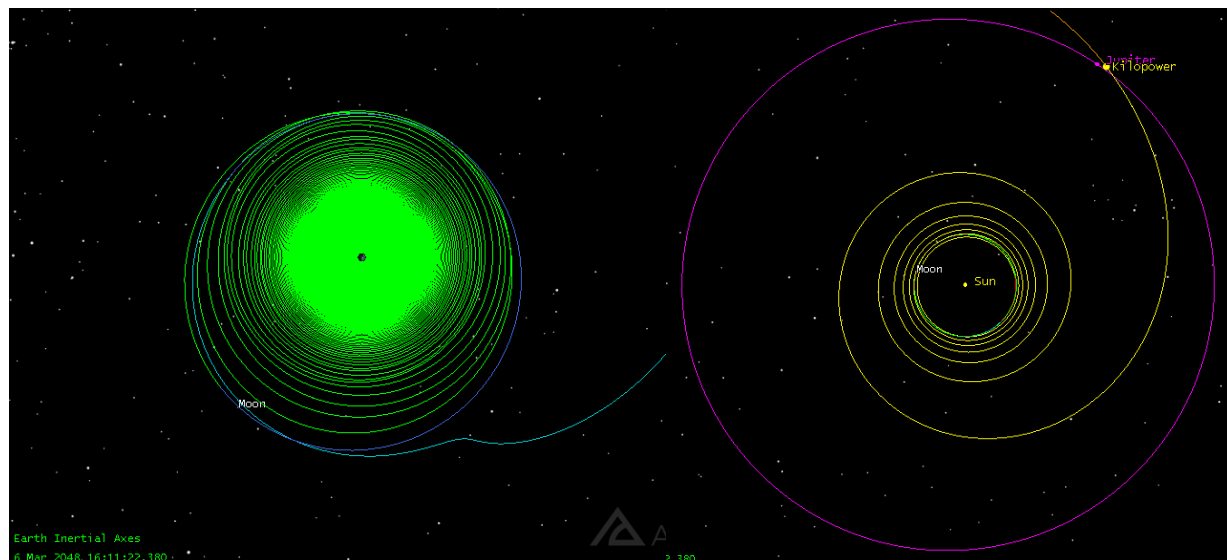


**Figure 35: Kilopower trajectory overview. Earth-escape (left) and Earth-escape to Jupiter (right) are shown.**

The propellant load required for the mission increased to 2,400kg. While an attempt was made to avoid a lunar flyby in order to compare this trajectory to the SPEAR trajectory described in the previous section, the increased departure mass combined with the low thrust from the propulsion system meant that it was not possible to completely avoid a lunar flyby, so one was selected that had only a small impact on the overall trajectory, reducing the DV required by 0.84km/s. The DV requirement and total transit time could be reduced further by selecting a lunar flyby with a different geometry, or by using any of the techniques mentioned in the previous section.

For this planetary geometry, a departure date of 2 April 2026 was chosen, again starting in low Earth orbit at an altitude of 700km. In this scenario, Earth escape is achieved on 5 October 2033, 2,743 days (approximately 7.5 years) later. The spacecraft arrives at Jupiter about 14.5 years (5,266 days) later on 6 March 2048. The total transit time is 8,009 days, approximately 22 years.

### 8.3 Comparison

The SPEAR vehicle is significantly lighter than the Kilopower vehicle. In comparison to SPEAR, the dry mass of the vehicle increased by 78% using the Kilopower power system, resulting in a slight mission interplanetary phase DV increase due to additional losses. The total propellant increased by 60%, from 1,500kg to 2,400kg. Due to the increased mass of the vehicle and propellant, this transit time is 59% longer than that of SPEAR. A summary is shown in Table 14.

**Table 14: SPEAR performance improvement over Kilopower system.**

	<b>SPEAR</b>	<b>Kilopower</b>
<b>Departure Date</b>	5 March 2026	2 April 2026
<b>Earth Escape</b>	21 February 2031	5 October 2033
<b>Duration</b>	1814 days, ~5 yrs	2743 days, ~7.5 yrs
<b>Delta-V</b>	7.371 km/s	6.535 km/s*
<b>Jupiter Arrival</b>	24 December 2039	6 March 2048
<b>Duration</b>	3228 days, ~8.8 yrs	5266 days, ~14.5 yrs
<b>Delta-V</b>	18.064 km/s	18.104 km/s
<b>Total Transit Time</b>	<b>5042 days, ~14 yrs</b>	<b>8009 days, ~22 yrs</b>

\*Delta-V appears low due to lunar gravity assist

#### 8.4 Mission and Systems Engineering Recommendations

SPEAR allows low-cost, high-performance deep space missions. Overall mission costs can be further improved through thoughtful technology selection, and wholistic mission optimization. As outlined Section 7, propellant selection factors into mission cost, with the highest-TRL propellant, Xenon, also being the most costly. The development of new electric propulsion systems that utilize more cost-effective propellants should be seen as an opportunity for cost reduction.

Reduction in mission duration can also lead to a reduction in operating costs, per Section 7. High-fidelity operating cost estimations should be generated prior to proceeding with the baseline mission outlined herein. A configuration with a higher launch mass but faster transit time may yield a lower net mission cost. Mission duration may also be improved by starting at a higher initial orbit. The Earth-escape mission segment is years in duration, due to the poor thrust-to-mass ratio of the NEXT-C thruster in the SPEARR spacecraft with initial propellant loading conditions. Launching the SPEAR spacecraft to a higher orbit or using a chemical “kick-stage” to achieve Earth escape more quickly is recommended. NASA’s planned Lunar Gateway could be used as a staging ground for such purposes.

Any opportunity to reduce spacecraft mass also results in cost savings. Lower dry mass results in both lower propellant consumption and shorter mission duration, and therefore any mass savings compound in a positive manner. Launch and operating cost savings must be carefully traded against development and unit costs, which tend to increase with the selection of more advanced, lightweight technologies. There are however simple system optimization levers that can be used to lower the mass without an increase to the development or unit cost. These are summarized in Table 15.

**Table 15: Strategies to optimize SPEAR vehicle mass without significant cost increase.**

Subsystem	Component	Method to minimize mass
Power	Conversion	<ul style="list-style-type: none"> <li>Material selection for heat exchangers</li> </ul>
	Radiator	<ul style="list-style-type: none"> <li>Increase temperature (decreases area by the fourth power of the rejection temperature)</li> </ul>
	Reactor	<ul style="list-style-type: none"> <li>Decrease volume (containment mass)</li> <li>Increase power</li> </ul>
	EPS	<ul style="list-style-type: none"> <li>Decrease distance to thrusters</li> <li>Direct drive</li> <li>High voltage transmission</li> </ul>

	Reactor Shield	<ul style="list-style-type: none"> <li>• Increase power</li> <li>• Increase payload separation distance</li> <li>• Increase payload radiation tolerance</li> <li>• Use localized shielding for sensitive avionics, payload components</li> <li>• Decrease operational duration</li> <li>• Decrease reactor cross-section</li> <li>• Select a thermal spectrum reactor</li> </ul>
Propulsion	Propellant storage	<ul style="list-style-type: none"> <li>• Storage pressure optimization</li> <li>• Propellant budget management</li> </ul>
Structure	-	<ul style="list-style-type: none"> <li>• Use truss structures</li> <li>• Increase truss diameter</li> <li>• Carbon-carbon structures</li> <li>• Decrease stiffness requirements (pointing)</li> </ul>

## 9 THERMAL SYSTEMS DESIGN AND PERFORMANCE ANALYSIS

As part of project SPEAR, The Hypershield Partnership, LLC (THP) conducted thermal analysis on the vehicle to provide radiators with sufficient performance to handle the expected waste heat of 12 kW<sub>th</sub> while aiming to have all radiators fit a mass budget of 200 kg. Additionally, the chosen radiator designs, on the full vehicle, were simulated through the expected thermal cycling as dictated by the vehicle's trajectory from Earth to Jupiter. As an additional constraint to the thermal system design, HI has planned to stay away from active cooling systems which would require pumps and additional controls systems. This greatly reduces the potential failure points for a system as critical as a NEP's radiators. For this reason, only passive heat pipes and solid material conduction were considered as means of transporting the heat from the reactor bay, out over the radiators surface area.

To start, a preliminary design study was performed using engineering first principles in order to guide the follow-on transient thermal modeling activities. The transient studies were then split between single radiator investigations and the full vehicle simulation incorporating the simulated trajectory from Earth to Jupiter.

### 9.1 Preliminary Design Study

Surface area required as a function of fins and surface properties was first considered. To provide an analytical relation for the radiators' performance, steady-state and isothermal assumptions were invoked. Additionally, a simple view factor,  $F_{self}$ , for self-radiation was considered as a function of  $n_{fins}$ , number of radiators (or "fins") arranged about the central pylon. Considering a combined value for solar and planetary heat sources, the required area of the isothermal radiator to get rid of the heat load,  $Q_{th,w} = 12 \text{ kW}_{th}$ , can be written,

$$A = \frac{Q_{th,w}}{n_{fins} \{ 2 \epsilon_T \sigma (T^4 - T_\infty^4) (1 - F_{self}) \} - \sum n_{facing} \alpha_{obj} I_{obj}} \quad (12)$$

where,

$$F_{self} = 1 - \sin\left(\frac{\pi}{n_{fins}}\right) \quad (13)$$

Equation 13 is the 2D version of the view factor for plates arranged like the radiators. This was used in the initial estimate to follow the theme of conservatism. That is to say, this value is larger than the associated 3D version of  $F_{self}$ . For example, at 90° separation, the two panels in 3D are,  $F_{self,3D} = 0.20004$  while  $F_{self,2D} = 0.2930$ . The solar constant,  $I_{sol} = 1.367 \text{ kW/m}^2$ , is the magnitude of the solar irradiation at the distance the Earth is from the Sun [57]. The design



variables included in Eq. 12, for a specified load of  $Q_{th,ws}$ , are the  $n_{fins}$ , the equilibrium temperature,  $T$ , and the surface optical properties of absorptivity,  $\alpha$ , an emissivity,  $\epsilon$ . As will be discussed more in the following section, the surface property values can differ between the solar spectrum and strictly infrared sources. For this initial analysis, a large range of surface properties were considered.

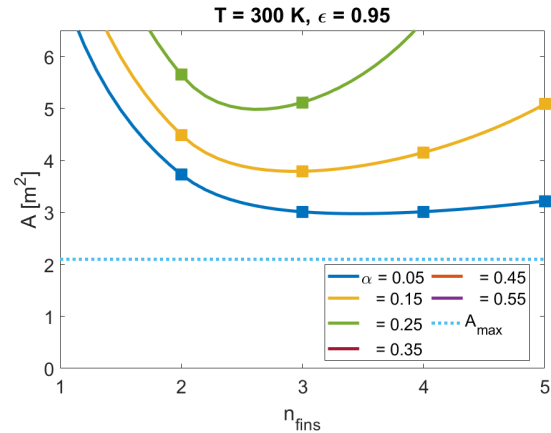
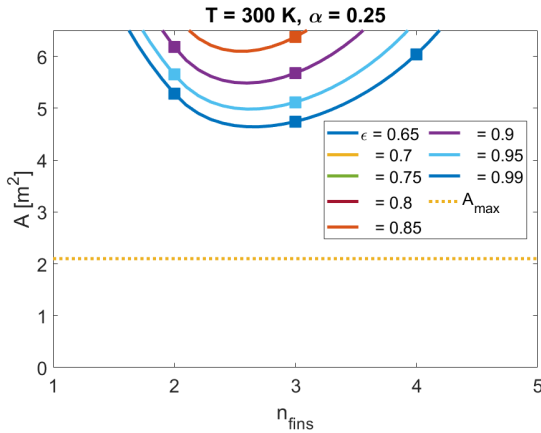
The condenser end of the main heat pipes, residing within the reactor bay, is intended to maintain an operating temperature of 650 K while transferring waste heat out of the reactor. The cold side of the conversion system takes waste heat to the radiators at 350 K. Temperatures must be maintained within the design ranges in order to provide the expected performance of the electrical energy production. The condenser can be colder than 350 K as long as the significant solidification of the heat pipe working fluid is not able to occur in such a way which hampers the ability of the liquid to flow through the wick of the heat pipe, back to the evaporator. The colder temperature would increase conversion performance but decrease radiator performance. If the condenser is too hot, then the working fluid will not liquefy. The liquefaction releases the latent heat needed to improve the heat transfer above natural convection. Thus, it is critical to ensure the radiators can conduct and radiate away sufficient energy to guarantee the heat pipe condensers are maintained at or below 350 K.

With infinite conductivity, the radiator would be isothermal at about 350 K. Figure 36(a-f) show the design space for such a system. Since there will likely be a temperature gradient across the radiators, the steady-state average temperature will be lower than the desired 350 K at the primary heat pipes. Ideally, the radiators are conductive enough to minimize this gradient. Considering these arguments, an average temperature of 300 K was also considered for the high-level sizing study. To round out the picture of the design space, the case of  $T = 400$  K was also included. For each of these cases, one surface property was held constant (along with the temperature) and the magnitude of total heat input scaled with number of fins through both the waste heat input from the reactor as well as the self-radiation between fins, per Eq. 13.

As the plots show, surface properties must be altered (i.e. surface coatings) to seek low absorptivity,  $\alpha$ , and high emissivity,  $\epsilon$ . Certain surface coatings are available which can obtain this characteristic using the differences in absorption/emission spectra described below. Note that the value of  $A_{max} = 2.1 \text{ m}^2$  is based on the outline of the radiators, as shown in Figure 5. This design is based on fitting into a Minotaur V launch vehicle's payload fairing. Larger areas would be possible if a deployable mechanism was included in the radiator design. Any additional mechanisms on a spacecraft will however increase the risk of subsystem failure. Fortunately, the results of the preliminary design study suggest that a design within the  $2.1 \text{ m}^2$  envelope is feasible and the added risk associated to deployable radiators was not needed.

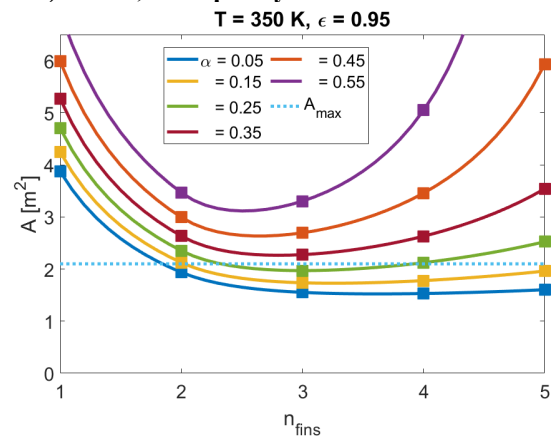
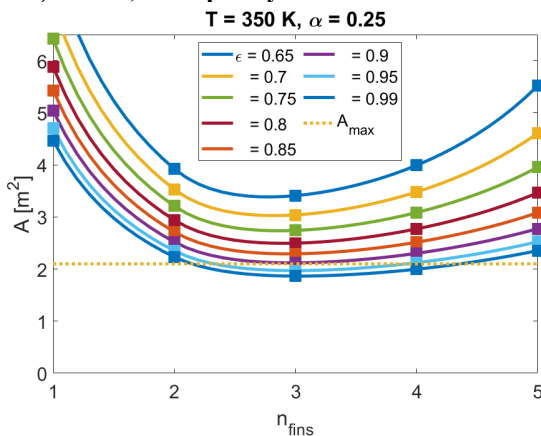
Both  $\epsilon_T$  and  $\alpha_{obj}$  are important and complex parameters which delve into the realm of selective emitters and non-Planckian radiation. For any given wavelength of light, the absorptivity and emissivity are equal. However, at different wavelengths of light, emissivity/absorptivity can vary in value. For radiators, this is important because the sun emits much of its light in the visible/UV spectrum, whereas thermal radiation is often in the infrared range. Thus, a radiator with low emissivity/absorptivity in the visible/UV range but high emissivity/absorptivity in the IR range would be able to reflect much of the sun's incident radiation while also rejecting heat in the IR spectrum. This is very dependent on the surface of the material, as well as the operating temperatures and the temperatures of the celestial bodies radiating on to the surface.

Over the span of all wavelengths, the selective emitters will have a total emissivity/absorptivity value for each temperature. Maximizing the ratio of emissivity at the radiator temperature to absorptivity at the source temperature is one way to optimize the radiator size. The figures below show how the number of fins and absorptivity of solar irradiance effects the required size of the radiators. The thermal effort found that the necessary radiators are realistic and achievable for the mission and mass budget allotted.



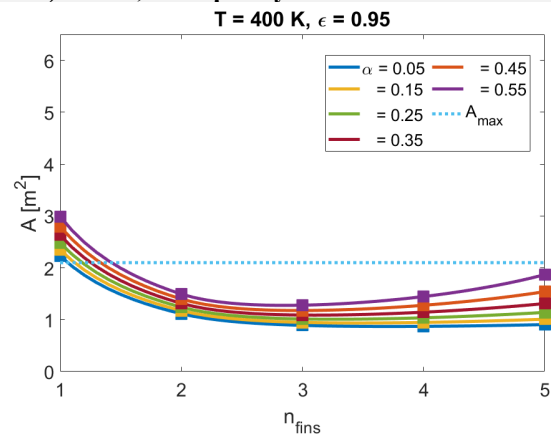
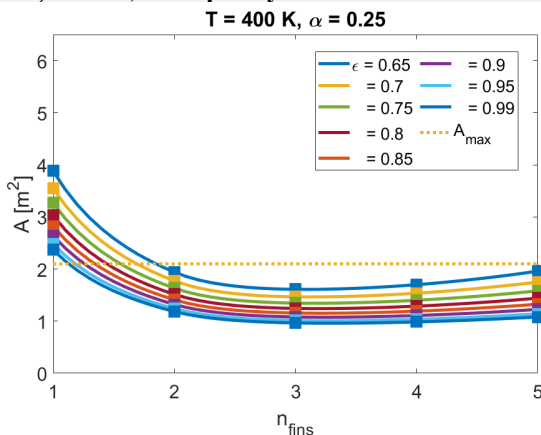
a.) 300K, absorptivity=0.25

b.) 300K, absorptivity=0.95



c.) 350K, absorptivity=0.25

d.) 350K, absorptivity=0.95



e.) 400K, absorptivity=0.25

f.) 400K, absorptivity=0.95

Figure 36 (a-f): Required surface area for radiator under various design considerations.

This provided the ballpark of radiator acreage needed to manage the expected energy balances. As already mentioned, these results represent ideal conditions for very high transport through the material. It is however clear that lower  $\alpha$ , larger  $\epsilon$ , and higher wall temperature lead to smaller required areas for radiating the waste heat. To put these performance characteristics in terms of materials, various properties and estimated cost of different materials was considered (Table 16).



**Table 16: Materials of interest for radiators. Data from [58]**

Material	$\rho$ [kg/m <sup>3</sup> ]	C [J/(kgK)]	k [W/(mK)]	T <sub>melt</sub> [K]	Cost [\$ /kg]
Copper (Cu)	8860	378	1-391 (alloy range)	1357	2.25
Aluminum (Al)	2770	961	117-218 (alloy range)	933	1.80
Beryllium (Be)	1850	1825	70-1000 = f(1/T)	1550	315
Graphite, pyrolytic (PG)	2210	100-2000 = f(T)	= 250-5000 = f(1/T) ⊥ = 0.8-17 = f(1/T)	2273	10
Graphite, fiber (25% epoxy by vol.)	1400	300-1300 = f(T)	= 5-13 = f(T) ⊥ = 0.4-1.1 = f(T)	450	110

To get an idea of the magnitudes of radiator masses for different material options, Table 17 shows mass of solid panels of various materials and thickness for different surface areas. This is to compare to the areas estimated in Figure 36.

**Table 17: Reference masses of different sized squareslabs for materials of interest. Materials in blue are masses in kilograms.**

Material		<i>Cu</i>			<i>Al</i>			<i>PG</i>			<i>Be</i>		
Total Surface Area [m <sup>2</sup> ]		4	5	6	4	5	6	4	5	6	4	5	6
Thickness [mm]	1	18	22	27	6	7	8	4	6	7	4	5	6
	10	177	222	266	55	69	83	44	55	66	37	46	56
	30	532	665	797	166	208	249	133	166	199	111	139	167

## 9.2 Radiator Performance Study

In order to better understand the radiators performance under realistic, non-isothermal, conditions with all competing transfer mechanisms, the energy equation in the solid material must be solved. Leveraging decades of modeling experience, THP has developed in-house software capabilities to meet such engineering simulation needs. The THP Multi-Physics Engine (MPE) can be used to simulate the transient relaxation of any system of equations which are governed by environmental, internal or state-dependent physical phenomena.

In order to understand the transient effects induced from the different material and design options, high-resolution numerical models of single radiators were developed. These models solved the energy equation in finite volume elements (Figure 37) which are generated from an outer-mold surface mesh. In the current application, a thermal initial value problem is propagated until steady-state conditions are reached. The energy equation for each discrete volume element of a body is formulated as,

$$\left. \frac{dT}{dt} \right|_{e,w} = \left[ \frac{\Delta \dot{Q}_n + \Delta \dot{Q}_t + \Delta \dot{q}_v \forall}{\rho \forall C} \right]_{e,w} \quad (14)$$

Where the sum,  $\Delta \dot{Q}_n + \Delta \dot{Q}_t + \Delta \dot{q}_v \forall$ , represents the generalized net rate of change of energy in element,  $e$ , of wall,  $w$ . This includes transfer in the element-normal and element-transverse directions as well as internal sources of energy generation or consumption. The MPE can use any number of custom sources and sinks leading to a change in the volume's temperature. The general energy balance expected for the SPEAR vehicle is depicted in Figure 38. Note that for the single radiator studies in this section, the environmental sources were lumped into a single heat source, with a single orientation. They are shown separately here as the full vehicle simulations in the next section will consider them individually, as they vary based on the SPEAR's trajectory from

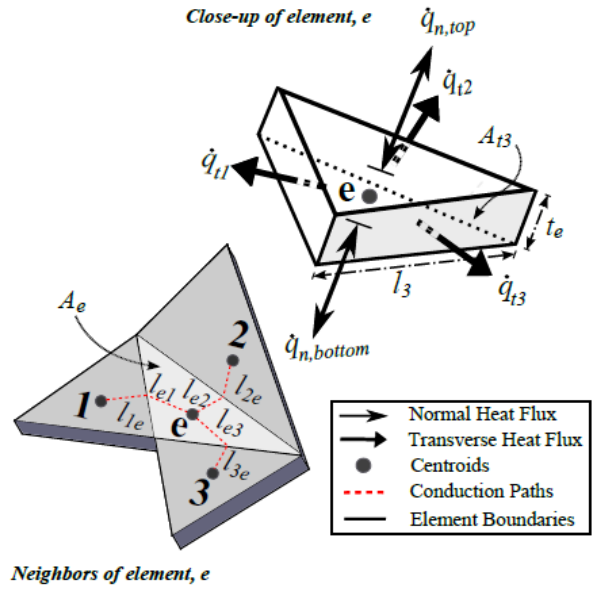


**Figure 37: Example of a volume element and relevant parameters used in the multi-physics engine.**

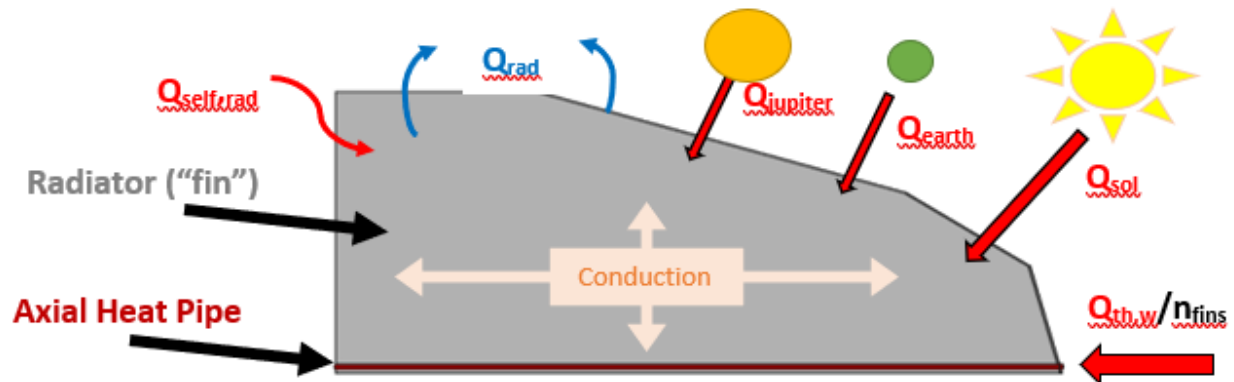


**Figure 38: Single radiator simulation setup. Mars was excluded due to negligible planetary effects during transit.**

Heat pipes offer enhanced heat transfer rates (analogous to increased conductivity) with decreased mass. This is due to the fact that most of the pipes volume is full of naturally-convecting vapor in place of a high conductivity solid. Consider the general heat pipe shown in Figure 39. In this study, heat pipes were modeled using industry standards for water heat pipe performance. Namely, a 10 K temperature gradient was assumed from evaporator to condenser [59]. As well as the thermal properties of the solid wall, the porous wick, solder holding the wick and saturated fluid flowing through the wick were lumped into a single, effective mass. That is to say, the composite properties of the wall were volume averaged. This is reasonable as the heat flux from the vapor core is relatively high compared with the thickness and conductivity of the outer wall, making for a small effective Biot number [58].



**Figure 39: Diagram of a heat pipe from [60].**

The wall and wick were both set as copper and standard Bi/Sn type solder. The wick's conductivity was calculated using the Maxwell equation for porous materials [61]],

$$k_{wick} = k_s \left[ \frac{2 + \frac{k_l}{k_s} - 2\epsilon \left(1 - \frac{k_l}{k_s}\right)}{2 + \frac{k_l}{k_s} + 2\epsilon \left(1 - \frac{k_l}{k_s}\right)} \right] \quad (15)$$

Where  $\epsilon$  is the porosity (set to 0.5 [61],) and  $k_s$  and  $k_l$  are the solid (copper wick) and liquid (saturated water) conductivities, respectively. The density and specific heat of the lumped mass were found by volume averaging the constituents. The vapor core of the heat pipe was considered to have a thermal conductivity defined as [59],

$$k_{vapor\ core} = \frac{Q_{th,w} L_{eff}}{A_{vapor} \Delta T} \quad (16)$$

In each design considered, water was the optimal working fluid for the operating temperature range (300-350 K) and copper housing/wicks are typically used together [59]. Ammonia in aluminum heat pipes are common in space applications but not when there is a significant on-board heat source, that is, they are intended for a lower temperature range typically experienced by spacecraft which do not have a nuclear reactor on-board.

Many different designs and combinations of materials were considered throughout this study. Here, results will be presented from two variations of two designs (four total). Each design consists of a single, axial heat pipe which transports heat out of the reactor bay, to the length of the radiator. The first (Case A, Figure 40a) is the radiator design provided to THP by Howe Industries. This consisted of a constant thickness slab, extending from a relatively wider heat pipe. This is the baseline case and is compared to the improved case (Case B, Fig8b) which includes a wedged radiator slab which transitions from thickness equal to the diameter of the heat pipe (1 inch= 25.4mm), to the tip at a quarter-inch (6.35mm). This simple alteration allows for decreased viewing angle of the other radiators and a decrease in volume of radiator material while increasing radiation surface area. Designs including additional heat

pipes as well as other internal phase change materials were also looked at but were deemed more appropriate for a phase II effort as the physics require additional modeling considerations. This will be discussed more in the final section with example designs already created.

A further increase in performance comes from the material variations considered. Each case, as a slab attached to the Cu-H<sub>2</sub>O heat pipe, was run as solid aluminum or pyrolytic graphite (PG) in a thin copper shell. In the latter case, the PG has far higher axial (transverse) conduction as compared to radial (normal) conduction (see Table 16). The radiators are designed to conduct heat away from the heat pipe and spread it as uniformly as possible over the surface, to be radiated away. With a constant thickness radiator made of Cu and PG, energy is easily brought away from the heat pipe, but has a harder time conducting to the surface to be radiated away. In the case of the wedge, the layers of PG can conduct straight to different parts of the radiator surface, making for an easy spread of the energy and getting the realistic performance as close to that ideal, isothermal performance as possible. Case A's included a solid Al design and a composite, Cu-PG design. The latter consisted of a thin (1mm) thick layer of Cu to encapsulate the much higher performing, but more brittle, PG. Case B's included the same solid Cu-PG combination along with a hollow Cu-PG design which used a 0.5 mm outer layer of Cu and a 2mm inner layer of PG.

**Table 18: Spacecraft surface coatings with associated optical properties.**

Surface Coating	Solar Absorptivity	IR Emissivity	Ref.
Magnesium oxide aluminum oxide (paint)	0.09	0.92	[62]
GSFC white NS43C (paint)	0.20	0.92	[63]
Ebonal C black (paint)	0.97	0.73	[62]
Blue anodized titanium (foil)	0.70	0.13	[63]

For the radiators, low absorptivity in the solar spectrum is desired in order to decrease the external heat loads added to material. On the other hand, the main purpose of the radiator is to radiate as much energy as possible, thus having high emissivity in the infrared (IR) range is very important. For these reasons each radiator was assumed to use a white paint made of magnesium oxide/aluminum oxide which provides the desired optical properties for the surface (see Table 18). An assortment of surface coatings is also shown to give an idea to the range of possible optical properties that could be considered in the thermal design of a spacecraft. As will be seen in the next section, while the radiators value high output over input, portions of the full vehicle may need additional heat input and storage to maintain survival temperatures.

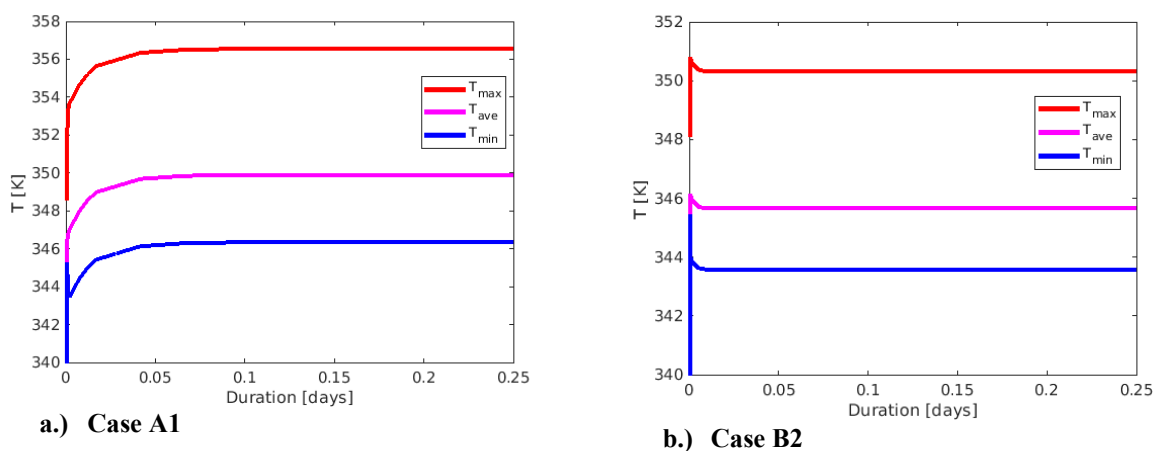


**Figure 40 (a-b): Examples of transient thermal results. The maximum, average, and minimum temperatures in the spacecraft are plotted as a function of transit time after startup.**

As shown in Figure 40, the material selection and wall design of the radiators dictate the extent to which they come close to the goal of a isothermal surface. In tables 19-23, highlights from the main designs considered are provided. These transient responses also show how quickly each design can adapt to changes to its energy balance. The main takeaway is that the case B2 design is the only one to achieve under 50 kg while all designs were able to sufficiently radiate the needed heat load.

Tables 19-23 compile the main results from the single radiator studies. First, the design variable of number of fins was verified. Since the preliminary analysis showed that anywhere from two to four fins would suffice, each of the four cases were tested under these different loads. Tables 19-21 offer a summary of the performance markers for each design. As the number of fins is increased, the temperature of the radiators decrease, as expected. The specific mass, a figure of merit commonly used for radiators, increased (meaning decreased performance per mass) as this surface temperature is decreased for the constant thermal load.

**Table 19: Single radiator performance results with ideal surface properties ( $n_{fins}=2$ ).**

Design Case	$T_{mean}, T_{max}$ [K]	Max $\Delta T$ [K/s]	Mass [kg]	Specific Mass [kg/kW]
<i>A1 (Solid: Al)</i>	414, 434	9.6	79	13
<i>A2 (Solid: Cu, PG)</i>	409, 420	10.1	92	14.3
<i>B1 (Solid: Cu, PG)</i>	409, 423	10.5	79	12.5
<i>B2 (Hollow: Cu, PG)</i>	410, 421	12.8	28	4.5

**Table 20: Single radiator performance results with ideal surface properties ( $n_{fins} = 3$ ).**

Design Case	$T_{mean}, T_{max}$ [K]	Max $\Delta T$ [K/s]	Mass [kg]	Specific Mass [kg/kW]
<i>A1 (Solid: Al)</i>	368, 384	6.9	79	17
<i>A2 (Solid: Cu, PG)</i>	369, 376	7.5	92	25
<i>B1 (Solid: Cu, PG)</i>	371, 377	7.9	79	20
<i>B2 (Hollow: Cu, PG)</i>	371, 377	9.7	28	7

**Table 21: Single radiator performance results with ideal surface properties ( $n_{fins} = 4$ ).**

Design Case	$T_{mean}, T_{max}$ [K]	Max $\Delta T$ [K/s]	Mass [kg]	Specific Mass [kg/kW]
<i>A1 (Solid: Al)</i>	350, 357	5.5	79	25
<i>A2 (Solid: Cu, PG)</i>	345, 351	6.3	92	33
<i>B1 (Solid: Cu, PG)</i>	346, 351	6.6	79	25
<i>B2 (Hollow: Cu, PG)</i>	346, 351	8.1	28	9

From Tables 19-21, only the four radiator designs are able to meet the temperature criteria while only case B2 was able to do so while maintaining a mass under 50 kg. Next, the  $n_{fins}=4$  scenario was simulated with various levels of degraded surface properties. Actual lifetime data for specific surface coating on spacecraft was not included in the current research as such data is not readily available for all surface coatings. Furthermore, the intended outcome of the present study is to help ballpark expected performance and material requirements in order to further guide the SPEAR design. Tables 22-23 include the four cases, with  $n_{fins}=4$ , for 10% and 50% degraded properties. This means that the IR emissivity was decreased by 10% and 50% while the absorptivity was increased by the same. Again, this is not necessarily expected to be the magnitude or even relative trend of degradation but should provide a conservative look at the worst case scenario for decrease optical performance of the surface. As a final note of interest, even though the surface temperatures are increasing in Tables 22-23, as compared to Table 21, the specific mass is staying about the same. This is because the surface properties are not performing at the same high rate as seen in Tables 19-20.

**Table 22: Single radiator performance results with 10% degraded surface properties ( $n_{fins} = 4$ ).**

Design Case	$T_{mean}, T_{max}$ [K]	Max $\Delta T$ [K/s]	Mass [kg]	Specific Mass [kg/kW]
<i>A1 (Solid: Al)</i>	359, 366	5.5	79	25
<i>A2 (Solid: Cu, PG)</i>	354, 359	6.3	92	33
<i>B1 (Solid: Cu, PG)</i>	355, 360	6.6	79	25
<i>B2 (Hollow: Cu, PG)</i>	355, 360	8.2	28	9

**Table 23: Single radiator performance results with 50% degraded surface properties ( $n_{\text{fins}} = 4$ ).**

Design Case	$T_{\text{mean}}, T_{\text{max}}$ [K]	Max $\Delta T$ [K/s]	Mass [kg]	Specific Mass [kg/kW]
<b>A1 (Solid: Al)</b>	413, 427	5.6	79	25
<b>A2 (Solid: Cu, PG)</b>	410, 420	6.4	92	33
<b>B1 (Solid: Cu, PG)</b>	412, 421	6.7	79	25
<b>B2 (Hollow: Cu, PG)</b>	413, 421	8.4	28	8

From the efforts described in this study, it is clear that using advanced, carbon based materials is very beneficial at achieving low specific mass for the thermal management system. Furthermore, achieving low mass while maintaining the required surface area for radiating is shown by case B2. If possible, the Cu encapsulation should be replaced with a lighter, less expensive material such as Al. Follow on work will need to consider the minimum requirements for strength over the associated temperature ranges, but from this phase I effort, the realm of effective designs has been identified and narrowed. Next, the full vehicle is considered with the B2 radiators and the full trajectory of the SPEAR mission.

### 9.3 Trajectory-Based Thermal Analysis of the Full Vehicle

Trajectory information was provided by Atomos, LLC. This included position information relative to the Sun, Earth and Jupiter. This data came in different time intervals for different legs of the journey as well as different coordinate systems. Unfortunately the sun-centered trajectory data was fairly coarse (ranged from 1-12 hours), which made using the eclipse data not possible. This is of minor consequence as internal heat generation from the reactor is much higher than that from environmental sources. However, there is still the need to understand the thermal response of the vehicle throughout an extended journey through space, as isolated areas, far from the reactor and out the Sun's view, could get dangerously cold. Performing a thermal analysis of the full vehicle helps identify these problem areas so proper thermal management techniques can be applied. Such techniques could include thermal straps or additional heat pipes to transfer heat to an isolated component or add an electric or radioisotope heater. The severity and duration of a cold or dangerously hot spot, will dictate what thermal management strategy is applied.

Figure 43(top) shows the Atomos trajectory of the SPEAR vehicle in terms of range from the Sun, Earth and Jupiter. The first two ranges are normalized by one astronomical unit (1 AU = 149.6 million kilometers) which equals the distance from the Sun to the Earth. The range to Jupiter is normalized by the final orbit, making the curve end at Range = 1. Unfortunately, only the final months of the overall trip were provided in the Jupiter reference frame, hence the short curve for  $R_{\text{Jupiter}}$ . As can be seen from the corresponding heat flux attributed to each of these celestial bodies (Figure 41, bottom), the final approach heating from Jupiter is orders of magnitude lower than that from the Sun. Similarly, it should be noted that the trajectory's proximity to the orbit of Mars was not considered but would result in an additional heat source. This would at maximum (closest approach) be of similar magnitude to that of Earth. However, since Mars is not the destination, it is likely this source of heat will not be significant and thus its exclusion from the current study is reasonable.



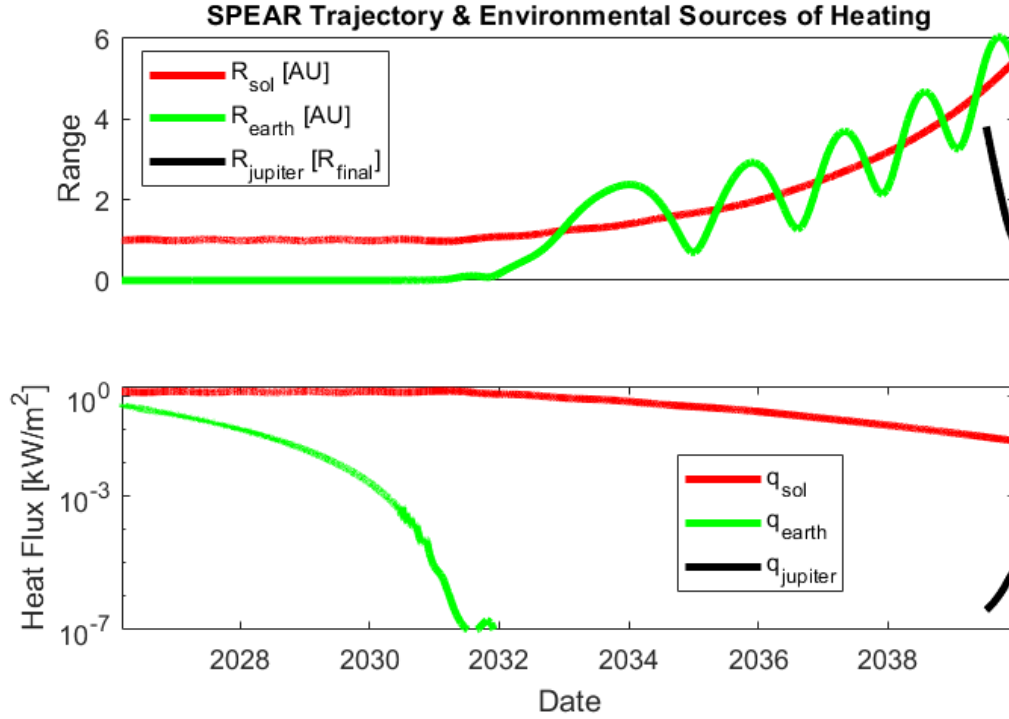


**Figure 41: (Top) Trajectory data shown as nondimensional ranges from the Sun, Earth and Jupiter. (Bottom) Maximum heat fluxes expected from space environment. Shared x-axis (at bottom).**

The heat fluxes considered in Figure 41(bottom) are direct solar irradiation, planetary albedo (reflection) and planetary infrared. Each of these sources are a function of the range from the body scaled by the solar constant,  $I_{sol}$ . Mathematically these fluxes can be expressed as with the following equations from [57],

$$q_{sol} = I_{sol} \left( \frac{AU}{R_{sol}} \right)^2 \quad (17)$$

$$q_{earth} = \frac{I_{sol}}{4} \left( \frac{r_{earth}}{R_{earth}} \right)^2 [1 + 3\rho_{earth}] \quad (18)$$

$$q_{jupiter} = \frac{I_{sol}}{4} \left( \frac{r_{jupiter}}{R_{jupiter}} \right)^2 [1 + 3\rho_{jupiter}] \quad (19)$$

Where the fluxes from planetary sources (Eqs. 18 and 19) include both the albedo and infrared terms. Each of these fluxes then scale based on the specific view factor of a surface on the SPEAR vehicle and each of the sources. The constants corresponding to each of these bodies are found in Table 24.

**Table 24: Planetary parameters of Jupiter and Earth. Mars neglected due to minimal effects on spacecraft heating.**

	Earth	Jupiter
Radius, $r$ [km]	6378	69911
Reflectivity, $\rho$	0.3	0.5

In order to run a large-scale simulation of the entire SPEAR vehicle for the long, 13-year mission, a reduced order model of the vehicle was generated. Namely, the reactor bay, central support pylon, Cubesat holders and hall thrusters were all replaced with smooth, simple shapes. Additionally, only aluminum coated with the magnesium oxide aluminum oxide paint, was considered for structural elements outside of the radiators. This provides a good

first take on the overall thermal fluctuation throughout the journey, while not getting caught up on specific design details which may or may not continue in the design process. Future work could consider specifically chosen component geometries under the same range of conditions shown in the models herein and apply different materials and surface coatings as dictated by the subsystem requirements and resulting temperature ranges.

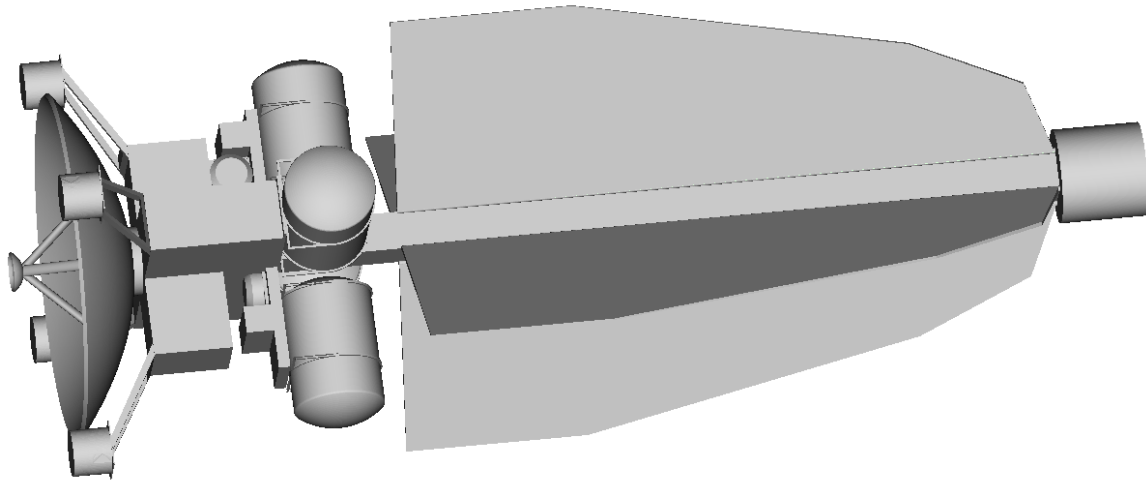


**Figure 42: Simplified 3D mesh of full vehicle used in simulations.**

The full vehicle simulations used a constant temperature boundary condition on the cold side of the thermoelectric converters and did not include the surface temperature of the reactor. A constant boundary temperature of 350 K was chosen to match the intended ‘cold-side’ of the ATEG and subsequent ‘hot-side’ (evaporator) of the radiators’ heat pipes. Furthermore, the current realization of this simulation shows the waste heat from the reactor dominating the overall thermal response, making for nearly constant temperatures throughout most of the journey, with the maximum surface temperature being held at 350K.

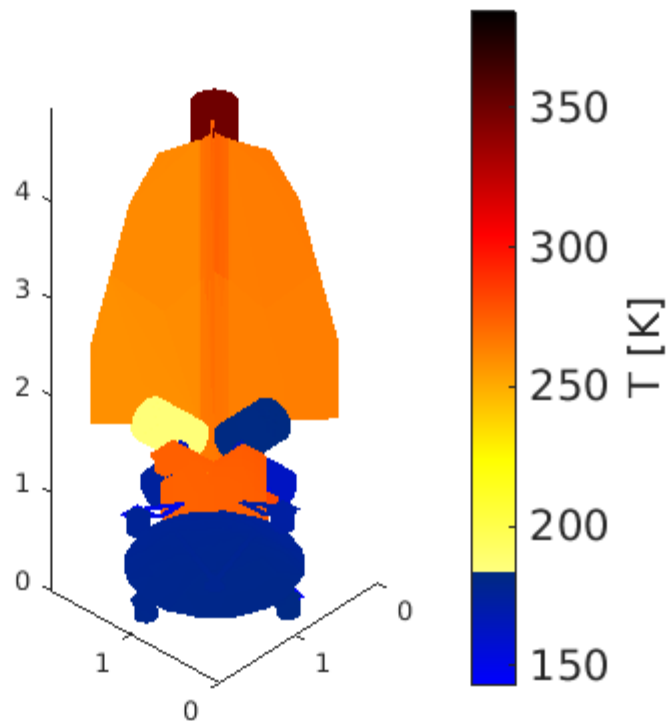


**Figure 43: Thermal analysis results from the full mission trajectory.**

Figure 43 shows the full vehicle's temperature distribution as it reaches Jupiter. Cold regions ( $<200\text{K}$ ) are shown in blue. The reactor, being isolated from this model, represents the temperature of the ATEG heat rejection. Clearly, some of these components seem thermally isolated from the rest of the vehicle. For the propellant tanks, this is desired as the Xenon inside is intended to be at its triple point ( $\sim 166\text{ K}$ ). One of the tanks, which is in the direct sunlight, is noticeably warmer than the others. No rolling was considered in the trajectory and for a large portion, the sun remains facing a single side of the vehicle. Future work will need to consider the energy requirements of inducing a roll at a given rate, as needed to maintain more uniform temperature around the vehicle. Such extensions are now feasible that a thermal model of the full vehicle has been created with the trajectory data incorporated.

Additional simplifications inherent in the current full vehicle model are a lack of internal heat sources from subsystems such as the power conditioning unit, communication electronics and electric thrusters. These sources are small in comparison to that of the waste heat of the reactor and to a lesser extent, to the external heat sources from celestial bodies. However, as the full vehicle simulations show, some of these portions of the vehicle are reaching very cold temperatures ( $<200\text{K}$ ). Including these internal sources of heat will act to both increase the fidelity of the results and show increased viability in the expected temperature ranges for the proposed mission. If these internal sources do not suffice to ensure the temperature limits desired for the final mission plan, many design options exist to mitigate the problem. These include additional heat pipes to transfer waste heat to other parts of the vehicle, or local heaters if additional heat pipes are not desired. These could be radioisotope heaters or resistive heaters which would draw from the reactor's electricity generation.

#### 9.4 Considerations for Phase II Thermal Analysis

Many aspects of thermal design and analysis were not able to fit into the scope of the phase I effort. Some of these have been mentioned already, including additional materials and surface coatings for different components as well as internal heat sources which are expected from on-board subsystems. However, the major follow-on task suggested by the author is that of the radiators. Added fidelity in heat-pipe models as well as more advanced materials

provide potential for further optimization. Including added understanding of realistic surface degradation over a long duration space mission.

As one immediate follow-up, secondary heat pipes could be applied in the radiators in order to adequately spread the heat across the radiators acreage (see Figure 44). This study used simplified models of the primary and secondary heat pipes based on published performance characteristics. Since the ATEG is a novel concept, large improvement may be possible from further optimization of the heat pipes by modeling the multi-phase fluid dynamics occurring inside the pipes. But the effective-conductivity models are not be sufficient to get a high confidence estimate of both a primary and secondary (or more) heat pipes. Additionally, as evinced in the preliminary analysis, as well as mentioned by Atomos in their preliminary mass estimate, allowing for a higher  $T_{low}$  for the reactor will allow for smaller radiators. However, this decreased mass would need to be compared with the modified cold-side temperature of the reactor.

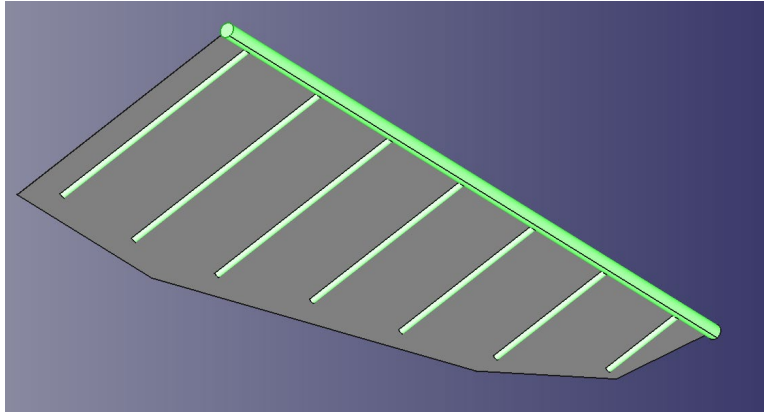


**Figure 44: Alternative radiator design. Heat pipes highlighted in green.**

Finally, now that a large-scale model of the vehicle throughout the trajectory has been created and tested, additional design considerations such as heaters, or simply alternative surface coatings or structural materials could be vetted in a formal design optimization process. Such activities were considered outside of the scope of the Phase 1 but represent excellent starting points in a Phase II effort.

## 10 CUBESAT SWARM

One of the most unique aspects of the SPEAR mission to Europa is the small cluster of 10 CubeSats included as its payload. Each CubeSat has a mass of 7 kg and it equipped with several instruments to maximize its life detecting abilities. deploying this swarm increases the chances of collecting particles from plumes and possibility of going directly through a plume to collect samples. Missions that utilize a single spacecraft likely do not spend enough time or have a high enough probability of intercepting a plume or collecting enough material from the atmosphere to analyze for life. This section will outline the mission architecture and design of the CubeSats to detect life at Europa.

Since their inception, CubeSats have grown from simple technology demonstrators to versatile satellites capability of complex missions and swarms for remote sensing and telecommunications. They are part of one of the fastest growing space industries and revolutions in recent years [64]. Until recently they have been restricted to Earth's orbit, but with the advent of the MarCO CubeSats they have begun to venture into deep space [65]. These tiny satellites proved that CubeSat technologies have advanced far enough to survive and function in deep space while performing tasks of significant value. SPEAR will deploy a small swarm of CubeSats that will accomplish several key science goals in the Europa environment, including mapping the surface and searching for life.

### 10.1 Europa Environment

Europa has been of keen scientific interest for many decades and the topic of many future deep space exploration missions. In fact, a Europa exploration orbiter is second on NASA's decadal survey [2]. It has been studied several times from probes, space based telescopes, and ground based telescopes. With every study, evidence grows

for there being a large sub-surface ocean trapped below an icy crust that has the potential to harbor life. This has been one of the primary drivers behind the exploration of Europa over other icy moons. Europa has a slightly elliptical 3.5 day orbit around Jupiter, which causes tidal heating of the subsurface ocean due to friction [66]. Many of the surface features on Europa can be explained by the existence of a subsurface ocean moving ice around in large rifts, rafts, wedges, and chaotic regions where it is believed water or warmer ice chunks have lifted the surface of the ice sheet [66]. This does not necessarily present evidence of a liquid ocean, as underneath the ice shell there could be warm convecting ice [66]. However, the Galileo probe observed a change in Jupiter's magnetic field around Europa, eluding to the possibility of a large ocean that is a good electrical conductor because of dissolved salts [66]. A liquid ocean makes Europa one of the primary locations to search for life beyond Earth, however, finding life at Europa will be a challenging task.

### 10.1.1 Evidence of Plume Activity

To directly study the subsurface ocean for life, one needs access to it. Penetrating the thick icy crust requires a large power source to melt or drill through the ice. It may be nearly impossible to melt through the ice without a nuclear power source, and the transit, communications, and safety of such a probe remain in question. However, it has been discovered that Europa may produce intermittent plumes that release liquid water. These plumes may contain evidence of life below the surface of the ice and offer one of the simplest methods for discovering life on Europa. In 2012 scientists using the Hubble Space Telescope discovered a large plume erupting from near the south pole of Europa with an estimated height of 160 km [67]. Utilizing the Hubble Space Telescope again in 2014 and 2016 two more plumes were identified [4]. The 2014 event reached an estimated 30 miles in altitude, while the one imaged in 2016 rose 62 miles from the same general location [68]. Determining the most likely position of these plumes is of great importance. The fact that these plumes were observed in the relatively same location may indicate they came from the same source, such as a crack or hot spot under the ice. This aids in the mission planning behind the CubeSat swarm. In 2019 the confirmation of water vapor from another plume was also confirmed [69]. The timing and duration between plumes appear to remain relatively uncertain. Measurements from the SPEAR probe and its CubeSats would help to determine the frequency of these plumes and their locations.

In the most recent 2019 finding, the fact that water vapor remained in the atmosphere around Europa is encouraging. While the goal of the CubeSats is to fly through these plumes there is always the potential for a plume to not appear in the relatively short 30 day mission. If water vapor remains in the atmosphere of Europa for an extended period of time, the CubeSats may be able to fly through the vapor and analyze its composition and test for life. The probability of intercepting distributed water particles would be much higher than waiting for intermittent plumes to appear and potentially dissipate by the time the CubeSats can reach the plume. With a swarm of CubeSats the probability of intercepting plume particles increases dramatically over a sole orbiter. Each CubeSat will also be able to study the Europa environment to detail presenting a wealth of information on one of the most important moons in our solar system.

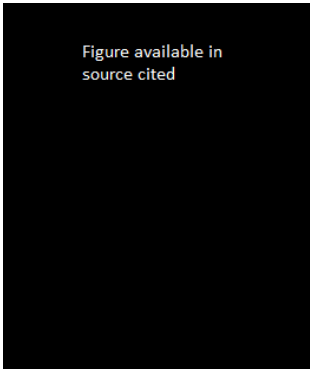


Figure available in  
source cited

**Figure 45: Results from a study conducted on particle ejecta from a plume on Europa. The two lines are the recommended upper and low altitude suggestions by Southworth et. al. for interceptor missions. Lower altitudes may yield greater impact rates due to the plume slowly returning to the surface, but these particles may damage the spacecraft if it encounters the plume while erupting. Figure courtesy of [70].**

### 10.1.2 Plume Mechanics and Particle Behavior

As discussed in previous sections, there have been several instances where the evidence for plumes and water vapor around Europa have been validated. The period and mechanics of these plumes remains disputed as either not permanent or periodic in nature [70]. Due to the inconsistent nature of the plumes one theory suggest that the plumes are triggered by mechanical stress opening cracks in the ice to release debris and eventually resealed due to mechanical stress again, or debris/condensation of water to seal the fracture [70]. The composition of the plumes is also questionable and whether they consist of icy particles, gaseous vapor, or a mixture of the two. The plume ejection rate according to some models can reach 5 kg/s [70] or higher with number density of particles decreasing with altitude as seen in Figure 45 from Southworth et al.

The plumes ejected material on Europa does not appear to reach escape velocity of roughly 2.025 km/s [70] and will return to Europa's surface. As the altitude above the plume decreases the size and number of particles changes. Smaller particles are more likely at higher altitudes while larger particles are more prevalent at lower altitudes [70]. This is important for spacecraft safety as impact more massive particles can significantly damage a spacecraft at orbital speeds. The number of particles impacted per second also changes, a simulation of this is visible in Figure 46 from Southworth et al.

Spacecraft such as Galileo, Europa Clipper, and the Jupiter Icy Moons Explorer, have only or will only conduct flybys of Europa, which severely limits its ability to intercept plumes. The sporadic nature of the plumes makes their location unpredictable, causing these probes to potentially miss them entirely. SPEAR's CubeSats are uniquely suited to cover a large area of Europa that could be subject to plume activity and will remain in orbit searching for evidence for much longer periods of time.

Spacecraft such as Galileo, Europa Clipper, and the Jupiter Icy Moons Explorer, have only or will only conduct flybys of Europa, which severely limits its ability to intercept plumes. The sporadic nature of the plumes makes their location unpredictable, causing these probes to potentially miss them entirely. SPEAR's CubeSats are uniquely suited to cover a large area of Europa that could be subject to plume activity and will remain in orbit searching for evidence for much longer periods of time.

### 10.1.3 Habitability of Europa

Europa is without a doubt an extreme environment, but with a potentially large liquid ocean it is a prime candidate to discover life outside of Earth. Energy sources for organisms on Europa remain speculative and it is believed that most organisms on Europa would subsist of non-traditional energy sources [71]. Some predict that organisms may get their energy from methanogenesis from hydrothermal vents deep in Europa's ocean [71]. In addition to this, the radiation environment may spur the ecosystem on Europa. Movement of ice would allow the surface, which has been bombarded by radiation, to transfer molecules to the sub-surface ocean from which organisms could collect energy.

While microorganisms may be present on Europa, it is predicted that Macrofauna would be lacking as the estimated oxygen content is not high enough to support life [71]. It would be expected that if organisms are detected they would be a form of extremophile able to survive the harsh conditions of Europa. Depending on the method of energy exchange simple organisms may inhabit the upper portion of Europa's surface ice for the energy they can

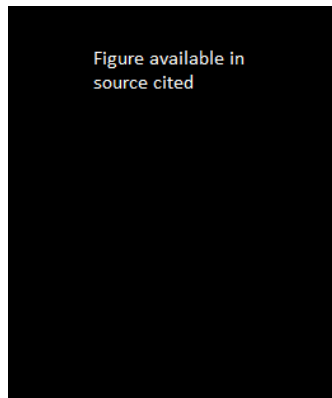


**Figure 46: Estimated particle size by Southworth et. al that would be present at various altitudes during a plume event. Smaller particles are less likely to damage spacecraft, but may have limited particle density. Figure courtesy of [70].**



obtain there [71]. This would be an ideal scenario- if a plume occurred because of a fracture in the ice, this would be the first location where water would be ejected into space for the CubeSats to intercept and analyze. With a higher density of organisms in this area, the probability of detection increases.

## 10.2 Wireless Power Transmission

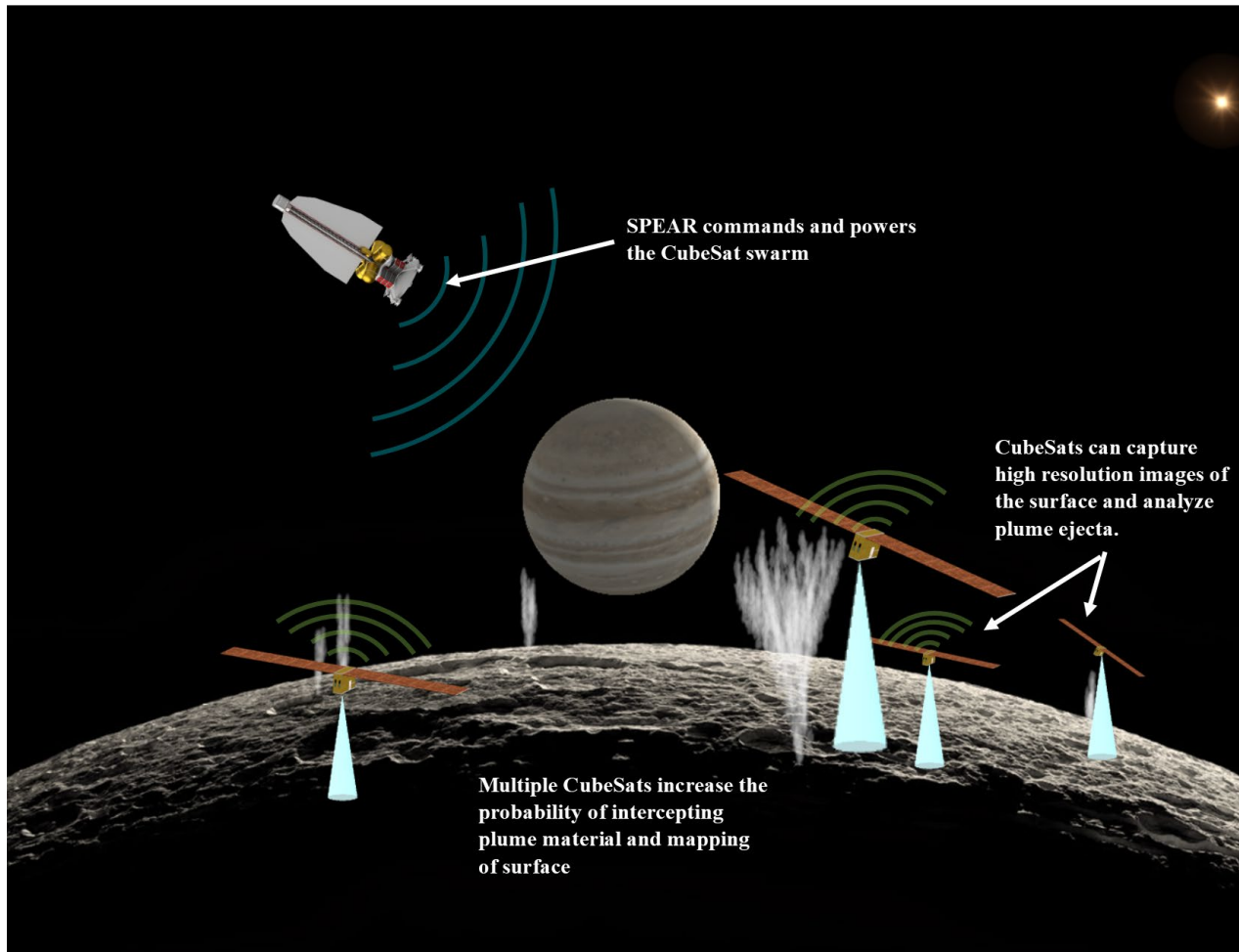


**Figure 47: A total of 10 CubeSats will be deployed from SPEAR, forming the life detecting swarm that will intercept plumes and study the surface of Europa. Having multiple spacecraft allows for a higher probability of intercepting a plume and gathering life forms within the material. SPEAR transmits and receives data from the CubeSats as well as powers them through RF charging. An intersatellite link between the CubeSats can be used to transmit data to SPEAR if it is not in radio contact or communicate new information.**

The CubeSats swarm will need to endure one of the harshest environments a CubeSat has ever been exposed to. At Europa there is only  $50.26 \text{ W/m}^2$  solar flux available for power [72], so at these distances most missions utilize radioisotope thermoelectric generators (RTGs) to power the spacecraft. Only until recently have solar panels been considered for missions out to Jupiter including Juno and the Europa Clipper. Utilizing an isotope source within the CubeSat may be possible, but an MMRTG is too large and expensive to use on the CubeSats. Creating a new, smaller RTG introduces many regulatory and safety concerns, especially considering that SPEAR is designed to be commercially available to industries for exploration. Large, mass intensive solar arrays could be used to produce

enough power for the CubeSat, but this introduces a significant failure mode for these satellites as many folding solar arrays would need to be combined together and deployed after a long hibernation inside the SPEAR spacecraft.

After SPEAR has entered Orbit around Europa, the scientific aspect of the mission will begin. The goal of the mission is to capture particles from plumes shooting out from the surface of Europa and analyze the particles for signs of life. In order to capture particles from plumes, SPEAR will deploy 10 CubeSats to fly through the plumes collecting as many particles as possible. The CubeSats will capture the particles and analyze them via Raman spectroscopy. Afterwards, the CubeSats will relay this information back to Earth via SPEAR. An intersatellite link will also be set up allowing the CubeSats to relay important information to each other, although their ability to alter course will remain limited.

The scientific aspect of the mission is set to last only 30 days due to the intense Jovian radiation field harming the CubeSats internal components. Even for the short duration, the CubeSats do not have a battery large enough to last the duration of the mission while accomplishing all of their science goals. Therefore, they must be charged as they orbit Europa. Each CubeSat will rely on wireless radio frequency (RF) power transfer to recharge their batteries.

With SPEAR probe capable of maintaining 3 kW of electrical power at Europa, the possibility of using radio frequency charging or a laser to recharge solar cells was explored. Recharging via RF waves is most favorable as the transmission system already exists and additional equipment will not be needed. However, wireless charging has never been used to directly power a spacecraft for long periods of time. Power beaming can be a highly efficient process compared to solar arrays and at moderate distances the power density of the RF field can far exceed that of the solar irradiance at Jupiter. In order to successfully harvest the RF power from SPEAR a large rectenna must be used by the CubeSat to convert the RF waves to an electrical input. The power received by the CubeSat can be determined by the following equation from [73].

$$P_r = \frac{P_t G_t}{4\pi R^2} A_r \eta \quad (20)$$

In this case  $P_t$  and  $G_t$  represent the power and gain of the transmitter,  $P_r$  and  $A_r$  is the power received by the rectenna and the effective aperture area of the rectenna,  $R$  is the distance from SPEAR to the CubeSat, and  $\eta$  is the efficiency of the system. There are several factors that determine the performance of far-field RF charging that will be discussed in the following sections such as frequency, transmitter size and Distance.

### 10.2.1 Transmitter Size

The transmitter size directly affects the gain and beam divergence of RF-charging. Gain is defined by the following equation provided by [74] :

$$G_t = 10 \log_{10} \left( \left( \frac{\pi D_t}{\lambda} \right)^2 \eta \right) \quad (21)$$

Where  $D_t$  is the antenna diameter,  $\lambda$  is the wavelength and  $\eta$  is the antenna efficiency. Note that  $G_t$  is in units of dB. The beam divergence has been calculated from the following equation provided by [75]:

$$\theta = \frac{\kappa \lambda}{D_t} \quad (22)$$

Where  $\kappa$  is a factor which varies depending on the feed illumination pattern and reflector shape [75]. Because the antenna diameter is fixed, the frequency is directly proportional to the received power and inversely proportional to the beam divergence. Increasing the antenna diameter would increase the gain of the antenna and as a result the received power based on equation 12. However, this would decrease the beam divergence expressed in equation 14 which limits the beam area the CubeSat will pass through to charge. It should be noted that equations 12, 13, 14 hold true only at far field lengths which can be calculated from the following equation provided by [76]:



$$r > \frac{2D_t^2}{\lambda} \quad (23)$$

Where in this case,  $r$  is the distance from the CubeSats to the SPEAR probe. If the distances is greater than the value determined from equation 15 the CubeSats are said to be in the far field region.

### 10.2.2 Beam Divergence

Increasing beam divergence results in the area that is being irradiated with RF waves become larger. This could allow for a greater number of CubeSats to be charged at the same time, depending on the orientation. However, as the beam divergence increases, the power received decreases. This relationship is visible in Figure 48. Decreasing the beam divergence is accomplished through changing the frequency or decreasing the antenna diameter. At a certain point it becomes more efficient to send energy via a laser beam, however, attempts have been made to avoid this additional power system to reduce mass and complexity. With a fixed diameter the only method to decrease the beam divergence is to increase the frequency which consequently increases the gain of the antenna. This makes for a very powerful and concentrated beam for charging in a small area. In order to increase both the power received and the beam divergence the transmitter diameter and frequency must be increased simultaneously while also increasing transmitter power. SPEAR is limited to a maximum of 3kW of power, and increasing the transmitter diameter is difficult as it has been sized to fit within the confines of small/medium class launch vehicles.

### 10.2.3 Distance

The distance between the transmitter and the receiver influences the levels of received power. This relationship is visible through equation 12, where the power received for an equivalent area follows the inverse square of the distance. Figure 2 displays the far-field charging at a frequency of 100 GHz and a transmitter diameter of 1.5 meters. Because receiver that is further than 12 km away effectively receives zero power, distance is a limiting factor when it comes to RF charging. Increasing the CubeSats rectenna size can compensate for this, but this may require a large deployable mechanism for each CubeSat to receive larger amounts of power at greater distances.

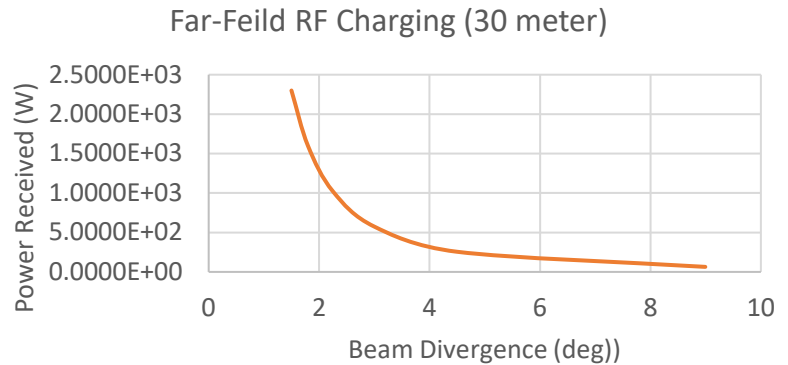


**Figure 48: Power received vs the beam divergence of a fixed antenna size. Changing the frequency of the RF generator changes the beam divergence; at higher beam divergences the received power drops considerably because of the lower frequency and lower power density.**

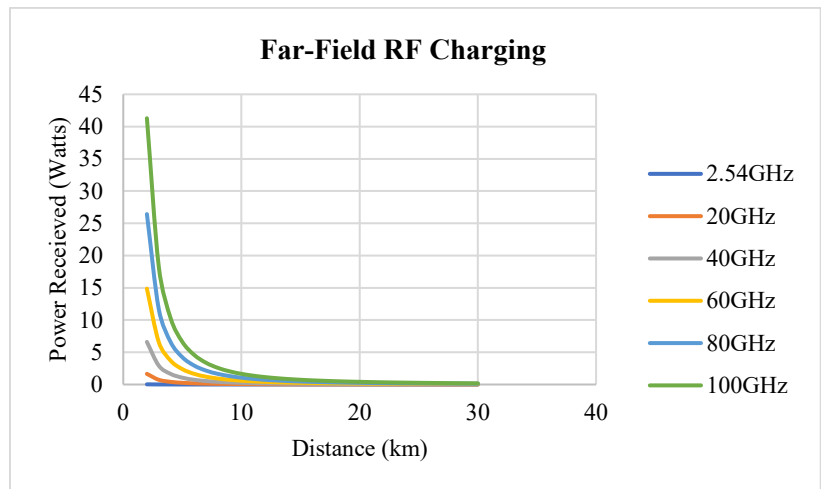


**Figure 49: The most limiting factor in wireless power transfer is the distance between the transmitter and the rectenna. Following the inverse square law, as the distance increases the power received per unit area is decreased.**

#### 10.2.4 Frequency

While the antenna diameter is currently fixed based on launch vehicle constraints the beam frequency/wavelength is easier to change. In Figure 49 one can see the difference the beam frequency has on the total received power. Distances closer to SPEAR are not included as these are within the near-field length and would be subject to difference constraints. As will be discussed in a later section, CubeSats this close will be traveling too fast to charge for a meaningful amount of time.

Figure 49 shows the absorbed power for a fixed CubeSat rectenna size. One must take into consideration the beam divergence as this is inversely proportional to wavelength. A low beam divergence results in a smaller area subjected to the RF beam; so while the CubeSats may intercept the very powerful beam, they would remain inside its influence for a very short amount of time depending on their position relative to SPEAR. This will be discussed further in the next section.



**Figure 50: Two CubeSats are deployed at a time from SPEAR to limit effects on SPEAR's ADCS system. After deployment and recovering from any deployment errors each CubeSat conducts a small orbital maneuvering burn to position itself away from SPEAR. After the burn the rectenna is deployed which will allow SPEAR to power the CubeSats during the mission. After complete deployment of the rectenna array, the CubeSats begin studying Europa's environment and collecting any debris. Dispenser modeled after Planetary Systems Corporation 6U canisterized satellite dispenser [19].**

### 10.3 CubeSat Swarm Operations

Once in orbit around Europa, SPEAR will deploy two CubeSats at a time, one from each side of the spacecraft. Each CubeSat deployer ejects the CubeSat with a small delta- $v$ , but the propulsion system for each CubeSat will be used to propel them to their desired orbits. This process is visible in Figure 50. It should be noted that the rectenna in this image is based on current technologies and has roughly a  $1\text{m}^2$  area.

Each CubeSat will have a different inclination than SPEAR but retain the same orbital period. This means the two satellites will pass each other twice near the same location every orbit, and the distance between SPEAR and the CubeSat will act in a sinusoidal fashion as seen in Figure 51. The velocity of the CubeSat relative to SPEAR is greatest when the two satellites are closest together as seen when evaluating Figure 51 as well.

Figure 52 illustrates the orbits of the satellites as well as their positions in time. The CubeSats with their own propulsion system will be capable of changing their inclination by 7 degrees, or travel up to 215 km away from SPEAR. This would create a large area for CubeSats to fly through plumes. Unfortunately, the CubeSats are limited by the RF far-field charging capabilities, and can not be charged efficiently at that inclination. However, there are other methods which can be used to extend their range as discussed below in the improvements section.

### 10.4 Charging Considerations

The factors that affect the CubeSat charging are the relative distance between the two satellites, the components that make up RF far-field charging, and the antenna orientation. As stated earlier, the relative distance is dependent on the CubeSats inclination change; however, the effective charging distance is limited by the RF far-field charging parameters. Therefore, the furthest distance the between the two satellites cannot exceed 12 km. That limits CubeSats to a 0.5-degree inclination change (which only requires a 10

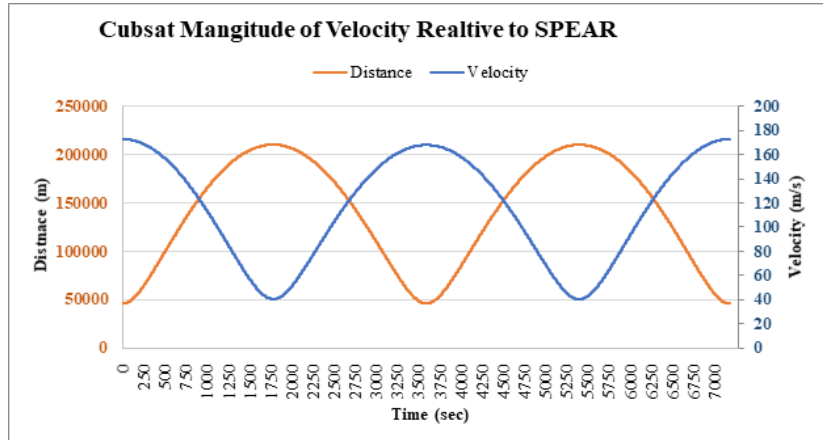


**Figure 51: Magnitude of the distance and velocity of a single CubeSat relative to SPEAR after deployment. SPEAR must charge these CubeSat during their orbit with a minimal expenditure of ADCS systems.**

**Orbital Map of SPEAR and CubeSat**

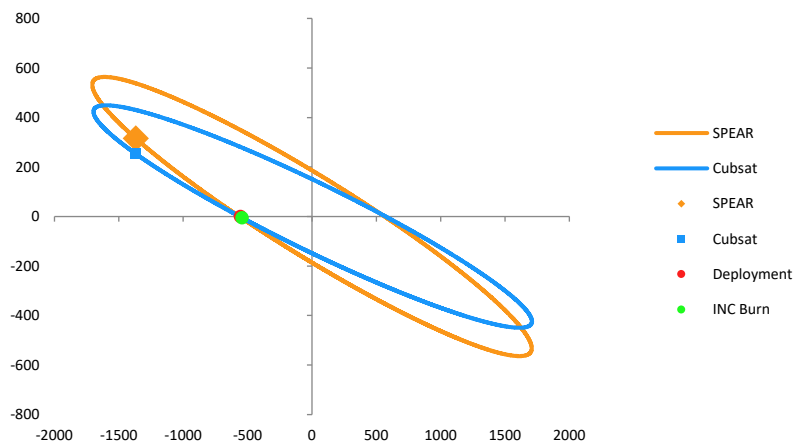


**Figure 52: Demonstration of CubeSat orbit and SPEAR orbit around Europa. The combination of 10 CubeSats and the SPEAR probe will allow for a greater probability of intercepting particles for analysis.**

m/s change in velocity). The RF far-field charging parameters are limited by size/weight, and current technology. The antenna orientation is the arguably the most constraining factor as the CubeSats need to be charged and data relayed back to Earth. Angling the SPEAR craft slightly may allow for both the CubeSats and the earth to be reachable without moving the craft straining its ADCS capabilities. From the frame of reference of the SPEAR probe, the CubeSat swarm will deploy and travel only up and down behind the craft. If the RF beam is aimed directly behind the craft and the CubeSats pass by, they will spend a very short period of time in the beam. Due to this, aiming the dish at an angle will increase the time spent charging. This is also where the larger divergence effects performance, as a wider beam divergence will increase the area bisected by the path of the CubeSat.

#### 10.4.1 Antenna Orientation

SPEAR will attempt to utilize its high gain antenna to beam power the CubeSats and as a result will need to position itself and maintain a constant orientation. This will allow all ten of the CubeSats to pass through the beam at different times to receive power. A tracking option was not selected at this stage due to the machinery required to move a large antenna.

By sending out power in a single direction and allowing the CubeSats to naturally pass through the beam, the weight and costs can be minimized. Locking SPEAR in place does come with its own set of challenges, as the optimum antenna orientation is dependent on the characteristics of the CubeSats orbit relative to SPEAR. In order to optimize the antenna orientation Howe Industries developed software capable of factoring all the parameters discussed that effect RF-charging and performed several trade studies.

The trade studies were conducted to determine the optimum antenna orientation for charging. The initial assumption was to align the antenna so that the CubeSat passes through the beam when it's closest to SPEAR. However, it quickly became apparent that the CubeSat was moving too quickly through the beam to reliably receive any power no matter how large the beam divergence. Figure 51 shows just how fast the CubeSat is moving when near SPEAR, and Figure 48 not only indicates how little power the CubeSat would receive at 30 meters (the closest approach), but also shows how quickly the CubeSat would pass through the beam given the size of the beam. The second option was to align the antenna so that the CubeSat could spend the most amount of time within the beam which would be when the CubeSat was moving the slowest; however, the CubeSat is the furthest away at this point. As stated earlier, the distance between the CubeSat and SPEAR is limited due to effectiveness of RF Charging as seen in Figure 49. Therefore, the trade studies were running at the maximum inclination change of 0.5 degrees which results in a maximum distance between the two satellites at less than 12 km. the trade studies showed the second method was more effective.

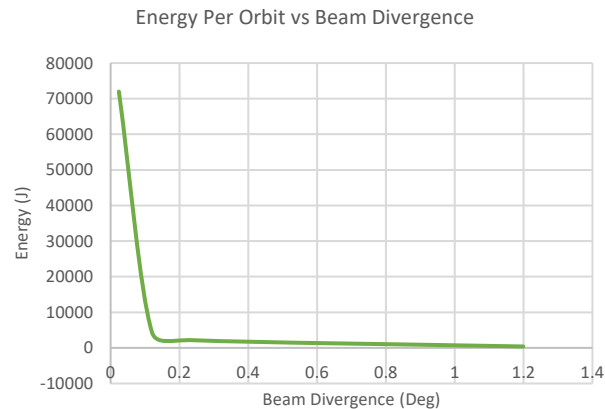


**Figure 53: A larger beam divergence allows for a larger area subjected to RF radiation, but at a lower power density. Decreasing the beam divergence increases the power density, and therefore the absorbed power.**

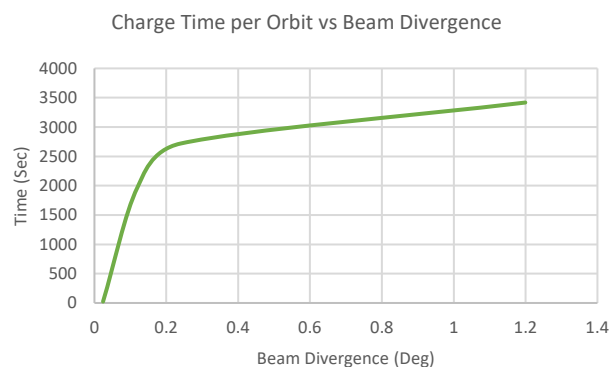


**Figure 54: While supporting high power densities, lower beam divergences are not able to target CubeSats for long periods of time.**



### 10.4.2 Estimated Absorbed Power and Charging Regime

Once the general angle orientation was determined, the RF parameters could be optimized to determine the most effective way to supply the CubeSat with power. To gain the most power, the transmitter antenna was set to the maximum size that could fit on SPEAR (1.5 meters in diameter). The frequency was then varied which in turn altered the beam divergence and the power. Figure 53 clearly shows the lesser the beam divergence the greater the total energy received by the CubeSat per orbit. Figure 54 shows the charge time is substantially small for beam divergences less than 0.1 degrees. Charge time is essentially a measurement of error (i.e. the less charge time you have the less room for error).

If the CubeSat were to charge when it was closest to SPEAR, the charge time would be less than a second, but that amount of time spent within the beam leaves little room for error. Should the inclination maneuver miss fire, the CubeSat orbit would be altered; therefore, it may not pass through the beam. Additionally, the CubeSat is at the closest position to SPEAR, so divergence of the beam creates the smallest area for the CubeSat to pass through, whereas the greater the distance between CubeSat and SPEAR the larger the beam area which means the more time spent within the beam hence, less penalties from errors. With that said, the ideal beam divergence, according to Figure 54 and Figure 55 is approximately 0.1 degrees which equivalates to a frequency of 100 gigahertz and would supply about 4500 joules of energy (or 1.25 whr) per orbit. This is substantially lower than 5.5 whr consumed per orbit, luckily there are ways to improve the supplied power which will be discussed shortly.

Using the optimized values for a 0.5 inclination, we calculate the CubeSat will receive 4457 joules over 1973 seconds. Figure 55 shows when and where the CubeSat is being charged, and Figure 56 shows an estimated amount of energy the CubeSat receives and consumes per orbit.

### 10.4.3 Improvements to Charging System

One way to increase the supplied energy to the CubeSats would be to add a secondary charging mechanism such as a laser or a separate tracking antenna to pair with the locked RF charging. Adding a secondary charging outlet, one that is smaller and capable of tracking the CubeSat as it passes closest to SPEAR, would greatly influence the total energy supplied per orbit. Initial estimates suggest a 473 nm laser with a divergence of 0.1 mRad and 25 watts could supply the CubeSat with 5,000 joules (1.38

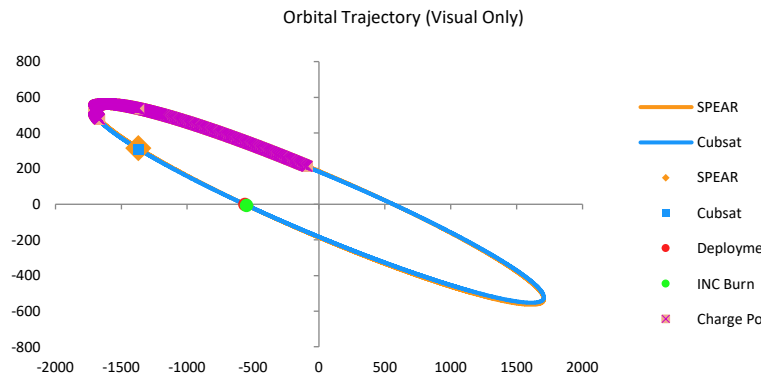


**Figure 55: Orbital map of locations where SPEAR will be able to charge an individual CubeSat. SPEAR has been angled to provide the maximum amount of power for this CubeSat with optimized beam divergence.**

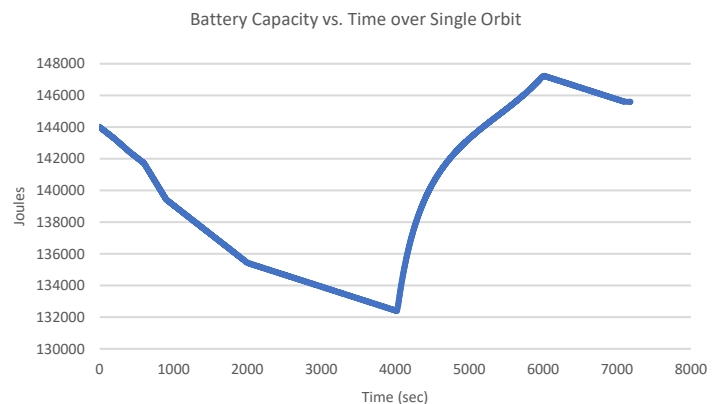


**Figure 56: The estimated total power available for the CubeSat as it completes one orbit. SPEAR is able to supply enough power to the CubeSat to allow it to continue its science goals throughout its orbit.**

whr) if it were able to track the CubeSat within 500 meters of SPEAR. It may be difficult to track and charge the swarm of CubeSats, so this may be on a “as needed” basis depending on the individual CubeSat power consumption.

However, the simplest way to improve the supplied energy per orbit is to increase the rectenna on the CubeSat. The trade studies above used a 0.5-meter diameter rectenna (assumed circle and added correction factor for calculations). If future technology allows for a larger rectenna on the CubeSat, it would increase the received energy per orbit by almost 9000 joules (2.5 whr) per meter increase in diameter. Figure 57 shows the effects of increasing the rectenna diameter on energy received. According to Figure 57, a beam divergence of 0.1 degrees and a rectenna diameter of 2.5 meters would be capable of supplying energy greater than the 20,000 joules (5.5 whr) consumption per orbit. Increasing the rectenna diameter would also allow more flexibility with beam divergence for example, a 0.15-degree beam divergence could still supply the 5.5 Whr and increase the total charge time according to Figure 57.

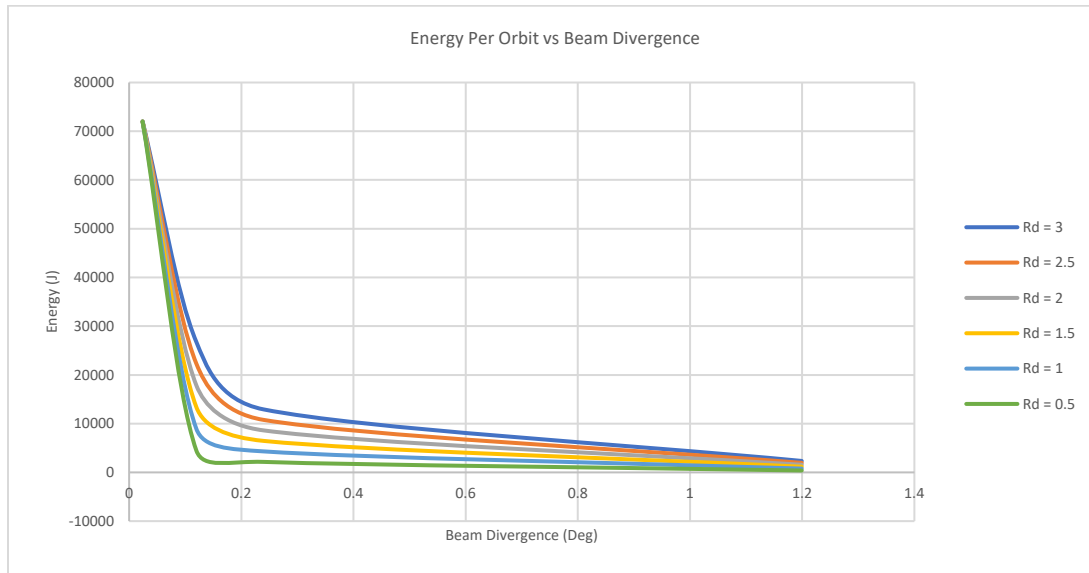


**Figure 57: Potentially one of the simplest methods to increase the absorbed power of the CubeSat is to increase the rectenna size. From the plot above one can see how at the same beam divergence a significantly larger amount of energy can be absorbed with slight increases to the rectenna area.**

If larger distances between CubeSats are desired this would limit the amount of power that SPEAR can provide the CubeSat. This may be solved by using the ADCS system on SPEAR to target each CubeSat individually for a set amount of time. Once that satellites maximum charge was reached SPEAR would move on to the next CubeSat. This may require a more robust ADCS system for SPEAR to conduct these movements, which may add mass increasing launch costs and complexity.

## 10.5 CubeSat Components

Each CubeSat that will be deployed from SPEAR will have a BOL mass of 7 kg. This consists of all key systems and a payload consisting of a camera, RF mass spectrometer, and lab-on-a-chip to test for chirality. A cross section view of the CubeSats expected configuration is visible in Figure 58. The main processing board consists of a Proton 200k Lite, which has a nominal operating power of 1.5W [77]. This board is also currently rated for 30 krad TID [77]. This will control the CubeSat as it orbits around Europa, process images for transmission, data from the Raman Mass Spectrometer, as well as the lab-on-a-chip. This chip has one of the highest TID ratings of any CubeSat computer.

The attitude determination and control system will consist of an XACT-15 ADCS system by Blue Canyon Technologies [78]. This system contains, reaction wheels, torque rods, inertial measurement units, magnetometer, star tracker, and sun sensors [78]. This system was considered ideal as it contains all of the necessary ADCS systems for this mission. Inclusion of the star tracker is important as these are the highest performing sensors available compared to traditional CubeSat attitude sensors [79]. Sun sensors and magnetometers only produce two angles of attitude data each, resulting in both being necessary to determine the three-axis spacecraft attitude. While Jupiter has a very strong magnetic field, a small magnetic field around Europa may exist because of its potential sub-surface ocean [20]. With this field still relatively unknown, a magnetometer may not provide the correct attitude information. The SPEAR CubeSats can use the sun sensor and star-tracker to find the spacecraft's attitude before the magnetic field characteristics are known. The XACT-15 system contains reaction wheel and magnetometers to control the attitude of the CubeSats. This low power system will allow the CubeSat to rapidly position itself for collecting science data and transmitting data back to SPEAR.

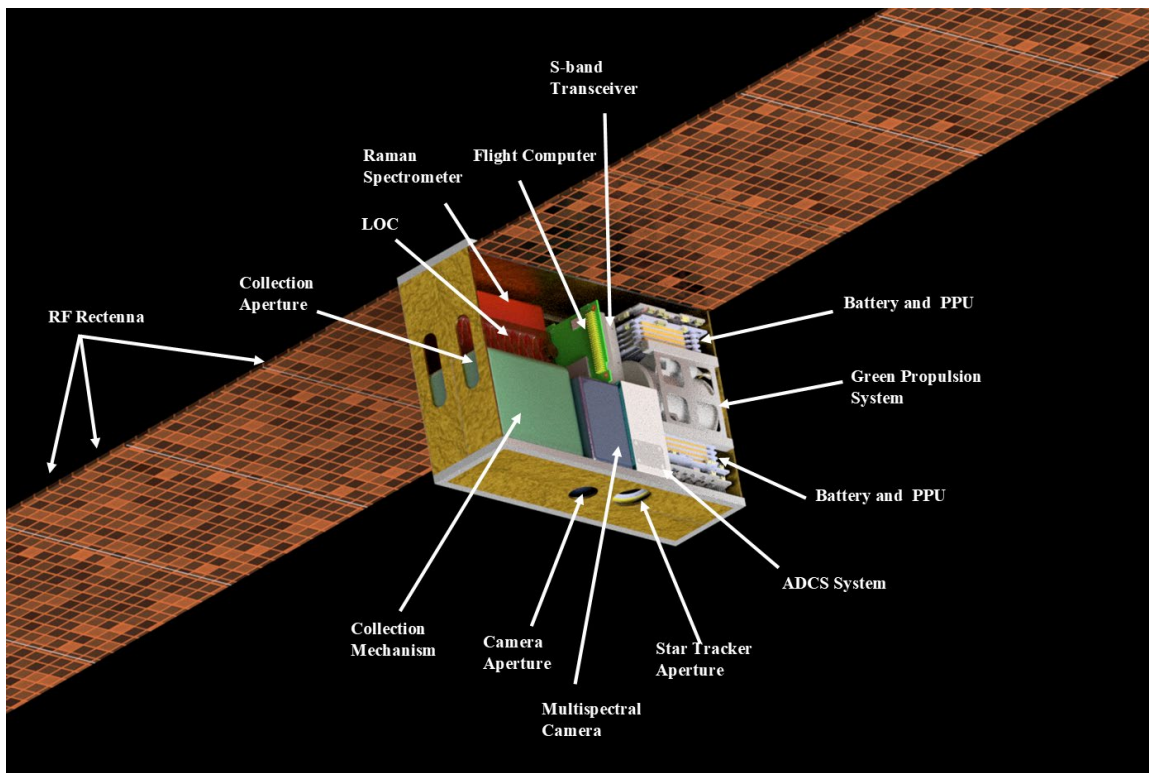


**Figure 58: Tentative CubeSat components to look for life at Europa. Each CubeSat includes all necessary components to operate in the Europa environment for 30 days. The payload includes a camera capable of multispectral and panchromatic images, Raman spectrometer, and a lab-on-a-chip with a chirality detector and microscope. Each CubeSat will communicate with the SPEAR mothership and be charged via RF coupling.**

To enter the desired orbit, the CubeSat is first ejected by the deployer. Then a propulsion system similar to the MPS-130 small sat propulsion system by Aerojet Rocketdyne [80] is used to accomplish the necessary inclination change maneuvers. This system uses AF-M315E green propellant [80] which is higher performing and less toxic than traditional hydrazine thrusters. This propulsion system is advantageous for several reasons including: increased propellant storage density, low freezing point of propellant, high specific impulse of the propellant [81]. This allows the CubeSats to reach a maximum delta-v of around 170 m/s to maneuver itself into a slightly separate orbit from SPEAR. This system does require the propellant and catalyst bed to be heated prior to firing the thrusters. However, this is only necessary during the very beginning of its orbit, which allows SPEAR to heat the propellant and the catalyst

bed prior to ejection. Leftover propellant can be used for orbit changing maneuvers, mission extensions, and end of life disposal.

As stated in the previous sections, the CubeSats will be powered via RF charging from the SPEAR Probe. This will be used in conjunction with the Starbuck-Nano [82] and the Optimus battery [83] from AAC Clyde Space. Currently, an 80 Wh battery, the Optimus-80, is used to power key systems within the CubeSat. The Starbuck-Nano will distribute and manage power within the spacecraft while communicating with the computer to anticipate future power requirements. The EPS system will take power from the RF rectenna and charge the battery. The charging rate of the battery is dependent on the charging profile, The Optimus-80 remains a place holder until charging profiles are finalized.

**Table 25: Predicted components utilized in the CubeSats that will be utilized to study Europa's environment and investigate for signs of life. Components are currently COTS to development costs and leverage heritage of systems that have been used for interplanetary CubeSats.**

Component	Mass (grams)	Power Minimum (Watts)	Power Maximum (Watts)	TID (krad)	Manufacturer	System
Proton 200k Lite	200 [77]	1.5 [77]	1.5 [77]	100 [77]	Space Micro	CD&H
XACT-15	910 [78]	Not Available	Not Available	Not Available	Blue Canyon Technologies	ADCS
S-Band Transceiver	190 [84]	4.5 [84]	13 [84]	10 [84]	IQ Spacecom	TT&C
S-Band Patch Antenna	49 [85]	4.5 [85]	13 [85]	Unknown	IQ Spacecom	TT&C
Starbuck-Nano	148 [82]	N/A	N/A	10 [82]	AAC Clyde Space	EPS
Optimus-80	650 [83]	N/A	N/A	Not Available	AAC Clyde Space	EPS
Rectenna Array	1354 (estimate)	N/A	N/A	Not Available	Composite Technology Development, Inc	EPS/Structures
MPS-130	1660 [80]	10 [80]	28 [80]	Not Available	Aerojet Rocketdyne	Propulsion
Structure	674 [86]	N/A	N/A	N/A	AAC Clyde Space	Structures
Gecko Imager	500 [87]	2.5 [87]	3.5 [87]	20 [87]	Space Advisory Company	Payload
Raman Spectrometer	650 [88]	1.25 [88]	3.75 [88]	Not Available	Anton Paar	Payload
Lab-on-a-chip	5 [89]	Not Available	Not Available	Not Available	Not Available	Payload
Total:	7000					

Each CubeSat will be equipped with a camera capable of panchromatic and multispectral images to capture high resolution images of Europa's surface. Leveraging remote sensing technologies from the NewSpace trend, these cameras are originally designed to provide high resolution images of the Earth. The Gecko Imager by SCS and Space Advisory Company can operate with four multispectral bands and in a panchromatic function to maximize the cameras scientific data potential [87]. With these spectra, each CubeSat will be able to identify specific attributes about the Europa environment. Similar to many of the instruments on the Europa Clipper mission these cameras will be used to detect plumes, investigate the atmosphere of Europa, collect high resolution geographic data and search for amino acids on the surface of Europa. Each camera at a 200 km altitude is predicted to have a 32km x 17km image swath with 15m/pixel resolution. As the altitude to the surface of Europa decreases, the swath size decreases as well as the pixel resolution of the surface. The camera is also radiation hardened to 20 krad from previous designs for use around Earth [87]. These cameras will be able to map out a significant portion of Europa's surface at much higher resolution than any previous mission or future mission planned.



One of the primary instruments onboard the CubeSat to analyze the plume particles is a Raman spectrometer. The compact size of this spectrometer makes it ideal to fit within the CubeSat. This will be used to identify components of the plume to detect for life sustaining compounds containing carbon, hydrogen, oxygen, nitrogen, phosphorous, and sulfur [89]. These elements have been found essential for all life on Earth [89] so the Raman spectrometer will primarily focus on these compounds and elements. Raman spectrometers can analyze the samples without significant sample preparation, are non-destructive, require small sample volumes of samples, and can complete analysis quickly [90]. These properties make it ideal to analyze the plume material, as its composition will be mostly unknown. The small sample sizes are also ideal, as the CubeSat may only intercept micrograms worth of material at a time.

SPEAR will have the complex challenge of communicating with the 10 satellites. Each CubeSat will be collecting a large amount of data from images as well as the Raman spectrometer, and lab-on-a-chip. To relay this information to SPEAR as quickly as possible during this short mission each CubeSat will be equipped with an s-band transceiver and s-band antenna. This will ensure a high data rate between SPEAR and its CubeSats. With the CubeSats expected to last only 30 days in Europa orbit they may not be able to transmit any stored data after this time frame. CubeSats could also communicate with each other to relay information quickly. Processing of all data will be performed on SPEAR to conserve power on the limited CubeSat platform.

Another instrumental piece of technology included on the CubeSats is a lab-on-a-chip (LOC). This revolutionary technology has been transforming how data is traditionally gathered. An entire process that would normally require bulky equipment and lengthy processing times can be miniaturized onto a small chip with high throughput capabilities [91]. Technology of this magnitude and small scale can greatly enhance space exploration and discovery as more experiments can be packed into smaller and lighter form factors including CubeSats. The LOC included on the CubeSats will consist of a microfluidic microscope and test for chirality [91]. As discussed in a later section, these will test and observe the material collected in the Europa plume for evidence of extraterrestrial life.

## 10.6 CubeSat Science Objectives

A variety of terrain exists on Europa, and of primary interest are the bands of ice that span its surface. These bands, believed to be caused material exchange between the surface of Europa and its ocean, are expected to contain material crucial to understanding Europa's ocean and the life it could possibly sustain [92]. These bands remain a prominent area to search for organic compounds and other minerals essential for life. Multi-spectral imaging can be used to determine the composition of many of these features from afar. Remote sensing satellites around Earth use multispectral imaging for a variety of applications. Several bands can be used to monitor different minerals, crops, algae blooms, and some thermal studies [93]. While it is unknown what type of life may exist on Europa, there is little evidence pointing to it being alive and visible on the surface. The wavelengths chosen for this mission include the include 55-210 nm [94], 300-1050nm [95], 0.8-5 $\mu$ m [96], and 7-70 $\mu$ m [97] to match that of the proposed Europa clipper mission (source). The 55-210 nm range will be used to determine the composition of Europa's surface in the UV spectrum [94]. In addition, this wavelength can also be used to characterize the atmosphere (if any) and investigate active plumes the CubeSat intercepts or sees from orbit. The 300-1050 nm range will be used to image the surface of Europa at high resolution receiving true color of the moon's surface [95]. The 0.8-5 $\mu$ m encompasses some of the near infrared range (NIR) and has been proven useful in the detection of some organic compounds necessary for life [96]. The final range 7-70 $\mu$ m within the infrared spectrum can be used to collect data on the temperature of the ice [97]. This can be useful to determine hot-spot locations with significant activity under the icy crust.

These images can provide a significant amount of scientific data about Europa's icy crust at a resolution previously unexperienced. This will help aid in the understanding of how Europa's ice sheet moves, the potentially composition of the ocean below the crust, and evidence showing minerals and compounds that can support life. High resolution geographical data will also be valuable for future missions to Europa that may support a lander. Images can be combined to make partial three-dimensional maps of the surface of Europa to better understand the ruggedness of the terrain. Thermal data from the CubeSats will also aid in determining the thickness of the ice. Both of these factors will be invaluable for future lander missions that wish to minimize landing risks and minimize the distance needed to reach the subsurface ocean if such a probe is attached for that application.

While the CubeSat cameras may only be able to identify compounds that support life, or detect materials that appear to be organic, they have no method to definitively prove there is life. The Raman spectrometer on each CubeSat will have the ability to analyze the compounds within the plumes to determine their composition. This will reveal a





multitude of information about the compounds and potentially life that exists underneath the surface of Europa. Raman spectroscopy is a powerful tool to determine chemical compositions of biological systems [98]. Raman spectrometers have also been shown to be useful in the analysis of extremophiles on Earth [99] [100] [101]. This is extremely valuable as life on Europa would most likely consist of extremophiles extracting energy from their environment in unique ways and living in an extreme environment [102]. In addition to the Raman spectrometer the lab-on-a-chip will be used to test the chirality of material obtained in the plume and observe it with a microscope.

Chirality is a useful test in the determination of life beyond Earth. Molecules, such as amino acids are chiral, meaning they are mirror images of each other [103]. Life on Earth consists of exclusively “left-handed” chiral amino acids and sugars [103]. Non-living compounds that contain amino acids contain equal parts “left” and “right” chiral molecules. This will be the primary method the CubeSats use to search for life on Europa. If left-handed amino acids are discovered this would provide strong evidence of life on Europa. Such a system has been developed on a small chip utilizing microfluidics [104] to perform the chiral separation. This small chip was capable of high throughput analysis in less than 90 seconds [104]. With a limited orbit lifetime around Europa, having high throughput of scientific data will be an invaluable resource. Flying through a plume may last only a few seconds, and only successfully occur with a few or single CubeSats. Additionally, the number of organisms living within the ice is unknown and the number of organisms per unit of material ejected may be very small [71]. If the density of living organisms brought up by the plume is in fact small, high throughput may be necessary to come across an organism. In addition to this, plume activity still remaining uncertain, it is possible that no plumes will be visible to SPEAR prior to ejection of the CubeSats. As a consequence of this a plume may never appear during the mission or appear in a different location than the CubeSats are able to move to. Recent studies have found water vapor within Europa’s atmosphere [69] after plume activity. If recent plume activity, or continuously suspended water vapor is present in the atmosphere, each CubeSat could have the opportunity to collect water vapor and other particles to test in the Raman spectrometer and lab-on-a-chip for chirality. Again, the high throughput of the chirality lab-on-a-chip will be able to process all the material during the mission.

Lab-on-a-chip technology has advanced rapidly, which is what has enabled the chirality experiments described above. In addition to this chirality experiment a microscope can also be used to examine the material collected from the plume. The purpose of this instrument is to observe the sample before its chirality is tested. This microfluidic microscope adds minimal mass to the CubeSat due to the advanced lab-on-a-chip technologies [105]. If microorganisms are observed with this microscope it will offer indisputable evidence of life on Europa. Smaller organisms such as bacteria and other extremophiles may be too small to be observable by the microscope, but still measure positive for “left-handed” chirality. Conversely, life on Europa may not have “left-handed” chirality but may be large enough to be visible within the microscope. Thus, each SPEAR CubeSat will contain three methods for determining presence of life or compounds that support life on Earth. The primary two being the Raman spectrometer and the lab-on-a-chip for chirality detection. The addition of a microscope on the lab-on-a-chip could offer the first image of extra-terrestrial life.

## 10.7 Sample Collection

Samples from the plumes must be collected in a safe manner so as not to damage the scientific equipment used to detect life. A significant advantage, discussed in the sections above, is the small sample size required for each of the instruments. Only a few micrograms are necessary to collect data for all of the instruments. Traveling at orbital speeds, the CubeSats must capture particles with a relative speed 1.34-1.41 km/s. Larger particles are dangerous because they can impart a significant amount of energy onto the CubeSat despite their small size. As shown Earlier CubeSats at lower altitudes will intercept larger particles and risk destruction, however, at higher altitudes smaller particles are much more prevalent, but particles impact per second decreases.

Even intercepting small particles could potentially damage the payload of the CubeSats; for this reason, a system utilizing aerogel will be used to capture these particles. This capture mechanism has been used previously on NASA’s Stardust mission to intercept comet material [106]. Aerogel is able to slow the particle down so it will not damage the spacecraft’s valuable components. This will also prevent the particles from disintegrating if they impact at a high enough velocity. The aerogel will be heated just enough to cause the particle to melt if made of water and condense onto the sample collection area. Some bacteria have been known to survive high velocity impacts at speeds of 5 km/s [107], however, the goal is not to necessarily capture these organisms alive, but to simply retain their organic





material for testing. Microorganisms can be transferred via evaporation and transfer of vapor from one location to another [108]. This will at least ensure that the microorganisms, dead or alive, can be transferred and condensed onto a sample plate so the life detecting instruments can operate without the risk of being damaged by particle and still can detect life.

The high throughput of the life detecting systems onboard the CubeSats are valuable as the biomass in Europa's ocean remains unknown. If organisms are present near the ice/water boundary between 0.1-1 liters of ice would need to be processed before a positive result was detected [71]. It is unknown how much material the CubeSats will be able to collect during its lifetime, but existing LOC technology had sensitivity levels on the parts per trillion range [104]. This will be extremely useful in the detection life with unknown amounts of organisms per kilogram of material. The high throughput of the LOC and Raman spectrometer would also aid in processing as much material as possible to increase the probability of detecting life.

## 11 COST COMPARISON AND ESTIMATION

Deep space missions have always been reserved for costly multi-million to billion-dollar programs. Meanwhile, development of space around Earth has taken a surprising turn. The NewSpace movement has prompted many companies to explore swarm of small satellites for remote sensing and communications. Smaller launch vehicles

**Table 27: Notable deep space missions with their associated launch vehicle and cost. Newer technologies and competition have pushed launch costs lower, yet they still remain high for more mass intensive spacecraft.**

Deep Space Probe	Launch Vehicle	Cost
Cassini	Titan IV	\$475 million [121]
Juno/ New Horizons	Atlas V 551	\$153 million [122]
Galileo	Space Shuttle Atlantis	\$450 million* [123]
Europa Clipper	Space Launch System	\$876 million** [124]

\*Average cost of a shuttle launch

\*\*Europa Clipper will potentially use the SLS as its launch vehicle which is currently estimated at \$2 billion which is subject to change.

**Table 26: Small-Medium launch vehicles and associated costs for a SPEAR launch.**

Launch vehicle	Maximum Payload to LEO	Launch Cost (dedicated)	\$/kg	SPEAR Launch Cost
Firefly Beta*	4,000 [126]	\$35 million [125]	\$8,750	\$13.27 million
Antares	6,600 [127]	\$80-85 million [127]	\$12,121-12,878	\$18.94 million
Minotaur IV	1,735 [129]	\$50 million [128]	\$28,818	\$43.69 million
Minotaur C†	1,458 [127]	\$40-45 million [127]	\$27,434-\$30,864	\$44.19 million
Epsilon†	1,200 [127]	\$39 million [127]	\$32,500	\$49.27 million
Vega	1,963 [127]	\$37 million [127]	\$18,848.7	\$28.57 million
Terran*†	1,250 [130]	\$10 million [130]	\$8,000	\$12.13 million
Rokot	2,150 [127]	\$41.8 million [127]	\$19,441	\$29.47 million
Dnepr	3,200 [127]	\$29 million [127]	\$9,062	\$13.74 million

\*Under development.

†Launch vehicle possible with improvements to SPEAR wet mass and trajectory.

and new commercial opportunities has driven down launch costs considerably. Private industries have also made their intentions known about commercializing the lunar economy as well. Modern technology is well suited to meet the needs of the expanding space economy. However, there is a significant lack of affordable technology for deep space

exploration. SPEAR aims to drastically reduce the costs of deep space missions by utilizing the revolutionary ATEGs and nano-reactor.

### 11.1 Launch Costs

The revolutionary power system allows SPEAR to have a low dry mass, and in the Europa mission scenario, a wet mass of 1,100 kg. With such a low mass it can potentially ride-share on larger launch vehicles such as a Falcon 9. With a launch cost of \$2,719/kg, as claimed by SpaceX [109], SPEAR could be launched for under \$4 million. SPEAR can be launched into virtually any orbit, limiting the need for it to be a primary payload on most missions. Table 27 shows the launch vehicle and associated launch cost for several notable deep space probes. It is clear from this table that SPEAR can be launched on a ride share mission for a fraction the cost of these larger deep space missions. SPEAR can also be launched on smaller launch vehicles as well if ride-shares are not available. Table 26 shows several small to medium class launch vehicles in production or slated for future launches. While these options are more expensive than a ride share, they are still fractions the cost of the larger launch vehicles used for the other probes.

The regulations behind a private company launching a reactor into space have been dictated through a presidential memorandum in August of 2019 [110]. This memorandum outlines methods of achieving launch approval for LEU fission reactors and includes wording which encourages reviewers to use heritage launch approval whenever possible- a fact which promotes the use of the SPEAR probe, as it can be used for a multitude of different missions. However, it does not list expected costs or fees. Cost estimates for this report rely largely on the assumption that the SPEAR probe will have been previously approved for launch and the agency review process is sufficient for private launch companies to avoid charging excess fees for launching the reactor.

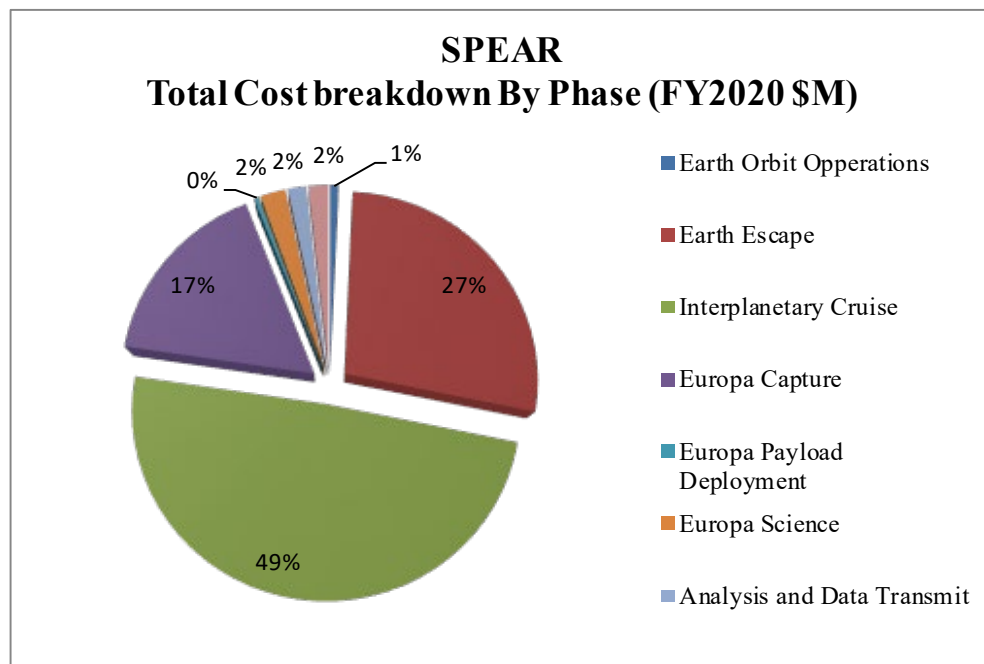


**Figure 59: Cost breakdown of a SPEAR mission to Europa. Most of the cost is dedicated to the phases where SPEAR is in a cruise phase in interplanetary space as well as around Earth and the Jovian system. Due to the relatively short mission life of the CubeSats the actual science collection portion of the mission contains very little of the actual mission cost.**

## 11.2 Operational Costs

Clearly, compared to larger missions SPEAR drastically reduces launch costs. A primary concern is also the operational costs associated with the SPEAR probe. With a long duration mission, the operational costs can add up quickly, especially during the cruise phase which produces minimal science data. Another phase that costs a significant amount is the orbital operations phase. In this phase SPEAR and the CubeSats will be collecting data about the Europa environment. Due to the extreme radiation environment this portion of the mission will consist of roughly 30 days. With a short duration science mission, the large costs normally associated with this phase are only applied over a short period of time, which further reduces mission costs. With the use of NASA's Mission Operations Cost Estimation Tool (MOCET) [111] the approximate cost of the SPEAR mission can be calculated for the different operational phases.

Costs for such a mission and technology available by the time a SPEAR mission can be conducted are largely

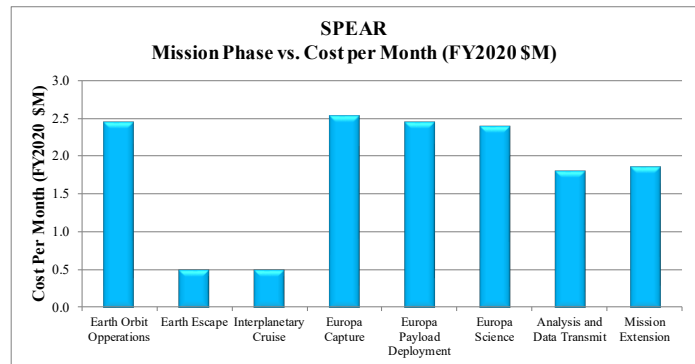


**Figure 60: Monthly costs of different SPEAR mission phases. While the interplanetary and Earth cruise phases may have the lowest costs. They are currently projected to last 5 and 10 years respectively.**

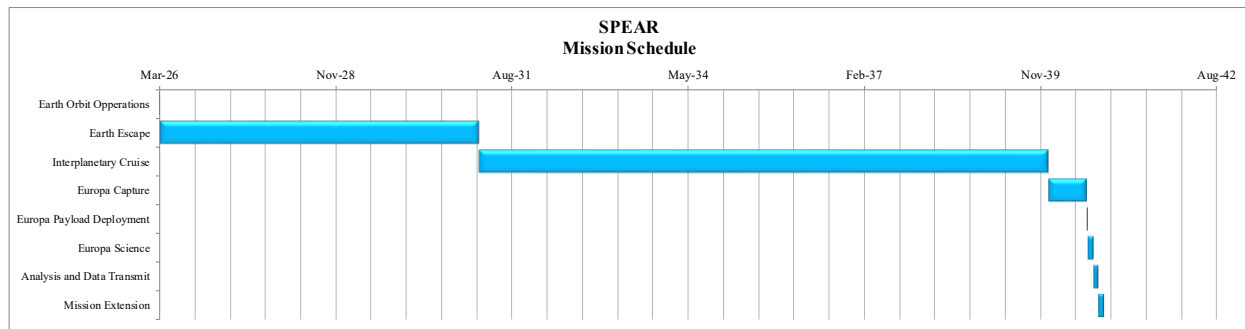


**Figure 61: An estimated SPEAR mission schedule based on an arbitrary launch data. Maneuvers and cruise phases consist of most of the mission with the science and data collection occurring at the end of the mission. A 30-day mission extension is estimated in this scenario and is subject to both SPEAR and the CubeSats survivability in the Europa environment. Reduction in mission length may be available via gravity assists and/or kick stages in Earth orbit.**

undetermined and may change predicted cost significantly. Utilizing the MOCET tool, the estimated operational cost for a SPEAR mission was calculated at \$109.13 million. The breakdown of this cost is visible in Figure 59. Most of the cost associated with this mission accumulates over long periods of interplanetary and planetary cruise phases. The actual science mission portion of the SPEAR mission only accounts for roughly 7% of the total operation costs. This is to be expected as each CubeSat is expected to survive roughly 30 days in orbit around Europa. Although the cruise periods around Earth and in interplanetary space have the lowest monthly costs, they are applied over long periods of time. Figure 60 shows the monthly cost of operating the SPEAR probe during its various phases. When more engineers, technicians, and operators are required, the monthly costs increase. Figure 61 shows an estimated timeline of the SPEAR mission. Clearly the cruise phase, Earth Escape, and Interplanetary Cruise make up the largest portion of the mission. Other phases such as Earth orbit operations, Europa Insertion, Europa Science, Analysis and Data Transmission, and Mission Extension have high monthly costs, but have phases that last only a few months or less. Methods need to be investigated to reduce the cost of these lengthier phases that return little in terms of science data but consist of the largest portion of the mission.

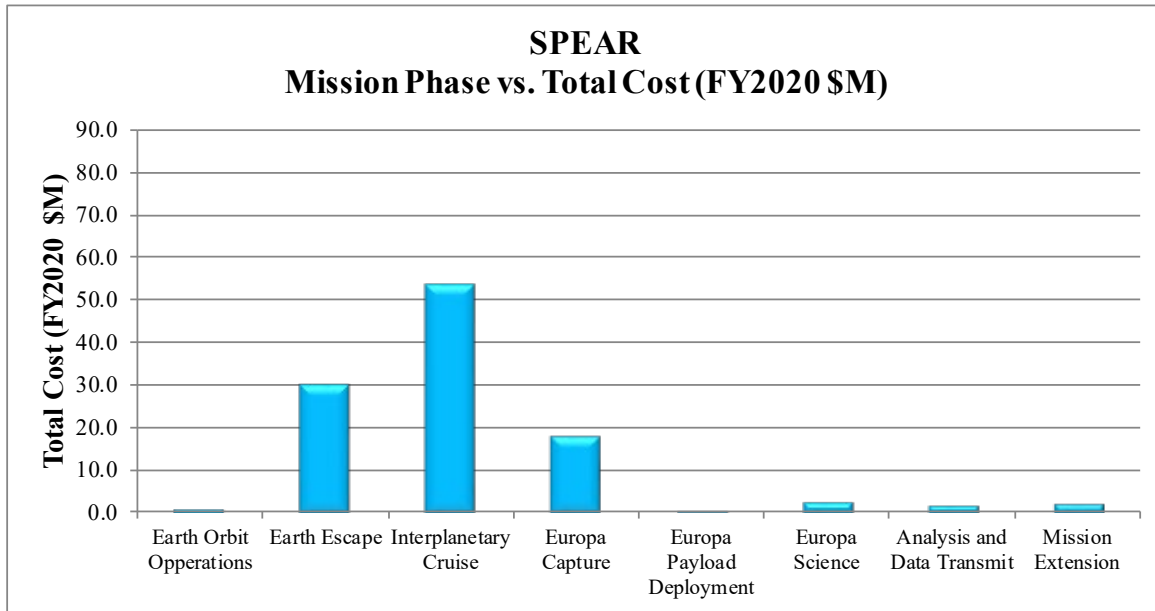


**Figure 62: Mission cost per phase of a predicted Europa mission. One can clearly see that the Earth escape and interplanetary cruise cost the most compared to other phases.**

A breakdown of the cost for each phase is visible in Figure 62. At over \$50 million for the interplanetary cruise and almost \$30 million for the Earth escape/cruise phase these portions of the mission are the costliest. The Europa capture phase was considered more expensive as this would theoretically involve monitoring of Europa, constant trajectory monitoring because of the complex Jovian system, as well as science data gathering on Europa and the Jovian system. Mission extensions can be applied for relatively inexpensive amounts; however, this is highly depending on the survivability of the SPEAR probe and the deployable CubeSats collecting data around Europa.

There are several methods that can be utilized to further reduce mission costs or increase science impacts during portions of the mission that would otherwise see no scientific benefit. During the cruise phase several instruments could be included to study the solar system while in transit to Europa. This will at least have a higher return of science data than a completely quiescent cruise phase. Lasers included within the SPEAR payload and CubeSat power system can be used for optical communication experiments. In addition to this the high gain antenna, magnetometer, and other environmental sensors can be used gathering gravity and other science data. If feasible, the high gain antenna may be useful as a radio telescope.

Seeing as this mission would be many years away in order to develop and test the power system there is bound to be many great advancements in technology. One such advancement that is quickly accelerating in its maturity is artificial intelligence (AI). Such a system could be used to control and optimize various aspects of SPEARS mission. This would include the autonomous navigation and control to Europa. If a trusted AI system can be used that makes corrections to its trajectory this could replace the need for teams on the ground to interpret data and send correction to the probe. This process could be very costly as there may be long periods of time where teams are paid to remain on standby and do nothing. An artificial intelligence computer could address minor anomalies in a timely manner and optimize the solution to keep SPEAR on track and ready to respond to any mission altering situations. With a large amount of power onboard the spacecraft, SPEAR could allocate resources to a more power intensive computer than previous missions could.

Another way to reduce operational costs would be to launch multiple SPEAR probes at a time. Instead of dedicated launches on small satellite launch vehicles, a single dedicated launch of large-heavy lift launch vehicle could be used to send multiple SPEAR probes at a time. These probes would benefit from using the deep space network at the same time and utilizing the same operations team. Instead of launching multiple missions into deep space at different times with different mission phases overlapping, a single launch could send numerous probes all with similar mission phases reducing the overall costs compared to individual launches. This would make production of the spacecraft and its components less expensive as multiple components would be created at a time.

The last method to reduce trip time would be to include a kick stage or perform gravity assists and other orbital maneuvers that would reduce the total trip time or the amount of xenon propellant. While xenon propellant is currently in use due to its high specific impulse, other cheaper propellants could be used such as iodine, krypton, and argon. Iodine could be a suitable replacement if the cost of xenon is large enough to outweigh launch costs. The addition of a kick stage has the added benefit of reducing trip time and the volume of xenon propellant required. Reducing trip time can significantly reduce the cruise time as this is when most of the cost is accumulated with no scientific output.

### 11.3 Reactor and Exotic Material Costs

There are several key material costs that arise when looking at the various components of SPEAR. The uranium used on the SPEAR probe needs to be enriched to 19.75% in order to be classified as low enriched uranium, or LEU. In order to enrich the expected 76.36 kg of uranium, the reactor would require 2,921 kg of feed material with a total of 3444 separate work units (SWU) to enrich the uranium. At a price of \$60/kg per SWU [112]; SPEAR's reactor fuel could be enriched for \$206,640. This is dependent on the feed stock enrichment and the current SWU price at the time of enrichment. Currently non-enriched uranium costs roughly \$38.81/lb. (\$85.56/kg) [112], which means spears would require roughly \$249,923 worth of uranium.

The reactor itself will be made from beryllium, lithium hydride, mercury heat pipes, and a single boron control rod. This system, as well as the ATEG power conversion system, is expected to require the most significant research and development costs. Material costs for the reactor have been outlined in Table 28. The greatest costs involved with the reactor involve the enrichment of the uranium as well as the bulk material cost of uranium. The lightweight nature of the reactor minimizes the more costly elements needed for fission such as beryllium, boron, and lithium hydride. This price estimate does not include the housing of the reactor, actuators, and other mechanisms necessary to control the fission process.

Estimating the cost of the ATEGs is a more difficult task as more research needs to be conducted into the performance of these materials as a function of isotope loading. The cost for these materials can also range drastically especially when looking at the rare Earth borides. With the isotope radiation sources, the price depends significantly on the infill percentage. The advantage of the ATEGs is that the amount of raw foot material required is very small. Table 29 shows a rough estimation of the ATEG cost for an entire SPEAR vehicle. This produces 3 kW of electrical power and represents only the bulk ATEG feet material not including conductors and insulators typically seen on TEGs.

It is clear from Table 29 how much ATEG with isotope dopants can cost. The price to mix boron into the ATEGs is drastically lower. While these systems all use the same volume percentage, the density of americium and plutonium are much higher than boron. It is important to note that these are the prices of only the dopant. The price of the raw foot material will be different and can vary significantly as well. If proven successful, potentially inexpensive thermoelectric feet or materials such as those discussed in the ATEG section can see drastic improvements in their efficiency. It may be possible for some rare Earth borides to achieve high efficiency levels without the need for a boron or isotope additive, as the ionizing material will be already be distributed in the foot material. However, these units may or may not be more expensive and difficult to manufacture. Continuing research is necessary to perform studies on different materials for optimizing the ATEG performance.

**Table 28: Raw reactor materials with their associated costs. Uranium enrichment costs to 19.75% has been predicted. Enrichment and raw uranium costs comprise of the most significant costs for this reactor. This estimation includes structures and mechanisms needed to control the reactor, but not minor mechanical components.**

Reactor Materials	Price	Estimated Cost (2019)
Uranium Enrichment	\$60/SWU [112]	\$206,640
Uranium	\$85.56/kg [112]	\$249,923
Lithium Hydride	\$902/kg [131]	\$6,142
Beryllium	\$981/kg [132]	\$50,629
Mercury	\$264/kg [133]	\$1,980
Boron	\$5,520/kg [134]	\$386.4
	Total:	\$515,700.4

There may also be several methods to reduce the amount of isotope required to achieve the high levels of efficiency that have been modeled. Decreasing the particle size will be extremely helpful as the isotope can be finely distributed amongst the ATEG foot. This may increase complexity when fabricating feet in order to accurately produce properly mixed feedstock. Additionally, layers or positionally dependent loading may increase performance as well. Depending on the effects of the radioactivity, this may require significantly smaller amounts of isotope and approach levels much more economically feasible for mass production. Generally speaking, the lower the volume percent of isotope required the less expensive the entire system becomes.

**Table 29: ATEG dopant materials with a PbTe foot with 7 vol% infill. These ATEGs can be estimated to reach more than 30% efficiency at SPEAR's operating temperatures. There are significant differences between the dopants with 10B costing the least and 239Pu costing the most. It is significantly advantageous to use 10B with the reactor to reduce costs, but it should be noted 10B can only be used in conjunction with a neutron source. It should be noted that these ATEGs have not been designed to match a specific voltage and current.**

PbTe ATEG	Am	Pu	B
Infill	7%	7%	7%
Particle Size	5 microns	5 microns	5 microns
Efficiency	30.5%	36.3%	30.1%.
Mass of ATEG feet	203 grams	44 grams	191 grams
Cost of Dopant	\$1,500/gram [135]	\$4,000/gram [136]	\$19.75/gram [137]
Mass of Dopant	20.23 grams	6.73 grams	4.04 grams
Cost of Dopant	\$30,345	\$26,920	\$80

One of the other major costs associated with the SPEAR mission is the amount of xenon propellant required for the journey to Europa. With the current trajectory and mass of SPEAR the estimated mass of xenon would be 804.3 kg. Xenon was chosen with the NEXT thruster because of its extremely high specific impulse. With a price estimate of xenon of around \$850/kg [113], the total cost of propellant for the SPEAR system would be \$683,655. Reduction in this price is possible either through reducing the mass of the SPEAR system, therefore reducing the required mass of propellant, or switching to a less costly, but more inefficient propellant such as krypton, argon, or iodine. These propellants would increase the mass of SPEAR due to the lower specific impulse which would in turn increase the launch costs, which are projected to be much greater than \$850/kg. Launch costs would need to drop significantly to make it feasible to switch to another propellant at this point.

#### 11.4 Development Costs

A rough order of magnitude was determined for each subsystem based on the current mass model to predict development costs for a full SPEAR unit. Unmanned Space Vehicle Cost Model (USCM8) was used to estimate the cost of the SPEAR spacecraft development and production [114]. These estimations showed that development and the production of the theoretical first unit (TFU) could be produced for roughly \$108 million. Other estimation with the QuickCost estimator by NASA [114] shows a potential development and production of a TFU within \$241 million. These numbers are subject to change and could vary significantly by the time SPEAR is ready for its mission. Once developed, the cost for creating new SPEAR units is reduced to the operational manhours for engineers and technicians to continue to build units. A cost model was assembled for a steady state operational scenario and includes estimates for personnel, NRC fees, administration, and materials. Assuming that one SPEAR unit is built per year, the total cost per unit becomes ~\$5M.

There are many aspects of the SPEAR concept which can potentially reduce the cost below that of the cost prediction tools. Three major costs associated with the SPEAR program are: operation, development, and launch. The operational costs, as seen above, can be modeled through a number of tools and predictive methods, and is expected to reach ~\$109M. However, this is based on costing tools based on previous missions which include manhours of NASA employees. Private entities (or on-board AI) may be able to significantly decrease this cost. Development will cost roughly \$100M-\$240M but will be a one-time cost. Steady state production is expected to cost on the order of





\$5M for building new units. Launch costs range from \$8.8M to \$35M for a spear unit, and although new private launch companies claim to be bringing the price down, it is unreliable to use those claims for predictions. Thus, the cost of a SPEAR launch may vary from \$360M for the initial launch to nearly \$14M per launch in a continuous mode.

Even if a mission were launched as soon as possible, the total cost of a SPEAR mission including development, launch costs, and mission operations would be expected to cost between \$227.6 million to \$360.6 million. These development and production costs are still extremely low compared to other deep space missions and their launch costs. Even with the higher end estimates, SPEAR is set to challenge current limitations on deep space exploration with its innovative design and advanced power system.

## 12 CONCLUSIONS AND FUTURE WORK

This Phase I study has shown the potential for SPEARs success as a deep space probe. Its ATEG power conversion system would truly revolutionize deep space exploration. Howe Industries has shown through testing of BN that RIC effects are visible in materials containing  $^{10}\text{B}(\text{n},\alpha)$  particles. A variety of materials have been identified that can be easily tested in a neutron environment to validate their ATEG potential. Work in a Phase II study could accomplish this material sweep which would further validate models, and provide the optimal material to create a  $^{10}\text{B}(\text{n},\alpha)$  based ATEG. This will also spur investigations into radioisotope based ATEGs and their ability to increase the efficiency of thermoelectric generators without the need for a neutron field. Howe Industries is confident that in the second year of a Phase II award, a working ATEG prototype could be tested in neutron environment. The success of such a test would validate the feasibility of the ATEG system without a doubt. Howe Industries will partner again with Atomos Space to demonstrate how our ATEG system could benefit their space-based power systems. In Phase II the Howe Industries team will work with a new partner, Zeno Power Systems, to demonstrate how the ATEG power conversion system can benefit terrestrial based power sources.

Throughout this study refinements have been made to the overall design of the SPEAR probe. It remains a capable spacecraft with the ability to deploy a CubeSat swarm in the search for life within the plumes of Europa. The mass of the system has grown since initial estimates, but spear remains a low mass system capable of launching on numerous small to medium class launch vehicles. With the help of Atomos Space and The Hypershield Partnership several methods have been identified to reduce the mass of the probe to reduce launch costs and decrease mission lifetimes. In a Phase II study Atomos Space will conduct studies to optimize SPEAR's trajectory to Europa, and from when it enters the Jovian system to Europa. They will minimize flight times as well as propellant mass with optimized gravitational assists from various celestial bodies.

The nano-reactor on board SPEAR has been shown through numerical analysis to reach criticality with a low mass reactor. Phase II will see further investigations into the nano-reactor to reduce the total dose exhibited by the vital components controlling the CubeSats and the SPEAR probe. Howe Industries has investigated the radiation environments SPEAR will experience, but further investigations will be conducted to determine material degradation due to GCR, the ATEG dopant, and neutron field to determine system degradation with time.

Howe Industries has outlined how a swarm of CubeSats at Europa could analyze ejecta from Europa's plume with advanced LOC technologies. Difficulties in powering these CubeSats have been outlined, and Howe Industries will continue to investigate more efficient methods to power CubeSats throughout their mission.

The unique power system for SPEAR has applications that are much more far reaching than just this Europa mission. The ATEG technology alone has the potential to revolutionize solid state energy harvesting for space missions and terrestrial operations. Missions that traditionally relied on RTGs and applied the ATEG technology would have significantly more power for scientific instruments increasing their exploration potential. The Kilopower reactor which is projected to produce 1-3 kWe has a current mass of 400 kg. The nano-reactor included on SPEAR can produce the same amount of power with a mass of only 134 kg. This can either reduce launch costs or reserve more mass of payload and other important science data. With no moving parts, save for the control rod mechanisms, the SPEAR reactor can operate without fear of mechanical failure due to wear and tear on the power generating systems.

Terrestrially, the SPEAR reactor and ATEGs have boundless potential. The ATEGs can be used for waste heat recovery on virtually any system that were a heat gradient is present. This could significantly increase the energy production capabilities of traditional power generation methods. It is estimated that by the year 2025 the thermoelectric



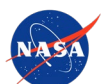
generator market will be worth \$741 million [115]. The nano-reactors could be used on Earth to provide power in areas that have limited infrastructure or in response to a natural disaster. The compact size of the reactors allows for multi-kilowatt power systems to be readily available and easily transported.

Various technologies requiring a Peltier Cooler, which creates a temperature differential between two thermoelectric couples using a power input, would also benefit from the ATEG technology. A more efficient Peltier cooler with the ATEG technology would require significantly less power to achieve the same performance. This would be extremely useful for applications that are power limited and require a rugged system that would not be prone to failure because of mechanical issues. In spacecraft this would be especially important as some computers, sensors, and systems need to be cooled. On Earth these efficient Peltier Coolers could be used for any system requiring highly efficient cooling that would require little to no maintenance and limited failure potential.

The technologies and situations described above mostly focus on the reactor alone, but there are numerous benefits that the SPEAR craft can have for private companies and NASA. With a high delta-v capability, and significantly low launch cost the SPEAR probe can deliver 70 kg of payload to virtually any location within reason. SPEAR opens deep space to NASA and other private companies for a relatively low price. The Europa mission described above shows a \$3.25 million to \$5.15 million per kilogram of payload to Europa. But once the SPEAR craft becomes widely used, the cost will approach just over \$200k/kg. Private companies could use SPEAR to deliver CubeSats or other 70 kg payloads to various locations in deep space for future business purposes. With the industrialization of space rapidly occurring it is only a matter of time before more private companies move to develop deep space for applications such as asteroid mining, communications, or data gathering. SPEAR can be used to explore areas of interest, deploy CubeSats, or test technologies in deep space for companies before they invest in the development of a complex space economy. SPEAR combines several groundbreaking technologies that will set in motion the availability and development of deep space as well as revolutionize terrestrial power production.

### 13 REFERENCES

- [1] Lockheed Martin, "Juno," [Online]. Available: <https://www.lockheedmartin.com/en-us/products/juno.html#mission-overview>.
- [2] National Research Council, Vision and Voyages for Planetary Science in the Decade 2013-2022, 2011.
- [3] Jet Propulsion Laboratory, "Europa Clipper," [Online]. Available: <https://www.jpl.nasa.gov/missions/europa-clipper/>.
- [4] K. Northon, "NASA's Hubble SPots Possible Water Plumes Erupting on Jupiter's Moon Europa," *NASA*, Vols. Release 16-096, 2016.
- [5] S. Potter, "Old Data Reveal New Evidence of Europa Plumes," *NASA*, Vols. Release 18-034, 2018.
- [6] L. Paganini, G. L. Villanueva, L. Roth, A. M. Mandell, T. A. Hurford, K. D. Retherford and M. J. Mumma, "A measurement of water vapour amid a largely quiescent environment on Europa," *Nature Astronomy*, 2019.
- [7] R. Mukai, D. Hansen, A. Mittskus, J. Taylor and M. Danos, "Juno Telecommunications," *DESCANSO Design and Performance Summary Series*, vol. 16, 2012.
- [8] J. Taylor, L. Sakamoto and C.-J. Wong, "Cassini Orbiter/Huygens Probe Telecommunications," *DESCANSO Design and Performance Summary Series*, vol. 3, 2002.
- [9] L. Mason, "A Power Conversion Concept for the Jupiter Icy Moons Orbiter," *First International Energy Conversion Engineering Conference*, 2003.
- [10] W. A. Hoskins, R. S. Aadland, N. J. Meckel, L. A. Talerico and J. M. Monheiser, "NEXT Ion Propulsion System Production Readiness," *Joint Propulsion Conference & Exhibit*, 2007.
- [11] National Aeronautics and Space Administration, "Juno Launch Press Kit," 2011.
- [12] BAE Systems, "RAD750 family of radiation-hardened products," BAE Systems, Manassas, Virginia.



- [13] Malin SPace Science Systems, "Junocam, Juno Jupiter Orbiter".
- [14] W. A. Hoskins, R. S. Aadland, N. J. Meckel, L. A. Talerico and J. M. Monheiser, "NEXT Ion Propulsion System Production Readiness," in *43rd AIAA/ASME/SAE/ASEE Joint Propulsion Conference & Exhibit*, Cincinnati, OH, 2007.
- [15] Aerojet Rocketdyne, "MSTI-3 Propulsion Module," 13 9 2019. [Online]. Available: <https://www.rocket.com/space/space-power-propulsion/monopropellant-rocket-engines>.
- [16] Blue Canyon Technologies, "Reaction Wheels RW8," [Online]. Available: <https://www.bluecanyontech.com/components>.
- [17] Blue Canyon Technologies, "Standard NST," [Online]. Available: [https://storage.googleapis.com/blue-canyon-tech-news/1/2019/07/BCT\\_DataSheet\\_Components\\_StarTrackers\\_F2.pdf](https://storage.googleapis.com/blue-canyon-tech-news/1/2019/07/BCT_DataSheet_Components_StarTrackers_F2.pdf).
- [18] Rocket Lab, "Rocket Lab Rideshare CubeSat Launch in Maxwell," in *CubeSat Developers Workshop*, 2018.
- [19] Planetary Systems Corporation, "Canisterized Satellite Dispenser," [Online]. Available: <https://www.planetarysystemscorp.com/product/canisterized-satellite-dispenser/>.
- [20] R. Pappalardo, B. Cooke, B. Goldstein, D. Senske and T. Magner, "The Europa Clipper OPAG Update," JPL, John Hopkins University, 2013.
- [21] S. M. Qadri and I. M. Abdel-Motaleb, "Thermoelectric Devices: Principles and Future Trends," Department of Electrical Engineering, Dekalb, IL.
- [22] J. F. Zakrajsek, "OPAG Technology Forum," Radioisotope Power Systems Program, 2018.
- [23] C. Vining, "An inconvenient truth about thermoelectrics," *Nature Mater*, vol. 8, pp. 83-85, 2009.
- [24] T. Shikama, S. J. Zinkle and S. Yamamoto, "Electrical properties of ceramics during reactor irradiation," *Journal of Nuclear materials*, Vols. 258-263, pp. 1867-1872, 1998.
- [25] S. J. Zinkle and L. K. Mansur, "Radiation Effects in Materials, with Emphasis on INsulators for Couplers," Oak Ridge National Laboratory, 2002.
- [26] C. Subramanian, A. K. Suri and T. Murthy, "Development of Boron-based materials for nuclear applications," *Bhabha Atomic Research Centre*, no. 313, April 2010.
- [27] R. F. Barth, H. G. H. Vicente, J. A. Coderre and T. E. Blue, "Boron Neutron Capture Therapy of Cancer: Current Status and Future Prospects," *Clinical Cancer Research*, vol. 11, no. 11, pp. 3987-4002, 2005.
- [28] M. Niffenegger and et. al., "The change of the Seebeck coefficient due to neutron irradiation and thermal fatigue of nuclear reactor pressure vessel steel and its application to the monitoring of material degradation," Paul Scherrer Institute , Switzerland, 2002.
- [29] S. Zinkle and E. Hodgson, "Radiation-induced changes in the physical properties of ceramic materials," *Journal of Nuclear Materials* , Vols. 191-194, pp. 58-66.
- [30] H. Lee, "Thermoelectric Generators," in *Thermoelectrics: Design and Materials*, John Wiley & Sons Ltd, 2017, pp. 8-22.
- [31] J. Nakamura and A. Akaishi, "Anomalous enhancement of Seebeck coefficients of the graphene/hexagonal boron nitride composites," *Japanese Journal of Applied Physics*, vol. 55, no. 1102A9, pp. 1-9, 2016.
- [32] L. A. Algharagholy, Q. Al-Galiby, H. A. Marhoon, H. Sadeghi, H. M. Abduljalil and C. J. Lambert, "Tuning thermoelectric properties of graphene/boron nitride heterostructures," *Nanotechnology*, vol. 26, 2015.
- [33] Z. Zhou, H. Liu, D. Fan and G. Cao, "Designing graphene/hexagonal boron nitride superlattice monolayer with high thermoelectric performance," 2019.
- [34] L. A. Algharagholy and a. et., "Tuning thermoelectric properties of graphene/boron nitride heterostructures," *Nanotechnology*, vol. 26, no. 47, 2015.
- [35] Y. Ouyang , Y. Xie, Z. Zhang, Q. Peng and Y. Chen, "Very high thermoelectric figure of merit found in hybrid transition-metal-dichalcogenides," *Journal of Applied Physics*, no. 120, 2016.

- [36] S. Miura, H. Sasaki, K.-i. Takagi and T. Fujima, "Effect of varying mixture ratio of raw material powders on the thermoelectric properties of AlMgB14-based materials prepared by spark plasma sintering," *Journal of Physics and Chemistry in Solids*, vol. 75, no. 8, 2014.
- [37] T. Mori, "High Temperature Boron-based Thermoelectric Materials," *material Matters*, vol. 4, no. 2, 2011.
- [38] T. Mori, "High temperature thermoelectric properties of B12 icosahedral cluster-containing rare earth boride crystals," *Journal of Applied Physics*, 2005.
- [39] A. Sussardi and a. et, "Enhanced thermoelectric properties of samarium boride," *Journal of Materiomics*, vol. 1, pp. 196-204, 2015.
- [40] Department of Energy, "Nuclear Materials Control and Accountability," *DOE Standard DOE-STD-1194-2011*.
- [41] D. I. Poston and P. R. McClure, "White Paper-Use of LEU for a Space Reactor," Los Alamos National Laboratory, 2017.
- [42] Marshall Space Flight Center, "Space Technology Game Changing Development Nuclear Thermal Propulsion (NTP)," NASA.
- [43] P. M. Huerta, "A review of the cold neutron moderator materials: neutronic performance and radiation effects," *Physics Procedia*, vol. 60, no. 74-82.
- [44] MatWeb, "Graphite, Carbon, C," 3 11 2016. [Online]. Available: <http://matweb.com/search/DataSheet.aspx?MatGUID=3f64b985402445c0a5af911135909344&ckck=1>.
- [45] MatWeb, "Lithium Hydride, LiH," 3 11 2016. [Online]. Available: <http://matweb.com/search/DataSheet.aspx?MatGUID=b0f308c749af4598b3c776a75c4afe75>.
- [46] E. Roussos, "THE IN-SITU EXPLORATION OF JUPITER'S RADIATION BELTS," Goettingen, Germany.
- [47] W. K. Tobiska, "Radiation Belts," in *Space Mission Engineering: The New SMAD*, Hawthorn, CA, Microcosm Press, 2011, pp. 136-137.
- [48] D. A. Adams, L. W. Howell and J. H. Adams, "On the use of Linear Energy Measurements to Estimate Linear Energy Transfer Spectra," NASA Marshall Space Flight Center, 2007.
- [49] A. Seppala and a. et, "Atmospheric impact of the Carrington event solar protons," *Journal of Geophysical Research Atmospheres*, 2008.
- [50] NASA, "Setting up Juno's Radiation Vault," 2010.
- [51] D. A. Herman, "NASA's Evolutionary Xenon Thruster (NEXT) Project Qualification Propellant Throughput Milestone: Performance, Erosion, and Thruster Service Life Prediction After 450kg," Glenn Research Center, Cleveland, OH, 2010.
- [52] Busek Co. Inc, "Hall Effect Thrusters," 2019. [Online]. Available: [http://busek.com/technologies\\_\\_hall.htm](http://busek.com/technologies__hall.htm).
- [53] G. Herdrich, "Magnetoplasmadynamic Thrusters," 2018.
- [54] Princeton, "Lorentz Force Accelerators (LFAs)," 2019. [Online]. Available: <https://alfven.princeton.edu/research/lfa>.
- [55] Apollo Fusion, "Apollo Constellation Engine (ACE)," 2019. [Online]. Available: <https://apollofusion.com/ace.html>.
- [56] M. A. Gibson, M. S. Lee, C. L. Bowman, D. I. Poston, P. R. McClure, J. Creasy and C. Robinson, "Development of NASA's Small Fission Power System for Science and Human Exploration," NASA, 2015.
- [57] S. L. Rickman, "Introduction to On-Orbit Thermal Environments," in *Thermal and Fluids Analysis Workshop*, Cleveland, Ohio, 2014.
- [58] Incropera, DeWitt, Bergman and Lavine, "Introduction to Heat Transfer 5th Ed.," John Wiley & Sons, Inc, 2007.
- [59] B. Muzyka and J. Weyant, "Heat Pipe Design and Modeling," Advanced Cooling Technologies Inc., 2015.



- [60] Ritt, Peter and D. Reist, "Heat Pipe Solutions for LED Devices," Tech Briefs, 2018.
- [61] Abadneh and a. et, "Thermal-Fluid Modeling for High Temperature Conductivity Heat Pipe Thermal Ground Planes," *Journal of Thermophysics & Heat Transfer*, 2014.
- [62] D. G. Gilmore and M. Donabedian, "Spacecraft Thermal Control Handbook, Appendix A: Surface Optical Property Data," *American Institute of Aeronautics and Astronautics*, 2003.
- [63] L. Kauder, "Spacecraft Thermal Control Coatings References," *Goddard Space Flight Center, NASA*, Vols. NASA/TP-2005-212792.
- [64] J. Foust, "Industry remains optimistic about continued growth of cubesats," 2016. [Online]. Available: <https://spacenews.com/industry-remains-optimistic-about-continued-growth-of-cubesats/>.
- [65] D. Leone, "In NASA First, Cubesats Headed to Mars with InSight Lander," 2015. [Online]. Available: <https://spacenews.com/in-nasa-first-cubesats-headed-to-mars-with-insight-lander/>.
- [66] W. S. Kiefer, "Europa and Titan: Oceans in the Outer Solar System?," Lunar and Planetary Institute.
- [67] S. Vance, W. Patterson, M. McGrath, K. Retherford, T. Hurford and B. Pappalardo, "Europa Plume Advisory Meeting Report," Lunar and Planetary Institute, 2014.
- [68] NASA, "Hubble Spots Possible Venting Activity on Europa," <https://hubblesite.org/contents/news-releases/2017/news-2017-17.html>, 2017.
- [69] NASA, "NASA Scientists Confirm Water Vapor on Europa," <https://www.nasa.gov/feature/goddard/2019/nasa-scientists-confirm-water-vapor-on-europa>, 2019.
- [70] B. S. Southworth, S. Kempf and J. Schmidt, "Modeling Europa's dust plumes," *Geophysical Research Letters*, vol. 42, pp. 10541-10548, 2015.
- [71] C. F. Chyba and C. B. Phillips, "Possible ecosystems and the search for life on Europa," *Proceedings of the National Academy of Sciences of the United States of America*, vol. 98, no. 3, pp. 801-804, 2001.
- [72] D. R. Williams, "Jupiter Fact Sheet," NSSDCA, Greenbelt, MD, 2018.
- [73] R. S. Bokulic and C. C. DeBoy, "21.1.4 Preliminary Link Analysis and Modulation/Coding Tradeoffs," in *Space Mission Engineering: The New SMAD*, Hawthorn, CA, Microcosm Press, 2011, pp. 630-634.
- [74] K. Chaurasiya and S. Kumar, "Design and Analysis of Parabolic Reflector Using MATLAB," *International Journal of Advanced Research in Electrical, Electronics and Instrumentation Engineering*, vol. 4, no. 3, pp. 1367-1373, 2015.
- [75] A. Behl, A. Bhatia and A. Puri, "Parabolic Antennas And Its Applications," *IJIRT*, vol. 1, no. 6, pp. 2117-2121, 2014.
- [76] D. Staelin, "MIT Open Courseware," 2003. [Online]. Available: <https://ocw.mit.edu/courses/electrical-engineering-and-computer-science/6-661-receivers-antennas-and-signals-spring-2003/readings/ch3new.pdf>.
- [77] Space Micro, "Space Micro," 9 4 2015. [Online]. Available: <http://www.spacemicro.com/assets/datasheets/digital/slices/proton200k-dsp.pdf>.
- [78] Blue Canyon Technologies, [Online]. Available: <https://bluecanyontech.com/components>.
- [79] J. Enright, D. Sinclair, C. Grant, G. McVittie and T. Dzamba, "Towards Star Tracker Only Attitude Estimation," *AIAA conference on Small Satellites*.
- [80] Aerojet Rocketdyne, "Modular Propulsion Systems Overview," [Online]. Available: <https://www.rocket.com/sites/default/files/documents/CubeSat%20Mod%20Prop-2sided.pdf>.
- [81] NASA, "Green Propellant Infusion Mission (GPIM) Overview," [Online]. Available: [https://www.nasa.gov/mission\\_pages/tdm/green/overview.html](https://www.nasa.gov/mission_pages/tdm/green/overview.html).
- [82] AAC Clyde Space, "EPS," [Online]. Available: <https://www.aac-clyde.space/satellite-bits/eps>.
- [83] AAC Clyde Space, "Batteries," [Online]. Available: <https://www.aac-clyde.space/satellite-bits/batteries>.
- [84] IQ Spacecom, "SLink," [Online]. Available: <https://www.iq-spacecom.com/products/slink>.



- [85] IQ Spacecom, "Antennas Patch antennas for Cubesats," [Online]. Available: <https://www.iq-spacecom.com/products/antennas>.
- [86] AAC Clyde Space, "Structures," [Online]. Available: <https://www.aac-clyde.space/satellite-bits/structures>.
- [87] Space Advisory Company, "Geck Imager," [Online]. Available: <http://www.spaceadvisory.com/products/payloads/gecko-imager/>.
- [88] Anton Paar, "Handheld Raman spectrometer: Cora 100," [Online]. Available: <https://www.anton-paar.com/us-en/products/details/handheld-raman-spectrometer-cora-100/>.
- [89] B. Streetman, "Exploration Architecture with Quantum Inertial Gravimetry and In-situ ChipSat Sensors," 2015.
- [90] University of Cambridge, "Raman Spectroscopy: Advantages and disadvantages," [Online]. Available: [http://web.archive.org/web/20120428151001/http://www.doitpoms.ac.uk/tlplib/raman/advantages\\_disadvantages.php](http://web.archive.org/web/20120428151001/http://www.doitpoms.ac.uk/tlplib/raman/advantages_disadvantages.php).
- [91] S. Nagl and a. et. , "Microfluidic chips for chirality exploration," *Analytical Chemistry*, vol. 83, pp. 3232-3238, 2011.
- [92] S. H. Howell and R. T. Pappalardo, "BAnd Formation and Ocean-Surface Interaction on Europa and Ganymede," *Geophysical Research Letters*, 2018.
- [93] Canada Centre for Remote Sensing, "Fundamentals of Remote Sensing," *Natural Resources Canada*.
- [94] K. D. Retherford and a. et. , "The Ultraviolet Spectrograph on the Europa Mission (Europa-UVS)," *American Geophysics Union*, 2015.
- [95] E. P. Turtle and a. et., "The Europa Imaging System (EIS): High-Resolution Imaging and Topography to Investigate Europa's Geology, Ice Shell, and Potential for Current Activity," *47th Lunar and Planetary Science Conference*, 2016.
- [96] D. L. Blaney and a. et. , "The Europa clipper Mapping Imaging Spectrometer for Europa (MISE): Using Compositional Mapping to Understand Europa," *50th Lunar and Planetary Science Conference*, 2019.
- [97] P. Christensen, "APAG Meeting," 2015.
- [98] N. Parab and V. Tomar, "Raman Spectroscopy of Algae: A Review," *Journal of Nanomedicine and Nanotechnology*, vol. 3, no. 2.
- [99] S. E. Jorge-Villar and H. G. Edwards, "Microorganism Response to Stressed Terrestrial Environments: A Raman Spectroscopic Perspective of Extremophilic Life Strategies," *Life*, vol. 3, no. 1, 2013.
- [100] I. Miralles, S. E. Jorge-Villar, Y. Canton and F. Domingo, "Using a Mini-Raman Spectrometer to Monitor the Adaptive Strategies of Extremophile Colonizers in Arid Deserts: Relationships Between Signal Strength, Adaptive Strategies, Solar Radiation, and Humidity," *Astrobiology*, vol. 12, no. 8, pp. 743-753, 2012.
- [101] H. G. Edwards, I. B. Hutchinson and R. Ingley, "Raman Spectroscopy of Extremophiles from Hot and Cold Deserts: An astrobiological Journey from Terrestrial Extreme Environments to Planetary Exploration".
- [102] D. B. Stajonovic and K. O. Cajko, "Extremophiles: Link between earth and astrobiology," *Zbornik Matice srpske za prirodne nauke*, 2008.
- [103] A. Good, "A New Test for Life on Other Planets," NASA Mars Exploration Program, 2017.
- [104] S. Nagl and a. et. , "Microfluidic chips for chirality exploration," *American Chemical Society*, vol. 83, pp. 3232-3238, 2011.
- [105] S. A. Lee and C. Yang, "A smartphone-based chip-scale microscope using ambient illumination," *Royal Society of Chemistry*, vol. 14, pp. 3056-3063, 2014.
- [106] National Aeronautics and Space Administration, "Stardust launch," 1999.
- [107] M. J. Burchell, J. Mann, A. W. Bunch and P. F. Brandao, "Survivability of Bacteria in Hypervelocity Impact," *Icarus*, vol. 154, no. 2, pp. 545-547, 2001.



- [108] G. M. Ayoub, L. Dahdah and I. Alameddine, "Transfer of bacteria via vapor in solar desalination units," *Desalination and Water Treatment*, vol. 53, no. 12, pp. 3199-3207, 2015.
- [109] Space Exploration Technologies Corporation, "Capabilities and Services," 2020. [Online]. Available: <https://www.spacex.com/about/capabilities>.
- [110] National Security Presidential Memorandum, "National Security Presidential Memorandum on the Launch of Spacecraft Containing Space Nuclear Systems," Administration of Donald J. Trump, 2019.
- [111] M. Hayhurst and a. et, "Mission Operations Cost Estimation Tool (MOCET)," NASA Cost Symposium, 2015.
- [112] World Nuclear Association, "Uranium Enrichment," [Online]. Available: <https://www.world-nuclear.org/information-library/nuclear-fuel-cycle/conversion-enrichment-and-fabrication/uranium-enrichment.aspx>.
- [113] A. Kieckhafer and L. B. King, "Energetics of Propellant Options for High-Power Hall Thrusters," *Space Nuclear Conference*, 2005.
- [114] H. Apgar, "Cost Estimating," in *Space Mission Engineering: The New SMAD*, Hawthorne, CA, Microcosm Press, 2011, pp. 289-324.
- [115] Markets and Markets, "Thermoelectric Generators Market worth \$741 million by 2025".
- [116] T. Mori.
- [117] A. Seppala.
- [118] K. Chaurasiya and S. Kumar, "Design and Analysis of Parabolic R".
- [119] S. M. Howell and R. T. Pappalardo, "Band Formation and Ocean-Surface Interaction on Europa and G".
- [120] M. Hayhurst, S. Eftekharzadeh, B. Wood, V. Jyothindran, Kellogg, C. Daniels, L. Jordin and W. Sasamoto, "Mission Operations Cost Estimation Tool (MOCET)," 2015.
- [121] United States General Accounting Office, "Cassini Mission Estimated Launch Costs for NASA's Mission to Saturn," 1995.
- [122] E. Zapata, "The State of Play US Space Systems Competitiveness," Future In-Space Operations Seminar, 2017.
- [123] N. Bray, "Space Shuttle and International Space Station," NASA, 2017. [Online]. Available: [https://www.nasa.gov/centers/kennedy/about/information/shuttle\\_faq.html](https://www.nasa.gov/centers/kennedy/about/information/shuttle_faq.html).
- [124] Office of Inspector General, "Management of NASA's Europa Mission," NASA, Washington, DC, 2019.
- [125] E. Berger, "After a remarkable resurrection, Firefly may reach space in 2019," 11 2 2019. [Online]. Available: <https://arstechnica.com/science/2019/02/firefly-returns-from-the-dead-with-a-larger-rocket-and-lunar-aspirations/3/>.
- [126] Firefly Aerospace, "Firefly Beta," 2019. [Online]. Available: <https://firefly.com/launch-beta/>.
- [127] United States Government Accountability Office, "Surplus Missile Motors," 2017.
- [128] S. Clark, "Spaceflight Now," 18 11 2010. [Online]. Available: <https://spaceflightnow.com/minotaur/stps26/101118preview/>.
- [129] Northrop Grumman, "Minotaur Rocket," [Online]. Available: <https://www.northropgrumman.com/space/minotaur-rocket/>.
- [130] Relativity Space, "Terran," [Online]. Available: <https://www.relativityspace.com/terran>.
- [131] Sigma-Aldrich Corporation, "Lithium Hydride," [Online]. Available: <https://www.sigmaaldrich.com/catalog/product/aldrich/201049?lang=en&region=US>.
- [132] Beryllium Science and Technology Association, "Facts and Figures," [Online]. Available: <http://beryllium.eu/about-beryllium/facts-and-figures/>.
- [133] Sigma-Aldrich Corporation, "Mercury," [Online]. Available: <https://www.sigmaaldrich.com/catalog/product/sigald/261017?lang=en&region=US>.



- [134] Sigma-Aldrich Corporation, "Boron," [Online]. Available: <https://www.sigmaaldrich.com/catalog/product/mm/112070?lang=en&region=US>.
- [135] Royal Society of Chemistry, "Americium," [Online]. Available: <https://www.rsc.org/periodic-table/element/95/americium>.
- [136] US Department of Energy, "Plutonium Certified Reference Materials Price List," [Online]. Available: <https://science.osti.gov/nbl/Certified-Reference-Materials/Prices-and-Certificates/Plutonium-Certified-Reference-Materials-Price-List>.
- [137] Sigma-Aldrich Corporation, "Boron," [Online]. Available: <https://www.sigmaaldrich.com/catalog/product/aldrich/gf96030086?lang=en&region=US>.
- [138] D. Incropera, Bergman and Lavine, introduction to Heat Transfer, John Wiley & Sons, Inc. 5th Ed. , 2007.

